Experimental Evaluation and Semi-Empirical Modeling of the Tractive Performance of Rigid and Flexible Wheels on Lunar Soil Simulant

Benjamin Paul Taylor

Thesis submitted to the faculty of the Virginia Polytechnic Institute and State University in partial fulfillment of the requirements for the degree of

Master of Science
In
Mechanical Engineering

Corina Sandu
Mehdi Ahmadian
Saied Taheri

July 9, 2009
Blacksburg, VA

Keywords: wheel mobility, off-road testing, Lunar soil simulant

Experimental Evaluation and Semi-Empirical Modeling of the Tractive Performance of Rigid and Flexible Wheels on Lunar Soil Simulant

Benjamin Paul Taylor

ABSTRACT

Understanding the effects of various wheel parameters on tractive performance is not completely understood. In order to properly quantify the individual effects of wheel parameters on the mobility of rigid and flexible wheels in soft soil, tests were performed, in cooperation with NASA Glenn Research Center (NASA-GRC), using the terramechanics rig at the Virginia Tech Advanced Vehicle Dynamics Lab (AVDL). To conduct such a study, four different wheels were evaluated under similar normal loads, slip ratios, and soil density. The first wheel represents the baseline, against which all the others were benchmarked. The remaining three wheels included the following parameter changes: 1) same diameter as the baseline but wider, 2) same width as the baseline but smaller in diameter, and 3) same width and diameter as the baseline but with a longer contact length. For each test the normal load, drawbar pull, and driving torque were measured and recorded for further analysis. To measure the effect of the changes in the wheels' parameters on the contact patch under different loads, a pressure pad was embedded below the surface of the Lunar simulant to measure the contact patch shape, size, and pressure distribution. Analysis of the experimental results showed that the drawbar pull was more significantly affected by the wheel diameter than by the contact width, and that same trend followed suit for the driving torque. Overall, the greater contact patch area resulted in a higher drawbar pull and torque.

Acknowledgement

I would like to first thank my advisor, Dr. Corina Sandu, for her many contributions to my work and academic achievement. Her support and understanding, in and out of the classroom, have helped me to achieve the academic and personal goals I set two years ago. I would also like to thank the other members of my M.S. committee, Dr. Mehdi Ahmadian and Dr. Saied Taheri, for their direction and teachings throughout my time here at Virginia Tech. From the lessons learned in Dr. Ahmadian's Land Vehicle Dynamics class, to the challenges met in Dr. Taheri's Tire Mechanics course, I have been fortunate to have learned the invaluable lessons they have taught me. I would also like to thank Mr. Vivake Asnani, Mr. Colin Creager, of NASA Glenn Research Center for not only their financial support, but also for the lessons I've learned through working with them, as well as for their hospitality during my time in Cleveland. Their challenges and questions have encouraged me to think well "outside the box." Special appreciation also goes to Mr. Damon Delap of NASA Glenn Research Center, and to Mr. Dave Glemming, Mr. Tim Rooney, Mr. Jim Benzing, and Mr. Jim Kish from the Goodyear Tire and Rubber Company for their help in getting the terramechanics operational through many long and laborious hours of work. The knowledge they have passed on to me will stick with me for years to come. My gratitude also goes to Mr. Aaron Schumacher from Kistler. His patience and guidance throughout the process of getting the terramechanics rig operational has played a crucial role in my work.

I would like to thank all my current and former colleagues at AVDL for their help with my work. Those who have helped me along the way to whom I am indebted include, but are in no way limited to, Ben Duprey, Charlie Weil, Dr. Florin Marcu, Mr. Michael Craft, Adam Woodward, Alireza Farjoud, Anake Umsrithong, and many others. Another special thanks goes to Mr. Carvel Holton, who's taught me lessons that cannot be learned in any classroom. I would also like to thank Mrs. Sue Teel for being my "lab mother." From completing infinite purchase requests to giving sound advice on dealing with life's curveballs, I am greatly indebted to her.

I would also like to express my most sincere gratitude to my family and to my dearest Sarah Jane, who have given me unending support through every trial and tribulation with their unceasing love.

Finally, I wish to acknowledge my Almighty God. Without His never-ending love, none of this would have ever been possible.

Contents

Acknowledgement iii
List of Tables vi
List of Figures vii
1. Introduction 1
1.1 Motivation 1
1.2 Research Approach 2
1.3 Thesis Outline 5
2. Review of Literature 7
2.1 Review of Literature: Single-wheel Testing Methods 7
2.2 Review of Literature: Rigid Wheel Modeling 11
2.3 Review of Literature: Summary 18
3. Description of Test Equipment 20
3.1 Description of Test Equipment: Soil Measurement Instrumentation 20
3.2 Description of Test Equipment: Terramechanics Rig Instrumentation 24
3.3 Description of Test Equipment: Terramechanics Rig Overview 28
3.4 Description of Test Equipment: Soil Preparation Method 35
3.5 Description of Test Equipment: Summary 43
4. Design of Experiment 45
4.1 Design of Experiment: Single-wheel Testing 45
4.1.1 Single-wheel Experimental Conditions 45
4.1.2 Single-wheel Experimental Procedure 47
4.2 Design of Experiment: 4x4 Vehicle Testing 50
4.2.1 4x4 Vehicle Experimental Conditions 50
4.2.2 4x4 Vehicle Experimental Procedure 52
4.3 Design of Experiment: Summary 53
5. Experimental Results and Discussion 55
5.1 Experimental Results and Discussion 55
5.1.1 32-in. x 7-in. Rigid Wheel 55
5.1.2 32-in. x 11-in. Rigid Wheel 60
5.1.3 20-in. x 7-in. Rigid Wheel 64

5.1.4 32-in. x 7-in. Spiral Wheel....68
5.2 Experimental Results and Discussion: Wheel Comparison....71
5.3 Experimental Results and Discussion: Pressure Pad Results....78
5.4 Experimental Results and Discussion: Summary....81
6. Modeling Results and Discussion....84
6.1 Modeling Results and Discussion: Individual Wheel Performance....84
6.2 Modeling Results and Discussion: Wheel Comparison....89
6.2.1 Exit Angle Determination....89
6.2.2 Results Using Same Exit Angles....94
6.2.3 Results Using Different Exit Angles....99
6.3 Modeling Results and Discussion: Validation....104
6.4 Modeling Results and Discussion: Conclusions....108
7. Supplemental Testing, Research Summary, and Future Work....109
7.1 Supplemental Testing, Research Summary, and Future Work: Fiber Optic Doppler LIDAR Testing....109
7.2 Supplemental Testing, Research Summary, and Future Work: Summary of Work....111
7.3 Supplemental Testing, Research Summary, and Future Work: Recommendations for Future Work....112
8. References....115
9. Appendices....117
A. Supplemental Test Data....117
B. MATLAB Codes Utilized....135
C. Terramechanics Rig Operations Manual....147

List of Tables

Table 1-1. Table of listed diameters and actual diameters for the three rigid wheels 5
Table 3-1. Conversion factors from controller units to SI units 35
Table 4-1. Sample spreadsheet used to set angular wheel velocities.....49
Table 5-1. Tabulated contact areas for each tested wheel under experimental loading conditions.....81
Table 6-1. Exit angles used to model the rigid wheels 92
Table A-1. Data from 32-in. x 7-in. rigid wheel tests sorted by desired normal loads.....120
Table A-2. Data from 32-in. x 11-in. rigid wheel tests sorted by desired normal loads.....122
Table A-3. Data from 20-in. x 7-in. rigid wheel tests sorted by desired normal loads.....124
Table A-4. Data from 32-in. x 7-in. spiral wheel tests sorted by desired normal loads 126

List of Figures

Figure 1-1. 32-in. x 7-in. rigid wheel (baseline) 3
Figure 1-2. 32-in. x 11-in. rigid wheel 3
Figure 1-3. 20-in. x 7-in. rigid wheel 4
Figure 1-4. 32-in. x 7-in. spiral wheel 4
Figure 2-1. Diagram labeled with variables used in rigid wheel model [18]. Note that velocity, force, and stress elements in the *y*-direction were not considered 16
Figure 2-2. Diagram of stresses on wheel [18] 18
Figure 3-1. Disassembled Rimik CP40 II cone penetrometer in its case 21
Figure 3-2. Assembled CP40 II cone penetrometer being used to check soil compaction 21
Figure 3-3. Labeled schematic of table-mounted bevameter used at NASA-GRC [19] 23
Figure 3-4. Shearing ring (with grousers) used in bevameter shear tests. The grousers were not used to collect the data used in the model for this document [19] 24
Figure 3-5. Uncovered TekScan I-Scan 3150 pressure pad 25
Figure 3-6. Kistler Instruments P650 wheel force sensor shown from wheel-mounting surface (left) and from above to depict near-field telemetry system (right) 26
Figure 3-7. Screenshot of Kistler control emulator 26
Figure 3-8. Celesco string potentiometer as it is mounted on the terramechanics rig 27
Figure 3-9. Screenshot of plots created with the LMS Test.Lab 8 28
Figure 3-10. Terramechanics rig at AVDL, shown with pneumatic tire on rigid metal surface ..29
Figure 3-11. Original counterweight assembly (left) and new air-spring design (right) 30
Figure 3-12. Camber and toe angle adjustment is done using the tie rod linkage (top view) 31
Figure 3-13. Volume below the testing surface can be used to store a second soil 32
Figure 3-14. Carriage on which test wheels/tires are mounted and tested 32
Figure 3-15. Drive train used to propel the carriage along the terramechanics rig 33
Figure 3-16. Depiction of how drive belt attaches to the carriage 34
Figure 3-17. Schematic of the master-slave controller configuration 34
Figure 3-18. Master-slave controller configuration 35
Figure 3-19. Angle at which shovel must be inserted perpendicular to the terrain. It should be held at such an angle as it is inserted farther 36

Figure 3-20. Loosened soil. After shoveling, it should look similar to these after the first pass (left) and final pass (right) 37
Figure 3-21. Rake being dragged along the top of the soil on first pass....37
Figure 3-22. Terrain profile created after three raking passes....38
Figure 3-23. Blade used to manually level "run-up" section of test lane....39
Figure 3-24. Hand tamper held at height from which it is dropped....39
Figure 3-25. Overlapping pattern created by dropping tamper....40
Figure 3-26. Blade used to level the test lane....40
Figure 3-27. Leveling blade immersed in soil while leveling the terrain....41
Figure 3-28. Results of soil leveling procedure....41
Figure 3-29. Winch and roller used to compact the soil....42
Figure 3-30. Test lane as it appears after being compacted with law roller....43
Figure 4-1. Diagram showing use of relative velocities to get slip ratio....46
Figure 4-2. On-board air tank used to set apply normal load to the wheel. The air tank was filled prior to each test run....48
Figure 4-3. Photo of 20-in. x 7-in. rigid wheel during test, with a slip ratio of 60%....50
Figure 4-4. NASA GRC 4x4 vehicle testing facility....51
Figure 4-5. Quantitative representation of controlled-pull method of increasing slip in step-wise manner....51
Figure 4-6. 4x4 vehicle used at NASA GRC for wheel tests, shown here with 32-in. x 7-in. rigid wheel. Attached circumferentially to each wheel are plastic grousers....52
Figure 5-1. Drawbar pull vs. slip ratio for the 32-in. x 7-in. rigid wheel....55
Figure 5-2. *DP* vs. F_z vs. S_d surface created with results of 32-in. x 7-in. baseline wheel tests...57
Figure 5-3. Projected view of *DP* vs. F_z for baseline wheel. The vertical lines represent lines of constant normal load....58
Figure 5-4. Driving torque vs. slip ratio for 32-in. x 7-in. wheel....59
Figure 5-5. τ vs. F_z vs. S_d surface created with results of 32-in. x 7-in. baseline wheel tests....60
Figure 5-6. Drawbar pull vs. slip ratio experimental results for the 32-in. x 11-in. rigid wheel....61
Figure 5-7. *DP* vs. F_z vs. S_d surface created from 32-in. x 11-in. wheel test results....62
Figure 5-8. Driving torque vs. slip ratio plot for 32-in. x 11-in. rigid wheel....63

Figure 5-9. 3-D plot of τ vs. F_z vs. S_d for the 32-in. x 11-in. rigid wheel 64
Figure 5-10. Drawbar pull vs. slip ratio curves for each load at which the 20-in. x 7-in. rigid wheel was tested 65
Figure 5-11. *DP* map for the 20-in. x 7-in. rigid wheel 66
Figure 5-12. Driving torque vs. slip ratio for the 20-in. x 7-in. rigid wheel 67
Figure 5-13. τ vs. F_z vs. S_d three-dimensional plot for the 20-in.-by-7-in. rigid wheel 67
Figure 5-14. Plot of drawbar pull vs. slip ratio for the 32-in. x 7-in. spiral wheel 68
Figure 5-15. Plot of driving torque vs. slip ratio for the 32-in. x 7-in. spiral wheel 69
Figure 5-16. 3-D surface created using *DP* results of the 32-in. x 7-in. spiral wheel tests 70
Figure 5-17. Torque map for the 32-in.-by-7-in. spiral wheel 71
Figure 5-18. Plots of drawbar pull vs. slip ratio for all four wheels under the 253.5-N normal load 72
Figure 5-19. Wheel plots of driving torque vs. slip ratio for all four wheels at the 253.5-N normal load 72
Figure 5-20. Plots of drawbar pull vs. slip ratio for the three rigid wheels under the 311.4-N normal load 74
Figure 5-21. Comparison plots of torque vs. slip ratio for the three rigid wheels, considering a 311.4-N normal load 74
Figure 5-22. Plot comparing drawbar pull vs. wheel slip for the three rigid wheels with an applied normal load of 355.8 N 75
Figure 5-23. Plots of driving torque vs. slip ratio for the three rigid wheels with a 80-lb_f (355.8-N) applied 76
Figure 5-24. Drawbar pull vs. slip ratio for the three rigid wheels with an applied 114-lb_f (507.1-N) normal load 77
Figure 5-25. Driving torque versus wheel slip for all three rigid wheels with 114-lb_f (507.1-N) normal load 77
Figure 5-26. Plot of contact pressure underneath the baseline wheel 78
Figure 5-27. Averaged pressure distribution of the 32-in. x 7-in. rigid wheel 79
Figure 5-28. Averaged contact pressure distribution for 20-in. x 7-in. rigid wheel 80
Figure 5-29. Pressure distribution plot for the spiral wheel under 57-lb_f (253.5-N) normal load 80

Figure 6-1. *DP* vs. S_d for the 32-in. x 7-in. rigid wheel for all four normal loads 85

Figure 6-2. Torque vs. slip ratio for the 32-in. x 7-in. rigid wheel for all four normal loads 85

Figure 6-3. Pull vs. slip ratio for the 32-in. x 11-in. rigid wheel for all normal loads 86

Figure 6-4. Torque versus slip ratio for the 32-in. x 11-in. wheel for all four normal loads 87

Figure 6-5. Drawbar pull vs. slip ratio for the 20-in. x 7-in. wheel for all normal loads 88

Figure 6-6. τ vs. S_d for 20-in. x 7-in. wheel under all four normal loads 88

Figure 6-7. Diagram of wheel with small exit angle 91

Figure 6-8. Diagram of wheel with large exit angle 91

Figure 6-9. Modeling output of sinkage vs. slip ratios for the three rigid wheels with equal exit angles 93

Figure 6-10. Modeling output of sinkage vs. slip ratios for the three rigid wheels with unequal exit angles 94

Figure 6-11. *DP* vs. S_d model results for the 57-lb_f (253.5-N) normal load 95

Figure 6-12. *DP* vs. S_d model results for the 70-lb_f (311.4-N) normal load 95

Figure 6-13. *DP* vs. S_d model results for the 80-lb_f (355.8-N) normal load 96

Figure 6-14. *DP* vs. S_d model results for the 114-lb_f (507.1-N) normal load 96

Figure 6-15. Driving torque vs. slip ratio for three wheels at 57-lb_f (253.5-N) normal load 97

Figure 6-16. Driving torque vs. slip ratio for three wheels at 70-lb_f (311.4-N) normal load 98

Figure 6-17. Driving torque vs. slip ratio for three wheels at 80-lb_f (355.8-N) normal load 98

Figure 6-18. Driving torque vs. slip ratio for three wheels at 114-lb_f (507.1-N) normal load 99

Figure 6-19. *DP* vs. S_d plots for three wheels under 57-lb_f (253.5-N) normal load, using unequal exit angles 100

Figure 6-20. *DP* vs. S_d plots for three wheels under 70-lb_f (311.4-N) normal load, using unequal exit angles 100

Figure 6-21. *DP* vs. S_d plots for three wheels under 80-lb_f (355.8-N) normal load, using unequal exit angles 101

Figure 6-22. *DP* vs. S_d plots for three wheels under 114-lb_f (507.1-N) normal load, using unequal exit angles 101

Figure 6-23. τ vs. S_d plots for three wheels under 57-lb_f (253.5-N) normal load, using unequal exit angles 102
Figure 6-24. τ vs. S_d plots for three wheels under 70-lb_f (311.4-N) normal load, using unequal exit angles 103
Figure 6-25. τ vs. S_d plots for three wheels under 80-lb_f (355.8-N) normal load, using unequal exit angles 103
Figure 6-26. τ vs. S_d plots for three wheels under 114-lb_f (507.1-N) normal load, using unequal exit angles 104
Figure 6-27. Modeling and experimental results for *DP* vs. S_d for 32-in. x 7-in. wheel at 253.5-N and 311.4-N normal loads.....105
Figure 6-28. Modeling and experimental results for τ vs. S_d for 32-in. x 7-in. wheel at 253.5-N and 311.4-N normal loads.....105
Figure 6-29. Modeling and experimental results for *DP* vs. S_d for 32-in. x 11-in. wheel at 355.8-N and 507.1-N normal loads.....106
Figure 6-30. Modeling and experimental results for τ vs. S_d for 32-in. x 11-in. wheel at 355.8-N and 507.1-N normal loads.....106
Figure 6-31. Modeling and experimental results for *DP* vs. S_d for 20-in. x 7-in. wheel at 355.8-N and 507.1-N normal loads.....107
Figure 6-32. Modeling and experimental results for τ vs. S_d for 20-in. x 7-in. wheel at 355.8-N and 507.1-N normal loads.....107
Figure 7-1. Diagram of LIDAR system 109
Figure 7-2. Velocity calibration diagram for fiber-optic cables 110
Figure A-1. Mean Pressure-Sinkage Curve for the 7.6-cm plate.....117
Figure A-2. Mean Pressure-Sinkage Curve for the 10.2-cm plate.....118
Figure A-3. Mean Pressure-Sinkage Curve for the 19-cm plate.....118
Figure A-4. Measured slip vs. command slip of the spiral wheel.....119
Figure A-5. 20-in. x 7-in. rigid wheel with 70-lb_f (311.4-N) normal load applied.....127
Figure A-6. 20-in. x 7-in. rigid wheel with 80-lb_f (355.8-N) normal load applied.....128
Figure A-7. 20-in. x 7-in. rigid wheel with 114-lb_f (507.1-N) normal load applied.....128
Figure A-8. 32-in. x 7-in. rigid wheel with 70-lb_f (311.4-N) normal load applied.....129

Figure A-9. 32-in. x 7-in. rigid wheel with 80-lb_f (355.8-N) normal load applied.....129
Figure A-10. 32-in. x 7-in. rigid wheel with 114-lb_f (507.1-N) normal load applied.....129
Figure A-11. 32-in. x 11-in. rigid wheel with 70-lb_f (311.4-N) normal load applied.....130
Figure A-12. 32-in. x 11-in. rigid wheel with 80-lb_f (355.8-N) normal load applied.....130
Figure A-13. 32-in. x 11-in. rigid wheel with 114-lb_f (507.1-N) normal load applied.....131
Figure A-14. Modeling and experimental results for *DP* vs. S_d for 32-in. x 7-in. wheel at 355.8-N and 507.1-N normal loads.....132
Figure A-15. Modeling and experimental results for τ vs. S_d for 32-in. x 7-in. wheel at 355.8-N and 507.1-N normal loads.....132
Figure A-16. Modeling and experimental results for *DP* vs. S_d for 32-in. x 11-in. wheel at 253.5-N and 311.4-N normal loads.....133
Figure A-17. Modeling and experimental results for τ vs. S_d for 32-in. x 11-in. wheel at 253.5-N and 311.4-N normal loads.....133
Figure A-18. Modeling and experimental results for *DP* vs. S_d for 20-in. x 7-in. wheel at 253.5-N and 311.4-N normal loads.....134
Figure A-19. Modeling and experimental results for τ vs. S_d for 20-in. x 7-in. wheel at 253.5-N and 311.4-N normal loads.....134
Figure C-1. Panel HVP-1 supplies 480 Volts to the motors. Breaker 15 must be flipped on to supply the voltage 147
Figure C-2. Panel LVP-1 supplies 120 Volts to power the motors. Breaker 18 must be flipped on to supply the voltage 148
Figure C -3. The controller panel has been successfully energized when the 480 V and 120V lights are illuminated.....148
Figure C-4. The LMS SCADAS III data acquisition system (DAQ). The power switch is located on the back of the device above the power chord connection.....149
Figure C-5. Boot the desktop computer to bring up the user desktop 149
Figure C-6. Keyed safety switch located at the Northeast corner of the terramechanics rig.....150
Figure C-7. The selection scheme showing how to open PiCPro, the controller interface 151
Figure C-8. The PiCPro code blocks for Axes 1 and 2 where the rate of Axis 1 must be set to zero and the rate of Axis 2 must be set to 2 *rad/s* to warm up the Kistler wheel sensor....152

Figure C-9. The terramechanics rig controller showing the function of each button corresponding to an example code....152
Figure C-10. The Kistler System with power source above and DAQ below....153
Figure C-11. The laptop computer that runs the Kistler system user interface....154
Figure C-12. The COM 1 port must be enabled when the Kistler interface is opened....155
Figure C-13. The main screen of the Kistler interface displays the measured forces and moments....155
Figure C-14. The Setup screen of the Kistler system....156
Figure C-15. The Diagnostics screen of the Kistler system....157
Figure C-16. The Signal Offset screen of the Kistler system....158

1. Introduction

Within the field of land vehicle dynamics, it is commonly known that one of the most complex components is the wheel/tire; however, this is also one of the least understood elements. Moreover, a good understanding of the wheel in off-road conditions, whether in mud, sand, or on icy terrain, is even less likely. However, a realistic prediction of off-road mobility is invaluable in the development of vehicles and the wheels/tires on which they roll [1]. Furthermore, an understanding of how a wheel's parameters affect off-the-road mobility is needed to create efficient wheels for use on Earth and in extraterrestrial environments.

The goals of the terramechanics field are to study the interaction between the running gear of a vehicle and the terrain and to establish guidelines for the development and testing of off-road wheels/tires/tracks and the vehicles on which they are mounted [2]. One challenge in understanding wheel traction in off-road conditions is that most studies are performed using pneumatic tires. While it is possible to compare the tractive performance of various tires, it is still a challenge to compare different designs. A very important step to make such comparisons is in understanding the effect of a single tire parameter change on the tractive and mobility characteristics of a tire. For example, as a tire's radius decreases under a given normal load, the contact patch becomes wider and longer. Controlling such an interrelated change proves nearly impossible when comparing the tire performance. Along with these interrelated parameters, another source of variability lies in the soil being studied. When modeling soil and testing in controlled environments in a deterministic framework, there often exists the assumption of uniformity, which is unrealistic. Current studies attempt to simulate the soil properties in a stochastic framework, treating different soil parameters as uncertain [3]. This study will mainly focus on understanding the behavior of rigid and flexible wheels on a mixture of very dry sand, which simulates the Lunar soil.

1.1 Motivation

Gaining a thorough understanding of the mobility effects of wheel/tire parameters serves a crucial role not only on this planet but also on celestial terrains [2]. While tire companies research new tire designs and technologies, there is also a growing demand for wheel designs that will be used on other heavenly bodies, i.e., the Moon. The National Aeronautics and Space

Administration (NASA) has become very interested in Lunar and planetary rover technologies as part of efforts to return to the Moon [4].

1.2 Research Approach

In order to limit uncertainties within the experiments discussed in this work, a systematic approach was taken in which single wheel parameters were changed to determine their effects on the tractive performance of rigid and flexible wheels. The first rigid wheel was used as a baseline wheel, from which the remaining three were altered in a specific way. The second rigid wheel was consistent with the diameter of the baseline but had a wider contact patch. The third rigid wheel had the same width as the baseline, but a smaller diameter. The final wheel tested in this study was designed to have an increased contact length but the same undeflected diameter and width as the baseline wheel in order to simulate a wheel of larger diameter. To understand such a parameter change, this wheel was flexible and consisted of spiral spokes.

The three rigid wheels were tested over a range of 21 slip ratios, ranging from -15% to +60%, and were subject to 4 normal loads: 57, 70, 80, and 114 lb_f (253.5, 311.4, 355.8, and 507.1 N). These normal loads were selected with the original Lunar Roving Vehicle (LRV) wheel load of 57 lb_f in mind, extending the range to twice that load (114 lb_f). The flexible wheel was also subjected to the same slip ratios, but was only tested under its nominal 57-lb_f (253.5-N) normal load. The four wheels are shown in Figures 1-1 through 1-4 below.

Figure 1-1. 32-in. x 7-in. rigid wheel (baseline).

Figure 1-2. 32-in. x 11-in. rigid wheel.

Figure 1-3. 20-in. x 7-in. rigid wheel.

Figure 1-4. 32-in. x 7-in. spiral wheel.

While the rigid wheels in Figures 1-1 through 1-3 have been listed as having diameters of 32 inches and 20 inches, the measured diameters of these three wheels are actually less than the their listed values. Determining the effective diameter of the spiral wheel is discussed later in

this thesis. Table 1-1 lists the given diameter of the three wheels alongside the actual measured diameter.

Table 1-1. Table of listed diameters and actual diameters for the three rigid wheels.

Wheel Label	Given Diameter (in.)	Measured Diameter (in.)
32-in. x 7-in. rigid wheel	32	31.5
32-in. x 11-in. rigid wheel	32	31.5
20-in. x 7-in. rigid wheel	20	19.5

1.3 Thesis Outline

Chapter Two includes a literature review relevant to this study. The first section discusses methods of single-wheel testing previously employed by various laboratories. The second section provides a look into wheel models used in previous studies.

Chapter Three is broken down into four main sections: 1) soil measurement instruments, 2) measurement devices outfitted on the terramechanics rig, 3) the terramechanics rig and its functionality, and 4) a step-by-step breakdown of the method used to prepare the GRC-1 Lunar soil simulant. Included in the first section are descriptions of the cone penetrometer and the bevameter. The second segment discusses the instruments with which the terramechanics rig is outfitted. In the third section of this chapter, the terramechanics rig is presented, along with a functional breakdown of its features and capabilities. The final piece of this section provides instructions for carrying out the soil preparation method, which was developed through the collaborative effort of NASA-GRC engineers and the AVDL at Virginia Tech.

Chapter Four discusses the design of experiment. Detailed in this chapter is a description of the testing procedure for the single-wheel tests performed at Virginia Tech. Also presented is the testing on a 4 x 4 vehicle platform currently being performed at NASA-GRC.

The experimental results of this study are presented in Chapter Five. These results are from testing the rigid wheels under the four normal loads, as well as from testing the spiral-shaped wheel under its single load case. All four wheels will be compared for the lightest loading case, and the three rigid wheels will be compared for the remaining three normal loads. The chapter will conclude with a presentation of results from the pressure pad tests of static contact pressure.

Results from a preliminary attempt at modeling the three rigid wheels for each load case are presented in Chapter Six. Comparisons of the tractive performance of these three wheels are also provided here. The experimental and modeling results will also be compared in this chapter.

Chapter Seven includes additional tests performed and remarks pertaining to this study. First, wheel-slip tests using a fiber optic Doppler LIDAR system will be briefly covered. Next, concluding remarks on the work performed in this study will be presented, followed by recommendations for future work. Included in these recommendations, are suggested modifications to the terramechanics rig.

2. Review of Literature

The effects of various independent wheel parameters on tractive performance are not completely understood. In order to properly quantify the individual effects of wheel parameters on the mobility of rigid and flexible wheels in soft soil, multiple tests must be performed under consistent dynamic and soil conditions. Moreover, when selecting a wheel model to be used for comparison against the test results, one needs to carefully consider all the model assumptions, inputs, and outputs. The first section of this chapter will discuss various testing methods described in the literature, and the lessons learned from these experiments in order to help develop a design of experiment for this study. The second section will discuss wheel models pertinent to this study. Reviewing these models will help us identify the best wheel model to employ, which will provide data that we can compare with the test results.

2.1 Review of Literature: Single-wheel Testing Methods

Tests can be executed on various platforms, including instrumented tractors, 4x4 vehicles with attachments, and single-wheel indoor soil bins [5]. Much can be learned from each of these test facilities. Thus, using a good testing procedure is imperative in obtaining accurate, usable test results. The methods discussed in this section have been selected based on the following scope of testing:

- Tests must be performed using a single-wheel test rig.
- Terrain must be dry and granular in nature.
- Slip ranges must cover -15% to 100%.
- Tests are conducted on level soil.
- Tests are performed at relatively low speeds, i.e. < 2 mph (0.894 m/s).

In order to evaluate and rate the test procedures discussed, the following criterion were used in this study:

1. Accuracy of results and data collected.
2. Amount of information gained from test results, i.e. thoroughness of test.
3. Repeatability of test results.
4. Feasibility of conducting the procedure with the available facilities.
5. Time required for testing.

It is important to note that single-wheel tests are the only type to be considered because the terramechanics rig at the Virginia Tech is a single-wheel test rig. Thus, we will not include other test types (4x4, etc.) in this review.

During the late 1960s, the U. S. Army Engineer Waterways Experiment Station (WES) ran a series of single-wheel tests of off-road tires to understand how testing techniques affect the performance characteristics of a wheel operating in dry sand [6]. This was done by evaluating several sources of uncertainty previously observed during terramechanics tests. These uncertainties included the effect of starting conditions on the results of controlled-slip tests, how well varying- and constant-slip tests results compare, and the ability to compare controlled-slip and controlled-pull test results. To clarify, controlled-slip tests are those in which the wheel and carriage are moved independent of one another, and the drawbar pull (*DP*) of the wheel can be measured directly. In a controlled-pull test, the carriage velocity is dependent on the applied in the direction opposite the carriage's motion; the wheel's ability to overcome this force (and the carriage's motion resistance) is the only source of motion. In this case the calculation of drawbar pull must consider the friction and inertia of the carriage, as well as the applied force.

Let it be known that prior to each test run, the soil was prepared in place. The soil was first tilled, and then screed-leveled, and this method helped to provide a uniform soil density along the length of the test bed. Some tests called for a greater soil density so a pneumatic tire was rolled over the terrain to provide the desired compaction. Nowadays, small rollers are used to compact the soil ([7]-[9]), as they can provide compaction on a wider test lane. Instead of reprocessing the soil in place, some tests performed during the evaluation phase of the original LRV wheels' development required that the soil be completely removed from the bin. Once removed, the bin would be refilled in layers and leveled between each layer. Alternatively, the same filling process involved filling the soil bin in layers and compacting the sand between each layer [10]. Although doing this provided a more uniform soil condition after all was said and done, the time and energy required to do this was not worth the price paid. Recently, automated soil processing methods have been implemented. At Kyoto University in Japan, a device separate from the tire testing assembly is used to loosen, level, and compact the soil [7]. On the front of this Mixing-and-Compaction Device (MCD) rests a gasoline-powered tiller to churn up the terrain. On the rear of the device an aluminum plate is used to level the terrain. Following

this leveling plate is the rubber-coated compaction roller, which can be passed over the soil multiple times to obtain the desired soil density.

Some soil reprocessing methods depend upon the type of wheel test being performed using that facility. Researchers at the University Putra Malaysia (UPM) in Selangor DE, Malaysia use two different compaction methods, depending on whether they are in towed-wheel mode or driven-wheel mode [9]. Prior to compaction, the soil is manually loosened and hand-leveled. If in towed-wheel mode, 100-kg gasoline-powered vibrating soil compactor is run over the surface to achieve the desired relative density. If in driven-wheel mode, one of either two hand-rollers is used instead. These rollers are constructed of steel tubes filled with concrete, and individually amass to 29 and 40 kg.

Following the final soil preparation step in these procedures, a cone penetrometer is commonly used to check for the proper relative density ([6], [11]). This method uses a force-measurement device (load cell, transducer, etc.) and a pre-programmed area of its cone-shaped tip to measure the pressure applied to the soil [1]. Simultaneously, a linear measurement device (LVDT, string potentiometer, etc.) is used to measure the depth below the surface that the cone has traveled.

Although preparing the soil prior to each test run has become common practice in tire/wheel-soil testing, some tests are also performed in a multiple-pass format [10]. Such a test can be used to simulate the rear wheel of a vehicle passing through the rut created by its corresponding front wheel. Many soil bins have the capability to perform the multi-pass tests as needed ([7], [12], [9]).

When performing single-wheel tests, various factors are considered. One such factor is the translational velocity of the wheel carriage. This is especially important when performing towed-wheel (rolling resistance) tests, in which minimizing strain rate and soil inertia are priorities [11]. Generally, lower speeds are selected to avoid these undesirable soil effects. Some examples include testing during the original LRV wheel development, in which speeds of 0.5 m/s measured [13]. UPM has designed its terramechanics rig to achieve speeds ranging from 0.053 to 0.547 m/s [9]. At the Soil Machine Mechanics Laboratory of the University of Newcastle upon Tyne, the single-wheels wheel tests were performed at 0.045 m/s.

One of the most important, controllable parameters of any tire/wheel test is the slip ratio, which dependent upon translational velocity at the wheel center, defined in equation (2.1):

$$s_d = \frac{R\omega - V_x}{R\omega} = 1 - \frac{V_x}{R\omega} \tag{2.1}$$

where R is the rolling radius of the tire/wheel, ω is the angular velocity of the tire/wheel, V_x is the translational velocity at the wheel center, and $|s_d| < 1$. Controlled-slip tests, as previously defined, provide the greatest amount of information when developing pull-slip and torque-slip relationships [6]. Several methods of inducing slip were explored at WES ([13], [6]). These included programmed-increasing slip, programmed-decreasing slip, and constant slip. Slip was programmed to increase by running the test wheel at a constant angular speed and actuating the carriage at a velocity greater than that of the wheel (negative slip); the carriage was then slowed at a constant, gradual rate until its velocity reached zero (100% slip). On the other hand, in the programmed-decreasing slip tests the wheel velocity was still held constant, but the carriage started at a speed slower than that of the wheel and increased at a constant rate until reaching a desired value in the negative slip range. During constant-slip tests the carriage and wheel velocities were held at constant, preset values.

Several conclusions were made based on these three methods [6]. First, when comparing the effects of programmed-increasing and programmed-decreasing slip tests, the programmed-decreasing tests produced larger pull and torque values, for slip ratios up to +10 or +15%; however, beyond these values the torque and pull reached equilibrium. Second, comparing programmed-slip to constant-slip tests indicates that at larger slip ratios there exists no difference between the torque and pull values; however, at the time of the report further testing was needed to determine the best technique to use at lower slip ratios. Lastly, it was found during programmed-slip tests that once a desired slip value was attained, the overall wheel performance became independent of starting conditions, i.e., initial velocities.

The controlled-pull test technique provides a more realistic method of testing than the controlled-slip method, at higher slip ratios the results become inconsistent [6]. It is important to note that during LRV wheel tests performed at WES the drawbar pull and torque continually increased with wheel slip, beyond about 20% slip; however, the energy consumption outweighs the traction created at the wheel-soil interface [10]. An example of such a situation is best exemplified with a 4x4 vehicle where the tractive effort of the running gear saturates the soil stresses and the vehicle becomes stuck, with its wheels spinning in place. Energy would be

consumed as long as the wheels continue to spin, but energy would be wasted. Therefore, it was concluded that comparing the pull of multiple wheels/tires at +20% slip was a useful metric.

The information presented in this literature review has provided a springboard off of which the procedures at the Virginia Tech Advanced Vehicle Dynamics Lab have been derived. The soil preparation procedures employed at other laboratories were considered in the development of the method used in this study. Because of its versatility and consistency, a variation of the controlled-slip testing method was employed for the wheel tests.

2.2 Review of Literature: Rigid Wheel Modeling

This section provides a broad overview of possible approaches that were considered for the modeling portion of this study. The models were reviewed with the following scope in mind:

- The terrain discussed in the models is similar to the Lunar regolith (e.g., dry sand).
- The models use inputs similar to the experimental setup, i.e. normal load and slip ratio.
- The models account for rigid wheels.
- The models are analytical or semi-empirical.
- The models involve only two degrees of freedom, e.g., translation along the *x*-axis and rotation about the *y*-axis.

In order to evaluate and rate the test procedures discussed, the following criterion were used:

1. Accuracy of model outputs, based on validations against experimental results.
2. Time required to run the modeling code.
3. Information that can be gained from models.
4. Validity of modeling assumptions as related to their applicability in this study.
5. Level of involvement in executing the model (needs to already be coded).

The wheel model developed through the cooperative effort of the University of the Federal Armed Forces Hamburg and the Ford Research Center in Germany builds on the fundamental pressure-sinkage relationship derived by M.G. Bekker and the shearing relationships of Janosi and Hanamoto [14]. Bekker's equation is shown in equation (2.2) below:

$$p = \left(\frac{k_c}{b} + k_\phi \right) z^n = k z^n \tag{2.2}$$

where n, k_c, and k_ϕ are pressure-sinkage parameters, z is the sinkage, and b is the width of a rectangular contact area or the radius of a circular contact area ([14], [15], [16], [1]). Equation (2.3) represents the Janosi and Hanamoto formulation as:

$$\tau = \tau_{\max} \left(1 - e^{-j/K} \right) \tag{2.3}$$

where j is the local shear displacement, K is the shear deformation modulus, and $\tau_{\max}$ is the maximum shear strength of the soil, as defined by the Coulomb rule in equation (2.4) as:

$$\tau_{\max} = c + p \tan \phi \tag{2.4}$$

where c is the soil cohesion and ϕ is the angle of internal shearing resistance of the terrain([14], [16], [1]). A unique feature of this model, which was named AS^{2}TM, lies within its data-storing capabilities. In order to model multi-pass effects on tire performance, the model records the vertical soil deformation and compaction for each wheel passing through a rut. Thus, this model could be valuable in the study of a full-vehicle model. As with any tire/wheel model, assumptions have been made in the development of this model. The primary assumption is that the tires/wheels being studied are either rigid wheels or approximated as rigid due to traversing very soft terrains and/or very high inflation pressures. The model also accounts for elastic tire deflection by substituting a circle of larger diameter. The size of this substitute circle is determined through an iterative solution to finding the equilibrium between the vertical soil reaction force and the vertical wheel load. A downside to implementing this wheel model is that it cannot be run using a Windows platform; rather, it requires a Linux/Unix-based system to operate.

Another model that has become quite popular employs Wong's work discussed in [17] and [16], and is called the Tractive Prediction Module (TPM). Wong uses the average radial

($\sigma(\theta)$) and tangential stresses ($\tau(\theta)$) across the width of the wheel to describe the normal wheel load in equation (2.5), the drawbar pull in equation (2.6), and the driving torque in equation (2.7) as:

$$W = rb\left\{\int_{\theta_2}^{\theta_1}\sigma(\theta)\cos d\theta + \int_{\theta_2}^{\theta_1}\tau(\theta)\sin d\theta\right\} \tag{2.5}$$

$$DP = rb\left\{\int_{\theta_2}^{\theta_1}\tau(\theta)\cos d\theta - \int_{\theta_2}^{\theta_1}\sigma(\theta)\sin d\theta\right\} \tag{2.6}$$

$$T = r^2 b\int_{\theta_2}^{\theta_1}\tau(\theta)\,d\theta \tag{2.7}$$

where *r* is the wheel radius, *b* is the wheel width, θ is any angle made with the vertical axis that lies between the entry (θ_1) and exit (θ_2) angles of the wheel-soil contact patch ([17], [1]). $\tau(\theta)$ is defined just as it was in equation (2.3). Conversely, Wong uses Reece's plasticity-based pressure-sinkage equation to define $\sigma(\theta)$ as:

$$p = \sigma(\theta) = \left(ck_c' + \gamma bk_\phi'\right)\left(\frac{z}{b}\right)^n \tag{2.8}$$

where *c* is the soil cohesion, γ is the weight density of the terrain, *n* is the sinkage exponent, k_c' is related to cohesion, and k_ϕ' is related to the angle of internal friction. Both k_c' and k_ϕ' are dimensionless pressure-sinkage parameters that are determined using the bevameter ([15], [16], [1]). It should be noted that equation (2.8) assumes that the soil of interest is uniform [15]. One of the commonly-used assumptions that this model does not use is that the radial soil reaction at an arbitrary element of the rim is the same as that under a plate that has been penetrated to the same depth as the element, insinuating that radial stress is independent of wheel slip [17]. However, proposed for use in this model is that the radial stress can be described using a variation of equation (2.8), as:

$$\sigma_1(\theta) = \left(ck_c' + \gamma bk_\phi'\right)\left(\frac{r}{b}\right)^n (\cos\theta - \cos\theta_1)^n \tag{2.9}$$

Equation (2.9) is defined as the radial stress for the region from the beginning of the contact patch to the point of maximum radial stress θ_M. From this point of maximum radial stress to the end of the contact patch, the radial stress is shown here, as:

$$\sigma_2(\theta) = \left(ck_c' + \gamma bk_\phi'\right)\left(\frac{r}{b}\right)^n \left[\cos\left(\theta_1 - \left(\frac{\theta - \theta_2}{\theta_M - \theta_2}\right)(\theta_1 - \theta_M)\right) - \cos\theta_1\right]^n. \tag{2.10}$$

Also defined in [17] is the point of maximum radial stress, shown below:

$$\theta_M = (c_1 + c_2 s_d)\theta_1 \tag{2.11}$$

where c_1 and c_2 are experimentally-determined coefficients and s_d is defined in equation (2.1).

Using equations (2.9) – (2.11), equations (2.5) – (2.7) were rewritten as:

$$\begin{aligned} W = rb\Bigg\{ &\int_{(c_1+c_2s_d)\theta_1}^{\theta_1} \sigma_1(\theta)\cos\theta d\theta + \int_{\theta_2}^{(c_1+c_2s_d)\theta_1} \sigma_2(\theta)\cos\theta d\theta \\ &+ \int_{(c_1+c_2s_d)\theta_1}^{\theta_1} \tau_1(\theta)\sin\theta d\theta + \int_{\theta_2}^{(c_1+c_2s_d)\theta_1} \tau_2(\theta)\sin\theta d\theta \Bigg\} \end{aligned} \tag{2.12}$$

$$\begin{aligned} DP = rb\Bigg\{ &\int_{(c_1+c_2s_d)\theta_1}^{\theta_1} \tau_1(\theta)\cos\theta d\theta + \int_{\theta_2}^{(c_1+c_2s_d)\theta_1} \tau_2(\theta)\cos\theta d\theta \Bigg\} \\ - rb\Bigg\{ &\int_{(c_1+c_2s_d)\theta_1}^{\theta_1} \sigma_1(\theta)\sin\theta d\theta + \int_{\theta_2}^{(c_1+c_2s_d)\theta_1} \sigma_2(\theta)\sin\theta d\theta \Bigg\} \end{aligned} \tag{2.13}$$

$$T = r^2 b\left\{\int_{(c_1+c_2s_d)\theta_1}^{\theta_1} \tau_1(\theta)d\theta + \int_{\theta_2}^{(c_1+c_2s_d)\theta_1} \tau_2(\theta)d\theta\right\} \tag{2.14}$$

Equations (2.12) – (2.14) are numerically integrated to determine their results [17]. This model uses the normal wheel load, slip ratio, terrain parameters, and wheel width and radius as inputs to determine the tractive performance.

The next wheel model to be considered in this study is that which was developed by B. Chan [18]. The code can be run on any operating system as a MATLAB m-file. The purpose of its creation was to combine the works of various researchers in the terramechanics field and implement their findings into an application that can be run as part of a vehicle dynamics simulation [18]. Several assumptions were made in the development of this model, and they are as follows:

1. When the ground becomes very hard/rigid, the tire model switches to the behavior of a flexible tire operating on the road. This limits the stresses imposed on the soil by the tire once it starts deforming.
2. The soil being modeled is considered to be a plastic material using quasi-static equilibrium plate sinkage equations based on strip load analysis, i.e. Bekker's and Reece's pressure-sinkage equations.
3. The tire model is rooted in analytical mechanics and is augmented with empirically obtained information to account for effects that would not be captured otherwise.
4. The tire model should revert to a pure longitudinal model or to a pure lateral slip model when either the lateral, or respectively, the longitudinal slip is zero.
5. The tire inflation pressure and the temperature remain constant or change at a very slow rate during the entire simulation.
6. The tire becomes approximated as a rigid wheel when it is traversing extremely soft terrain, which would result in a more significant soil deformation compared to the tire deformation. The tire can also be assumed rigid when the combination of carcass rigidity pressure and inflation pressure exceed the terrain's bearing capacity.
7. The contact patch of the wheels being modeled is rectangular in shape.

It is important to note that this model is able to be used in combined-slip situations, in which both longitudinal and lateral forces will be experienced by the wheel. However, due to the scope of this study and of the models being considered, only purely longitudinal (straight-line)

motion will be studied. Shown in Figure 2-1 is a diagram depicting the variables used in this model.

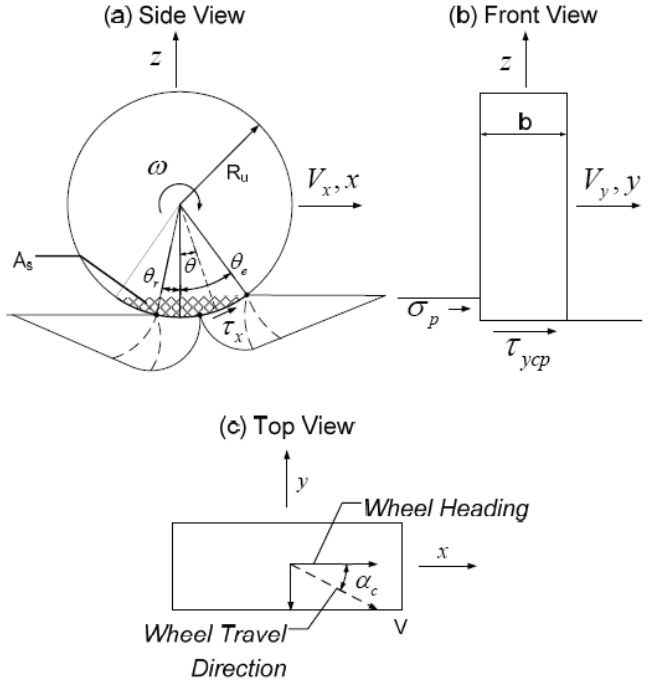

Figure 2-1. Diagram labeled with variables used in rigid wheel model [18]. Note that velocity, force, and stress elements in the *y*-direction were not considered.

The variables shown in Figure 2-1 that are of interest in this study are listed below:

$R_u \equiv$ Undeformed radius of the wheel (physical radius of wheels modeled in this study)
$\theta_e \equiv$ Entry angle
$\theta_r \equiv$ Exit angle
$\theta \equiv$ Angle on the wheel relative to a fixed frame
$V \equiv$ Longitudinal velocity
$\omega \equiv$ Angular velocity of the wheel
$b \equiv$ Width of the wheel
$A_s \equiv$ Area of the wheel sunk in soil in the plane of the wheel
$\tau_x \equiv$ Shear stress acting in the longitudinal direction of the wheel

As a result of the plasticity assumption, Chan's model utilizes Reece's pressure-sinkage formulation, shown in equation (2.8) just as was done in [17]. Likewise, this model applied equations (2.9) and (2.10) for the radial stresses, as:

$$\sigma_n(\theta) = \begin{cases} \sigma_{nf}(\theta) & \theta_N \le \theta < \theta_e \\ \sigma_{nr}(\theta) & -\theta_r < \theta \le \theta_N \end{cases} \tag{2.15}$$

where $\sigma_{nf}(\theta)$ and $\sigma_{nr}(\theta)$ are equal to $\sigma_1(\theta)$ and $\sigma_2(\theta)$, respectively, and θ_N is the point along the circumference where the sign of the shear stress changes and the maximum principle stress occurs [18]. This model calculates the shear stress in the longitudinal direction using the Janosi-Hanamoto equation that was also used in [14], [17], and [1]; this formulation is restated in equation (2.16) below:

$$\begin{aligned} \tau_x &= \tau_{\max}\left(1 - e^{-j_x/K_x}\right) \\ &= \left(c + \sigma_n \tan(\phi)\right)\left(1 - e^{-j_x/K_x}\right) \end{aligned} \tag{2.16}$$

where K_x is the shear deformation modulus in the longitudinal direction and j_x is the shear displacement defined in equation (2.17), as:

$$j_x = R_u\left[(\theta_e - \theta) - (1 - s_d)(\sin\theta_e - \sin\theta)\right] \tag{2.17}$$

where s_d is the wheel slip ratio defined in equation (2.1). As with most predictive mobility analyses, this model evaluates the normal wheel load, drawbar pull, and driving torque using the following equations:

$$W = R_u b\left(\int_{-\theta_r}^{\theta_e} \sigma_n(\theta)\cos(\theta)\,d\theta + \int_{-\theta_r}^{\theta_e} \tau_x(\theta)\sin(\theta)\,d\theta\right) \tag{2.18}$$

$$DP = R_u b\left(\underbrace{\int_{-\theta_r}^{\theta_e} \tau_x(\theta)\cos(\theta)\,d\theta}_{\text{Shear Thrust}} - \underbrace{\int_{-\theta_r}^{\theta_e} \sigma_n(\theta)\sin(\theta)\,d\theta}_{\text{Compaction Resistance}}\right) \tag{2.19}$$

$$T = R_u^2 b\int_{-\theta_r}^{\theta_e} \tau_x(\theta)\,d\theta \tag{2.20}$$

Shown in Figure 2-2 is a depiction of the normal and shear stresses on the wheel shown as radial and tangential stresses, respectively.

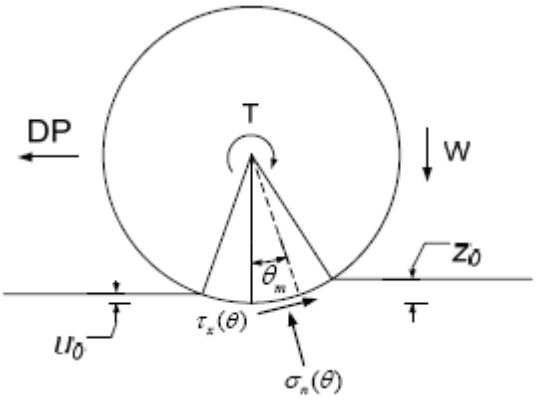

Figure 2-2. Diagram of stresses on wheel [18].

In this figure the sinkage of the wheel is determined using equation (2.21) below:

$$z_0 = R_u\left(1-\cos\theta_e\right) \tag{2.21}$$

Similarly, the unloaded terrain depth is calculated as:

$$u_0 = R_u\left(1-\cos\theta_r\right) \tag{2.22}$$

The inputs used in this model include the following:

- Slip ratio (s_d)
- Normal load (F_z)
- Angular wheel velocity $\left(\omega\right)$
- Wheel radius (R_u) and width (b)
- Soil parameters gathered from bevameter tests $\left(K_x,\ \phi,\ n,\ c,\ k_c',\ k_\phi',\ \gamma\right)$

Outputs of the model include drawbar pull (DP), driving torque (T), and wheel sinkage (z).

2.3 Review of Literature: Summary

Testing methodologies and rigid wheel modeling approaches have been thoroughly discussed in this chapter. From the literatures that were discussed, a couple of conclusions can be made about which approach should be taken, with respect to testing and modeling:

1. Because the controlled-slip test type allows for the most information to be gathered per test, and because the terramechanics rig is capable of performing this type of test, a slip-increasing style will be employed for this study.
2. Because Chan's model is accessible and can be run on a Windows operating system using MATLAB, it will be used for the rigid wheel modeling portion of this study.

3. Description of the Test Equipment

The terramechanics rig at the Advanced Vehicle Dynamics Lab facilitates the experimental studies of wheels/tires in a nearly-completely controlled environment. Having access to such a test rig eliminates environmental factors (snow, rain, etc.) and therefore, allows for uninterrupted testing cycles and faster results production: the terramechanics rig serves as an invaluable resource. The terramechanics rig can take several different measurements during tests. For this study the relevant measurements are the drawbar pull, which is the measured force in the direction along the soil vane, the normal load applied to the test wheels, the driving torque at the spindle caused by the wheel-terrain interaction, and the angular wheel position, which was used to measure the slip ratio. To obtain accurate, usable data, great care must be taken in preparing the test surface. Without a consistent soil preparation method, uniformity within the measurements can leave much to be desired in the data.

In this chapter, a general overview of the test equipment used in this study will be presented. The first section will discuss the instruments used to measure the relevant soil parameters. Then, the instrumentation and measurement devices on the terramechanics rig will be discussed. Following this will be a description of the terramechanics rig's design and functionality. The chapter will conclude with an in-depth look at the soil preparation method used to create terrain conditions consistent with those used at NASA GRC.

3.1 Description of the Test Equipment: Soil Measurement Instrumentation

The terrain conditions in this study must be similar to those on the Lunar surface and also consistent throughout all of the tests. In order to create such conditions, a soil preparation method was developed. To ensure accuracy and consistency with the desired terrain conditions, a Rimik CP40 II cone penetrometer (CPT) is used to measure the soil compaction gradient (G). Figures 3-1 and 3-2 show the disassembled penetrometer and fully-assembled penetrometer in use, respectively.

Figure 3-1. Disassembled Rimik CP40 II cone penetrometer in its case.

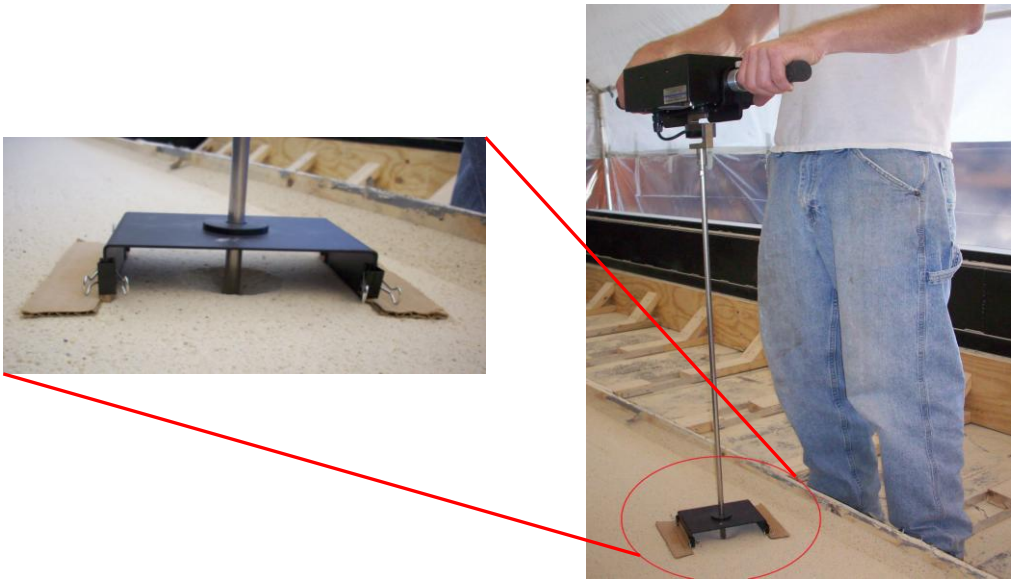

Figure 3-2. Assembled CP40 II cone penetrometer being used to check soil compaction.

The first step in doing so is to set the cone above the soil to be measured. The next step is to start recording data, after which time the cone is inserted into the soil. From this initial insertion, continue to apply a force on the two handles, causing the penetrometer to move downward while measuring pressure and sinkage. The maximum depth of the measurements can be set to a various range of values, and the increment at which the pressure measurements are taken can also be set manually. The CPT measurements are important because the soil compaction can be

used to determine the relative density of the soil. To meet the terrain conditions required for this study, a density of 1.67 g/cc (24% relative density) was used, and the corresponding compaction gradient was 3.5 kPa/mm with a standard deviation of $+/-0.5$ kPa/mm. The method for obtaining this testing condition will be discussed in the Chapter 4.

Determining the mechanical properties of any soil, such as the Reece stiffness parameters k_ϕ' and k_c', requires a bevameter to record pressure-sinkage and shear data. Bevameter tests were performed on the GRC-1 Lunar simulant at the NASA Glenn Research Center (NASA-GRC) in Cleveland, OH. In Figure 3-3 is a schematic of the table-mounted bevameter used at NASA-GRC to perform the pressure-sinkage and shear tests. The results of these tests can be seen in Appendix A, and the MATLAB code used to automatically calculate the stiffness coefficients can be seen Appendix B.

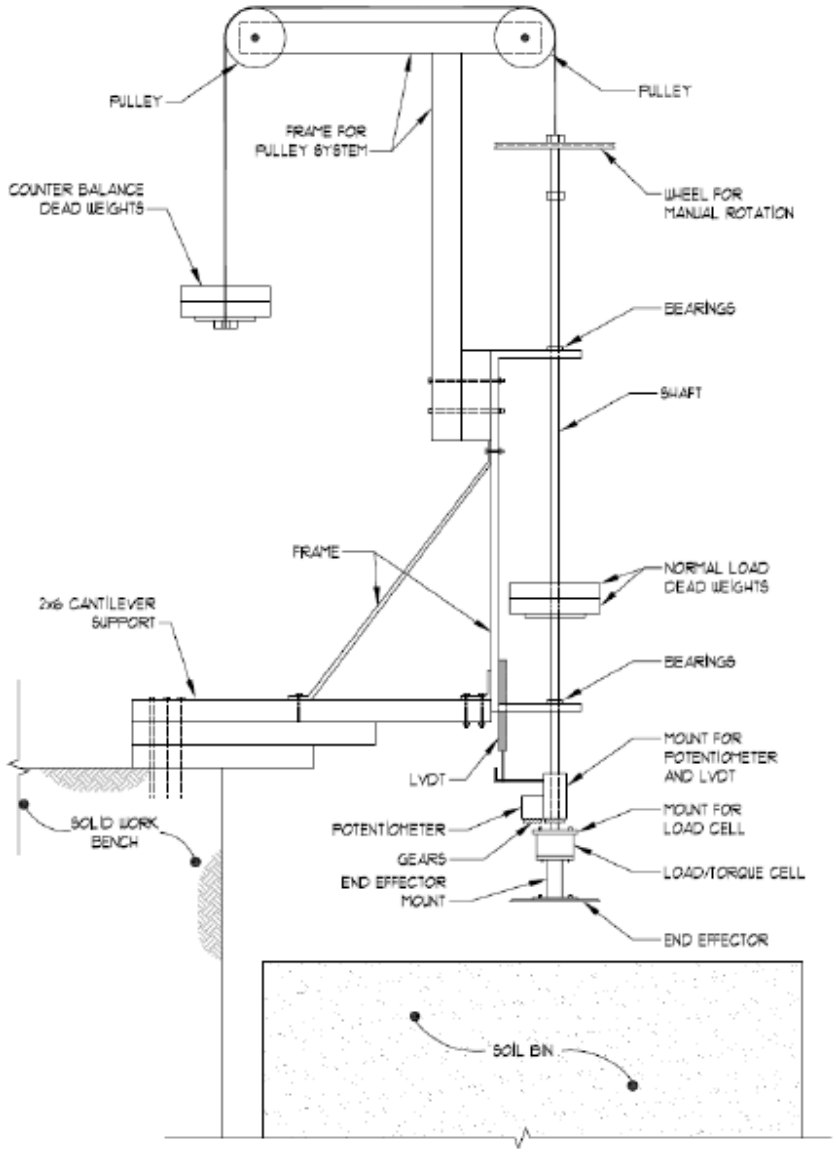

Figure 3-3. Labeled schematic of table-mounted bevameter used at NASA-GRC [19].

The bevameter shown in the figure above is mounted to a rigid table using wooden cantilever supports, to which the aluminum frame is attached. The instrument is capable of measuring both shear and pressure-sinkage data by adding and/or removing deadweights to the designated mounting positions on either the counter-balance or normal load ends of the cable-pulley assembly. The end effectors used for the data collection relevant to the model validated in this study were the flat plate, shown in Figure 3-3, and the shearing ring, as shown in Figure 3-4.

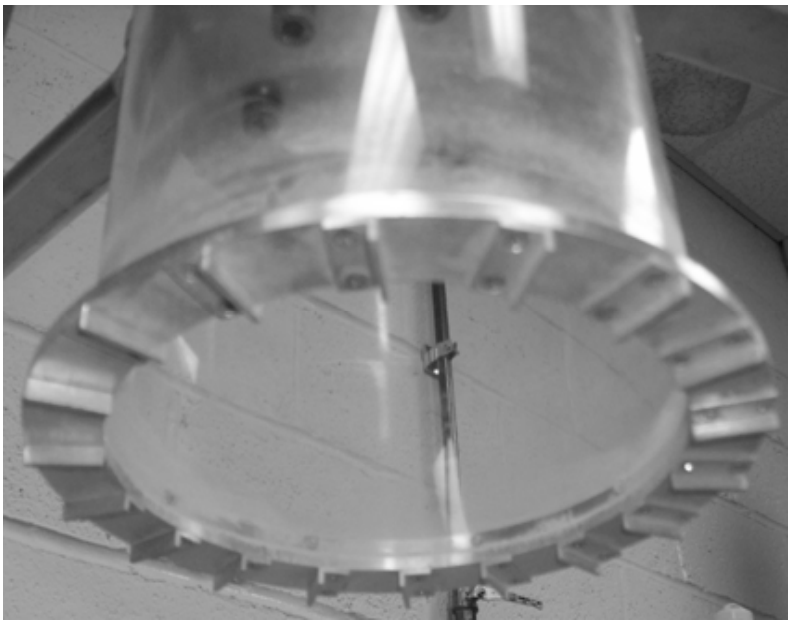

Figure 3-4. Shearing ring (with grousers) used in bevameter shear tests. The grousers were not used to collect the data used in the model for this document [19].

Unlike the flat plate, which required the effector mount for pressure-sinkage testing, the shearing ring was directly attached to the load/torque cell. To measure the normal load and/or torque applied to the soil surface, the load/torque cell was used. When performing pressure-sinkage tests, the vertical force pressing down on the sand surface was measured with the load cell. As the load on the sand was increased, the sinkage was measured using the LVDT. The shearing motion was executed by manually rotating the wheel located at the top of the shaft, as the torque applied to the sand was measured by the torque cell and the angular displacement was measured by the potentiometer. Shearing tests were performed under different, pre-determined normal loads. It is important to note that the pressure-sinkage and shear tests were not performed simultaneously [19]. The data sent from the load/torque cell was sent to an oscilloscope and saved for processing.

3.2 Description of the Test Equipment: Terramechanics Rig Instrumentation

A TekScan I-Scan 3150 pressure pad was used to measure the contact pressure distribution under each tested wheel. The pad was imbedded in the soil, at a depth of three inches; such a depth was selected to offset any boundary conditions created by the rigid support

on which the sensor rested. A picture of the pressure pad resting on its rigid, black plastic support is shown in Figure 3-5.

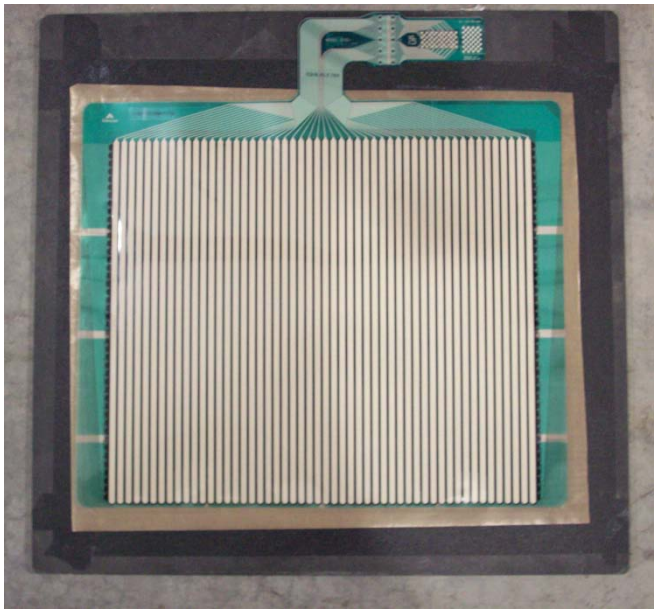

Figure 3-5. Uncovered TekScan I-Scan 3150 pressure pad.

The pad shown above is about 0.127 mm thick, with overall dimensions of 49.91 cm by 50.8 cm. The actual sensing region is 35.86 cm by 43.59 cm, which contains measurement grid of 44 by 52 sensing lines (2288 sensels). This provides 1.5 sensels per square cm of the sensing area. Two preventative measures taken to avoid shearing to damage the sensor were the placement of a thin piece of weaved-copper fabric at the pad-plastic support interface and positioning a thin sheet of translucent plastic on top of the sensor. In previous studies that implemented the TekScan pad, a final step to prevent any damage to the pressure pad was to place the entire pressure pad-plastic support assembly into a large plastic bag and seal the opening as to limit the amount of fine sand particulates entering the bag [20]. The plastic bag further reduced the risk of shearing damage to the pad, as well.

To measure forces and moments at the wheel hub, Kistler Instruments provided a P650 wheel force sensor [12]. The P650 wheel hub has the ability to make measurements of wheel forces on the three linear axes while measuring the moments about these axes, as well. This system uses piezoelectric effects (longitudinal and shear) within the hub and conditions the signals into units of force, moments, and angular position/velocity. From here, the signals are sent to the electronic control system, free of noise and interference. To prevent wear resulting

from contact between surfaces, the signals are transmitted via a near-field telemetry system. Wheels and tires being tested are mounted to the sensor, which is placed where brake components would normally be located, as shown in Figure 3-6, and is able to rotate with the wheel as the carriage as it traverses the length of the soil container.

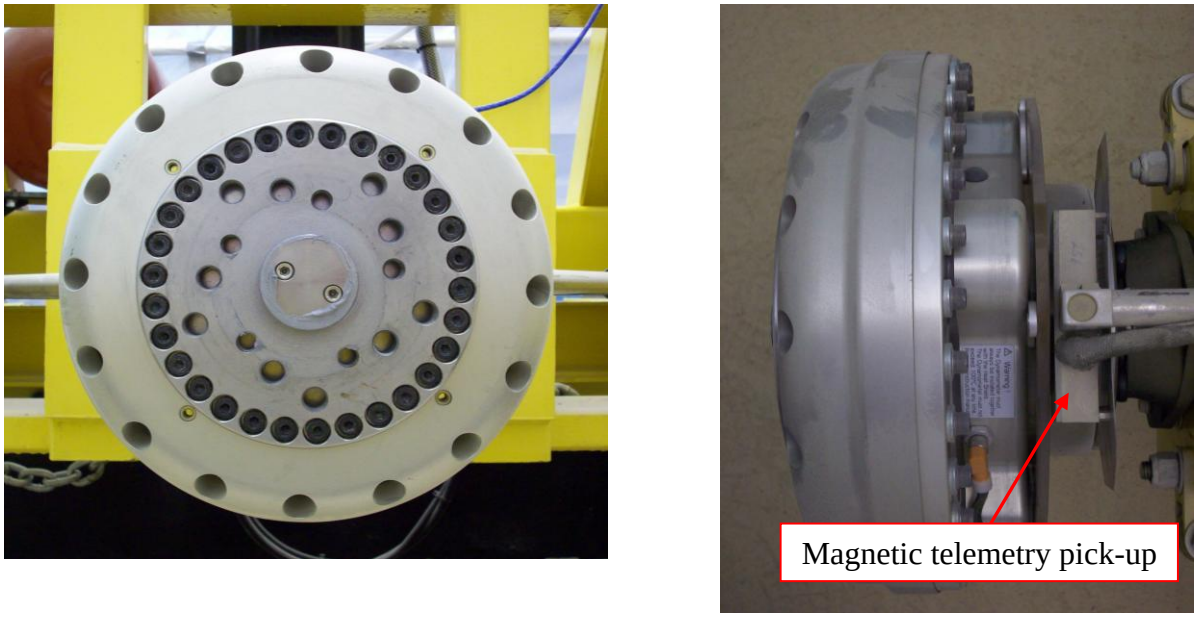

Figure 3-6. Kistler Instruments P650 wheel force sensor shown from wheel-mounting surface (left) and from above to depict near-field telemetry system (right).

The P650 wheel force hub is operated using a control emulator program installed on a PC. A screenshot of the longitudinal, lateral, and vertical forces (in Newtons) is shown in Figure 3-7.

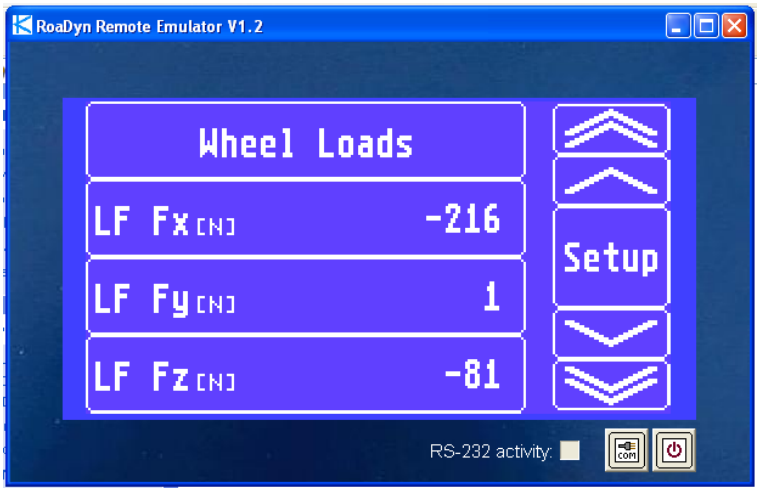

Figure 3-7. Screenshot of Kistler control emulator.

Because tire deflection and wheel sinkage are very important measurements to make when performing terramechanics studies, some means of acquiring these measurements is needed. To account for this, a Celesco string potentiometer is installed on the terramechanics rig. This potentiometer is mounted to a rigid section separated from the vertical motion of the wheels, and measures the change in distance from the original length of the string. The string, itself, can extend up to fifty inches. The string pot has the capability of measuring rigid wheel sinkage in soft soils, flexible wheel deflection on rigid surfaces, and a combination of the two in which the combined sinkage and deflection of flexible wheels can be measured. Figure 3-8 provides a picture of the string potentiometer as the body sits on the upper, unmoving section on the rig, and the string is attached to the vertical carriage.

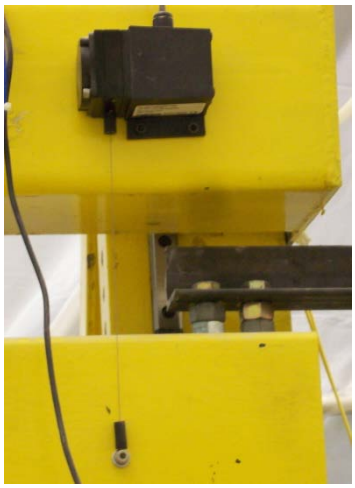

Figure 3-8. Celesco string potentiometer as it is mounted on the terramechanics rig.

The measurements made by the Kistler wheel force hub and by the string potentiometer are recorded using an LMS data acquisition (DAQ) system. The SCADAS III front-end contains the circuitry needed to process input voltage signals, and converts these signals into units of force, moment, angular position/speed, and linear distance. All relevant data can be saved for further processing. A screenshot of the LMS-created plots is shown in the figure below.

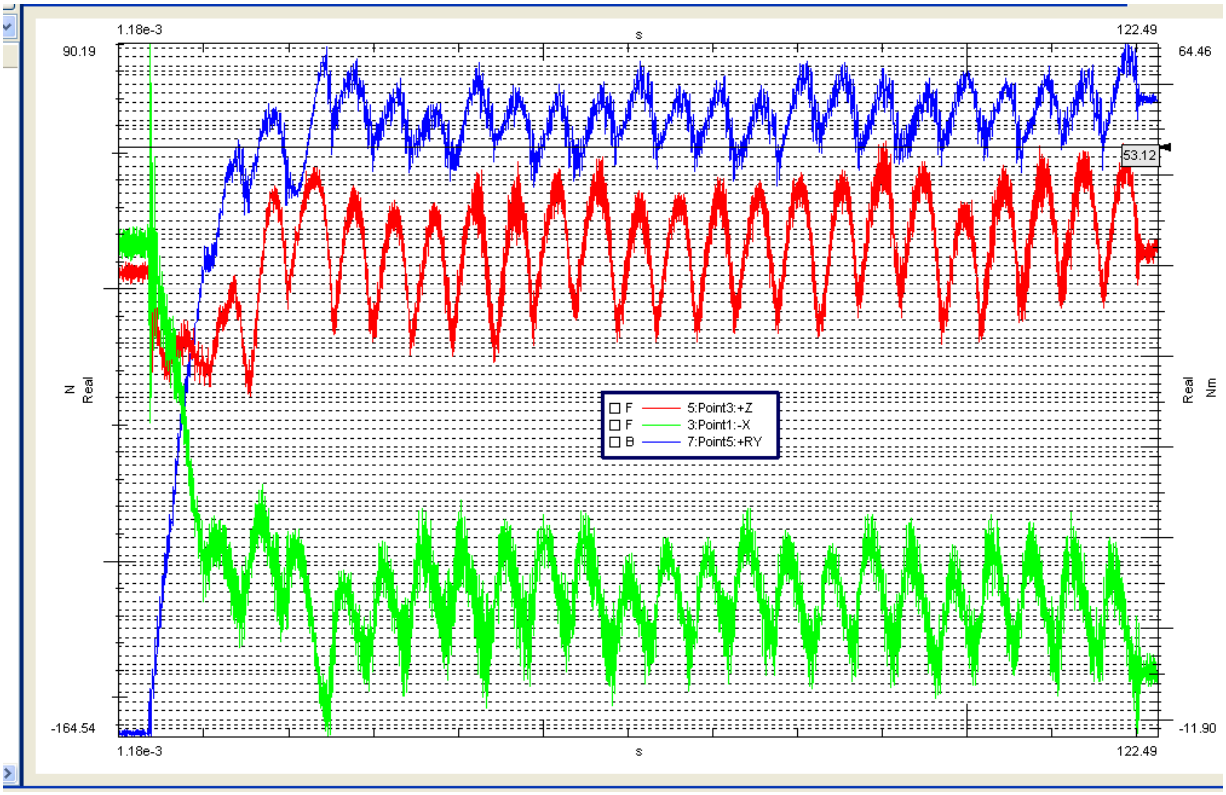

Figure 3-9. Screenshot of plots created with the LMS Test.Lab 8.

A valuable set of tools that has recently been added is the set of three digital video cameras, one of which is already on the rig, while the remaining two will be added in the very near future. The mounted camera is positioned within a protective casing to view the back of the wheel being tested. One of the remaining two cameras will be mounted on outer side of the wheel such that entry and exit angles of a tire/wheel in soft soil can be observed. The other camera will be suspended above the wheel to observe steering maneuvers in future studies.

3.3 Description of the Test Equipment: Terramechanics Rig Overview

The terramechanics rig, shown in Figure 3-10, at the Virginia Tech Advanced Vehicle Dynamics Lab (AVDL) is comprised of three functional components: Motion and actuation, Controls, and Hardware [12].

Figure 3-10. Terramechanics rig at AVDL, shown with pneumatic tire on rigid metal surface [12].

The Motion and Actuation area involves directional movements along the soil vane, in the lateral direction of the container when a toe angle is input, and in the vertical direction allowing for movement as a function of variations in terrain height. Along with the linear movement of the carriage, the second function of the Motion and Actuation sector is to apply torque to the wheels for accelerating/braking and steady-state testing: the wheel/tire rotational velocity and carriage straight-line velocity can be independently controlled to induce a preset wheel slip.

The Controls function includes the adjustable components of the terramechanics rig. One such component is variable normal load from very light loads, i.e. loads seen by the Lunar exploration vehicle wheels tested in this study, up to much heavier loads, such as those seen by large sport utility vehicles. To account for lighter loads, a counterweight system was originally installed on the carriage; however, friction within the cables from which this assembly was suspended was too great to overcome without losing its effectiveness. To resolve this friction issue, a pair of air springs has been installed. Besides ridding the carriage of a frictional source, the air springs also reduce the overall inertia of the carriage. Both the counterweight and the air-spring designs can be seen in Figure 3-11.

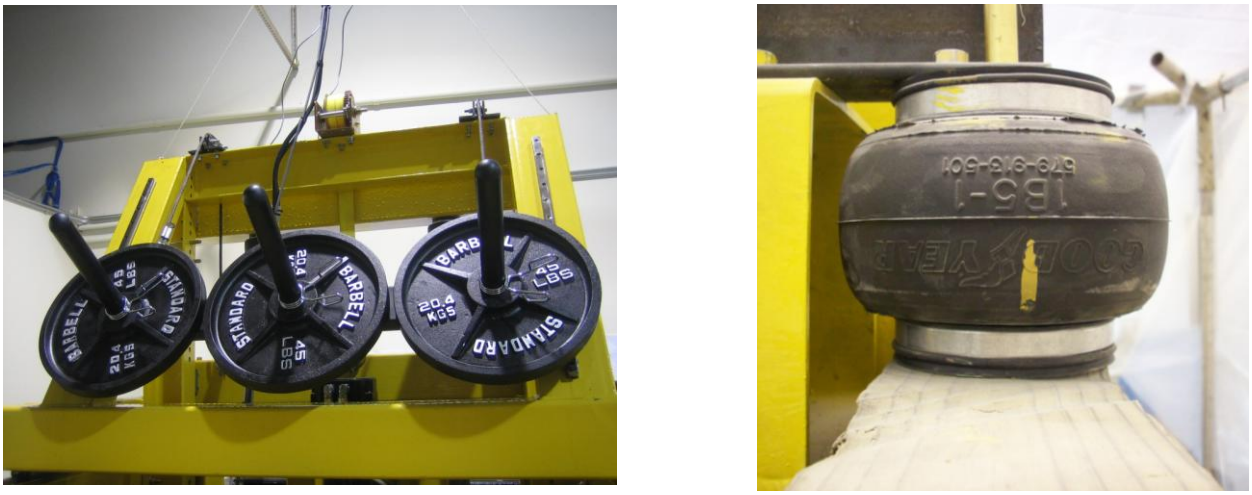

Figure 3-11. Original counterweight assembly (left) and new air-spring design (right).

Another component of the Controls function is the adjustability of the wheel hub in the vertical direction. The terramechanics rig has the capacity to test wheels/tires ranging from 20 inches to 37 inches in diameter. A third component of the Controls function is the ability of the carriage to traverse the soil bin along the longitudinal direction in either direction for any distance. This allows for soil preparation to be carried out in a regimental and repeatable fashion. The last component of the Controls functional area is the adjustability of the camber and toe (steering input) angles. The camber and toe angles can be adjusted from -8° to +8° and from -45° to +45°, respectively. Figure 3-12 provides an overhead view of these adjusters.

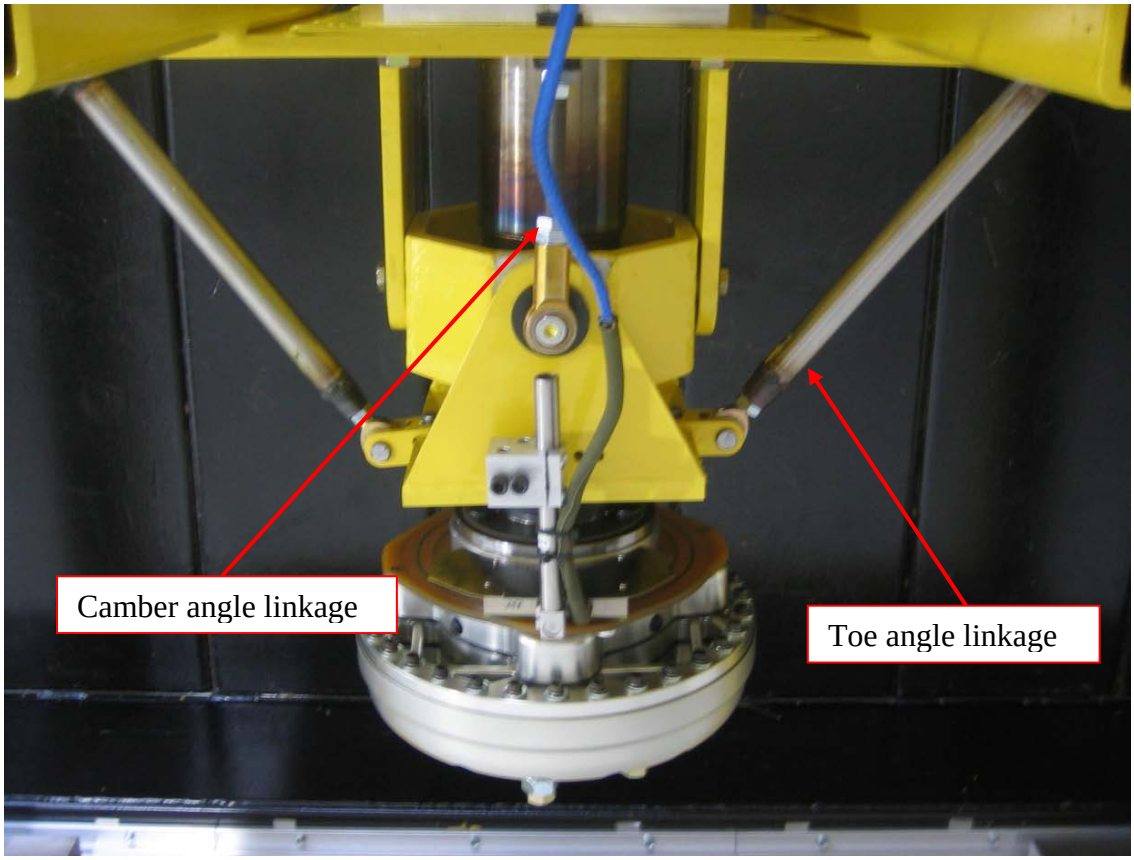

Figure 3-12. Camber and toe angle adjustment is done using the tie rod linkage (top view) [12].

The Hardware functional block of the terramechanics rig is comprised of the soil vane, the carriage for motion in the longitudinal and lateral directions, and the sensors and DAQ equipment discussed in the preceding section [12]. The soil vane's primary purpose is to create, maintain, and store various soils and surfaces. Even while one type of surface is in use on the upper level, the bottom level, shown in Figure 3-13, of the vane is able to store a second type of soil.

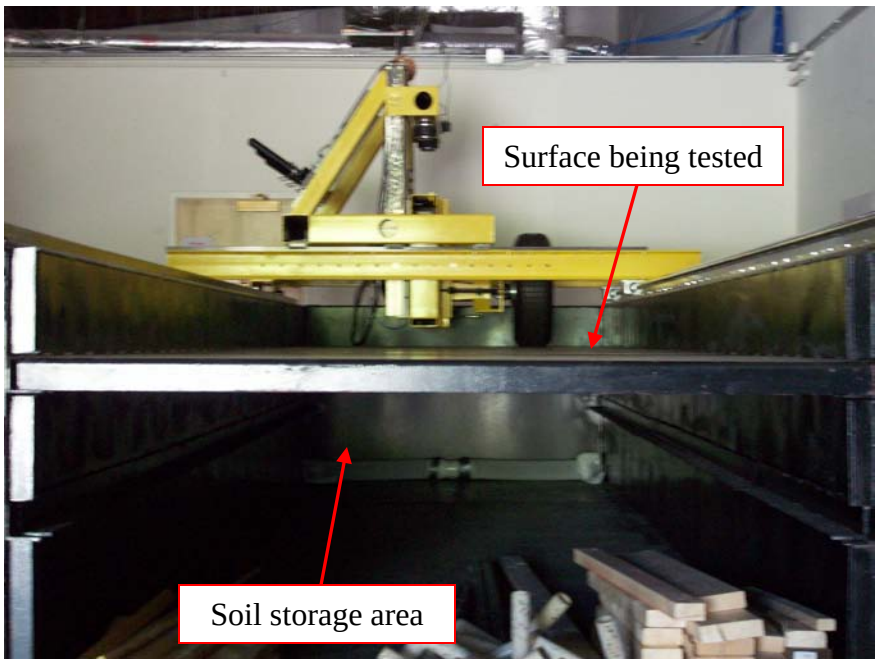

Figure 3-13. Volume below the testing surface can be used to store a second soil.

The carriage, shown in Figure 3-14, serves the purpose of supporting the test wheel/tire together with the motor and gearbox.

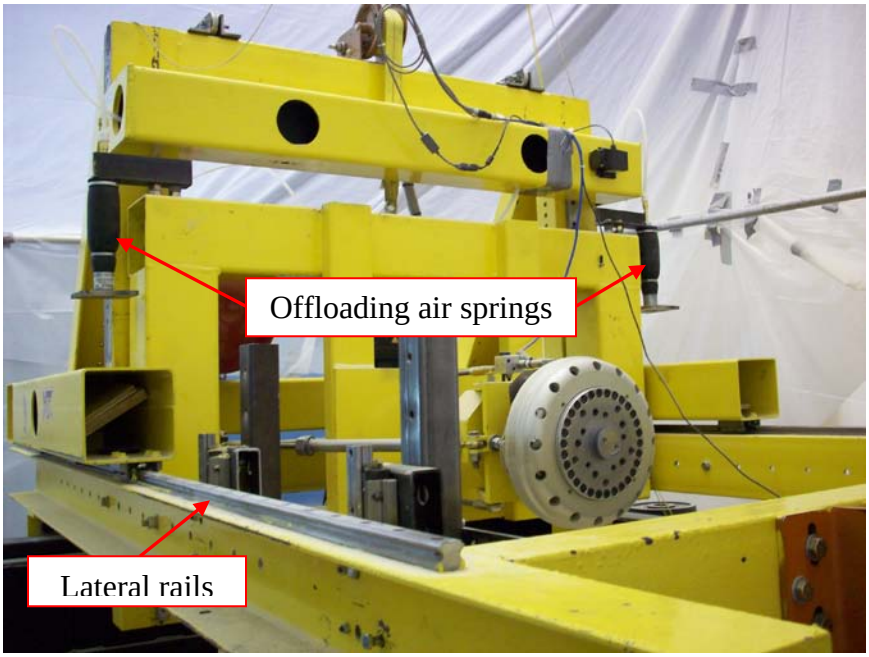

Figure 3-14. Carriage on which test wheels/tires are mounted and tested.

The carriage also has the laterally-aligned rails which allow the wheel/tire move side-to-side when executing steering maneuvers. The aforementioned air springs are labeled in Figure 3-14. When testing at heavier normal loads, these springs can also be oriented in a manner such that normal loads can be applied. Moving the carriage requires a motor and gear reduction combination that creates enough power to overcome not just the combined motion resistance of the carriage and any wheels/tires, but also the inertia of the carriage at various velocities and accelerations. The motor-gearbox combination consists of an 8.6-kW motor fit to a 23.08:1 gear reduction. The output of the gearbox connects to the drive pulleys via a pair of drive shafts. It should be noted that these drive shafts are oriented at a slight angle in the horizontal plane, causing a very small amount of secondary torque due to the universal joints at each end. The drive train system is shown in Figure 3-15.

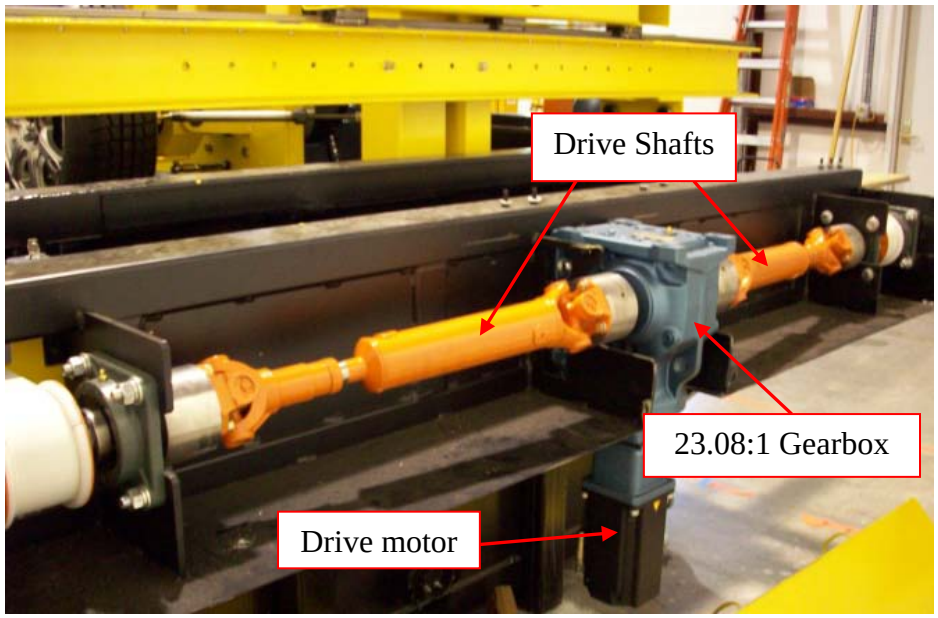

Figure 3-15. Drive train used to propel the carriage along the terramechanics rig.

The drive pulleys are used to convert the drive train's rotational motion to the carriage's translational motion via two belts attached to the carriage and a pair of idler pulleys located at the end opposite the drive train. Figure 3-16 depicts how the belts are attached to the carriage.

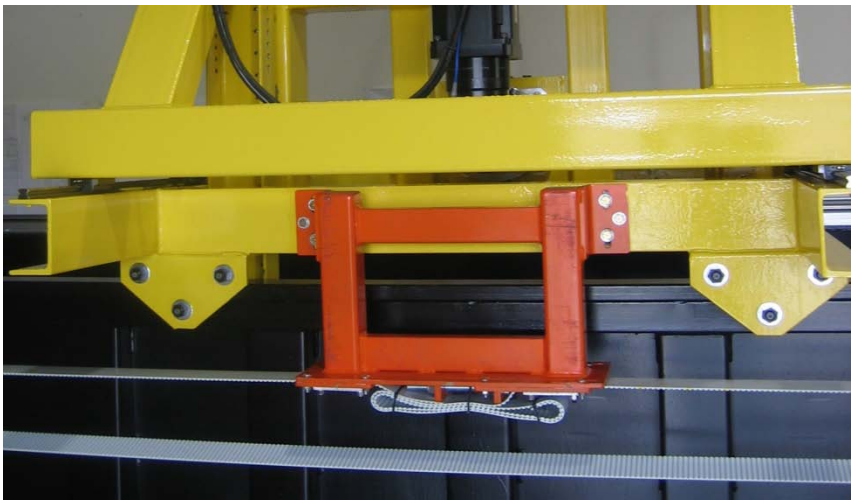

Figure 3-16. Depiction of how drive belt attaches to the carriage [12].

A master-slave motor combination is used to control both of the motor-gearbox sets implemented on the terramechanics rig. A diagram of this master-slave setup is shown in Figure 3-17, and a picture of the setup is shown in Figure 3-18.

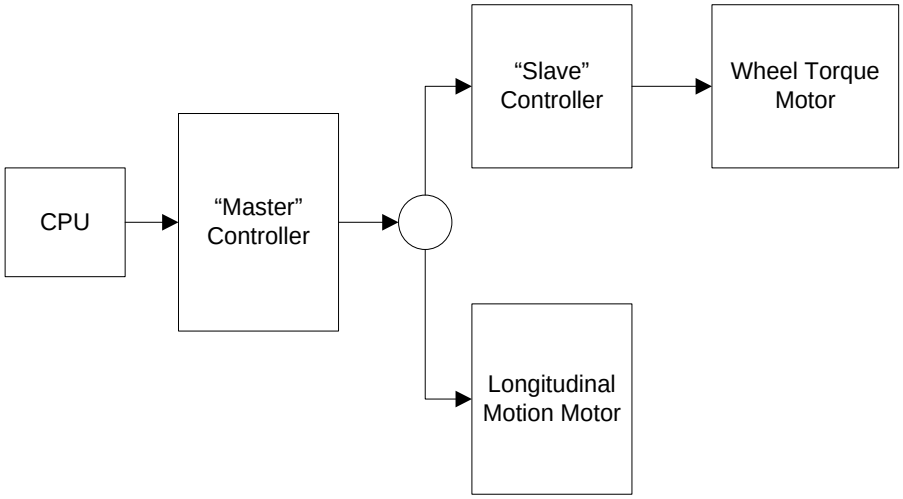

Figure 3-17. Schematic of the master-slave controller configuration [12].

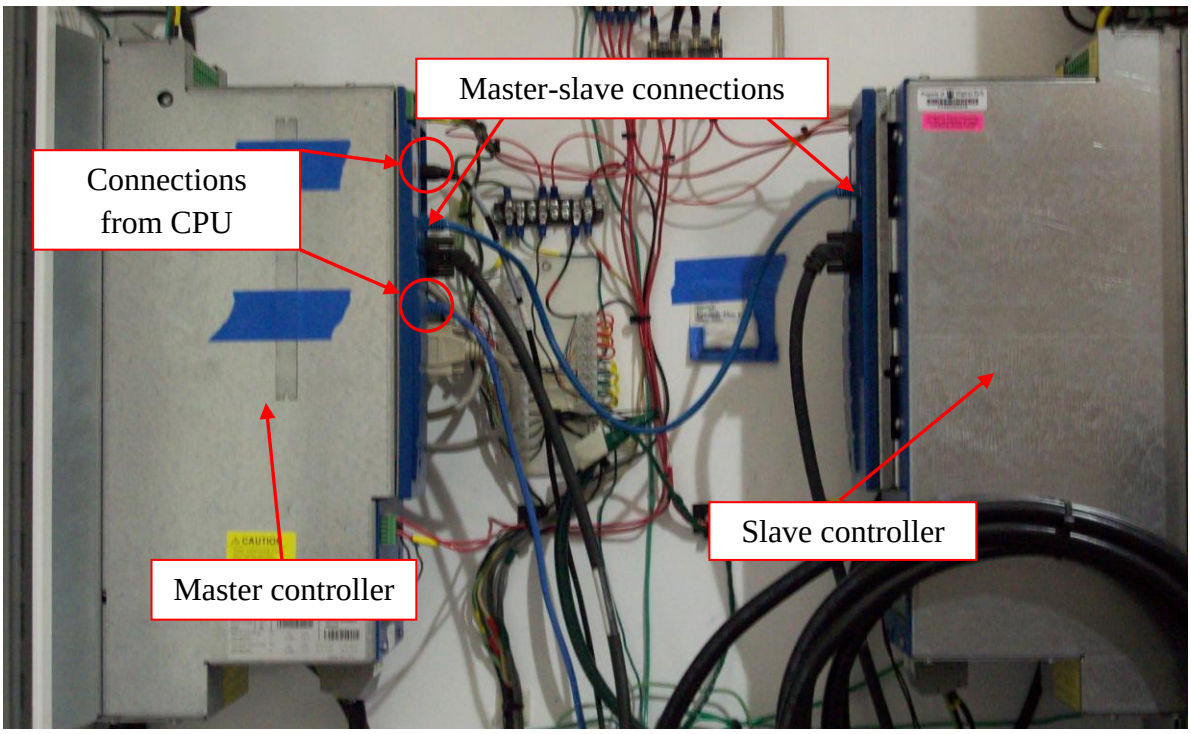

Figure 3-18. Master-slave controller configuration.

To control the master-slave setup, a PicPro ladder logic programming code is used. The code does not use SI units within it, so conversion factors are required. Instead, the units employed for velocity are dubbed "Ladder Units per minute" (LU/min). Table 3-1 presents these conversion factors.

Table 3-1. Conversion factors from controller units to SI units.

Controller (Type of motion)	Code Velocity (LU/min)	SI Velocity
Master (Translational)	34515.9285	1 cm/s
Slave (Rotational)	572957.7684	1 rad/s

With the vast functionality of the terramechanics rig, a diverse range of tests can be run, proving the rig to be an invaluable asset to understanding tire-terrain interactions. A user's manual of basic operating procedures of the terramechanics rig is located in Appendix C of this document.

3.4 Description of the Test Equipment: Soil Preparation Method

One of the most important parts of testing on any off-road terrain is the preparation of the soil. In this particular study, a method of grooming the soil to match conditions consistent with NASA GRC was developed and implemented. The density of the GRC-1 Lunar simulant, to

which the soil was prepared, was 1.67 g/cc (24% relative density), and was verified with a compaction gradient of 3.5 kPa/mm with a standard deviation of $+/-0.5$ kPa/mm. Achieving this density required careful execution of the preparation steps; the protocol for this preparation is thoroughly discussed in the following paragraphs.

The first step in the soil preparation process is to loosen the soil using a flat shovel. The shovel must be inserted into the soil so that the blade is held perpendicular to the terrain, as shown in Figure 3-19. Inserting the shovel at this angle ensures that no sand will be compacted by the blade during the loosening step.

Figure 3-19. Angle at which shovel must be inserted perpendicular to the terrain. It should be held at such an angle as it is inserted farther.

The blade must reach the bottom of the soil, or as deep into the terrain as possible. Once the shovel is as deep as possible, the handle should be pulled towards the operator such that the soil is lifted up and its stress history, erased. From here the handle should be pushed away from the operator and lifted out of the soil. Then, moving the shovel to backwards (toward the operator), roughly two to three inches, to a new insertion point, the loosening step should be repeated. This process should be repeated over the length of the soil. Once the first pass along the length of the terrain has been made, one should return to the starting point and begin loosening another line

next to the first pass; this process is repeated on both sides of the first line. Figure 3-20 show how the "destressed" terrain should appear after the first and final loosening pass.

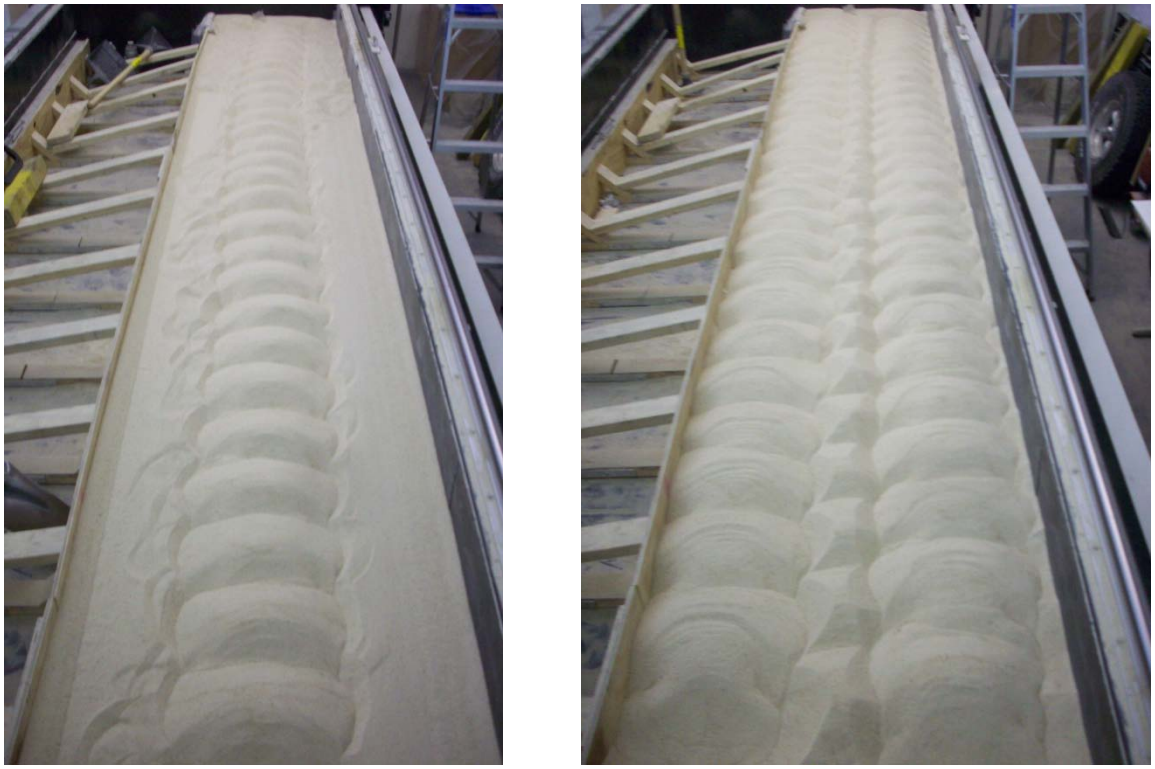

Figure 3-20. Loosened soil. After shoveling, it should look similar to these after the first pass (left) and final pass (right).

The next step in the soil preparation procedure is to rake the terrain so that the ripples seen in Figure 3-20 are removed and a relatively level terrain profile is obtained. Figure 3-21 depicts the raking step.

Figure 3-21. Rake being dragged along the top of the soil on first pass.

When executing the raking step, the rake should be pulled at an angle parallel to the terrain. This will allow for even soil distribution along the length of the test lane. Three passes should be made with the rake, with two passes over the rippled soil and the third, in the middle of the first two. The resulting terrain should look very much like that in Figure 3-22.

Figure 3-22. Terrain profile created after three raking passes.

The next step in the preparation protocol is to level and compact the so-called “run-up” section of the test lane. This portion, which is roughly one-and-a-half meters long, cannot be prepared in the same manner as the rest of the test lane because the terramechanics rig carriage blocks access to this section. Therefore, during testing it was used as a section over which the test wheels could reach steady-state. The downfall to having this portion is that it shortens the length of usable test region; methods are currently being devised to make this section usable. Nevertheless, the terrain in this part still needs to be prepared somehow. This area is leveled by hand using the scraper shown in Figure 3-23.

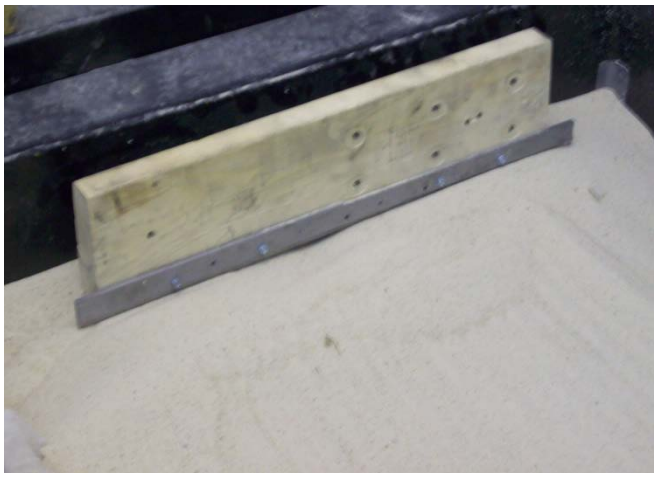

Figure 3-23. Blade used to manually level "run-up" section of test lane.

A bubble-level is placed on the sand to check that the terrain is level throughout the length of this section. The next step in preparing the "run-up" section is to compact the terrain. A hand tamper is dropped, in an overlapping pattern, onto the soil from a height of roughly 10 cm. Figure 3-24 shows this process being carried out.

Figure 3-24. Hand tamper held at height from which it is dropped.

The tamper should be dropped in an overlapping pattern, such that it is moved one-half its width after each drop, traveling from one side of the test line to the other, then moving along the length

of the test lane roughly one-half the tamper's width, and repeating the side-to-side pattern. The "run-up" section should look similar to Figure 3-25 when it is completely leveled and compacted.

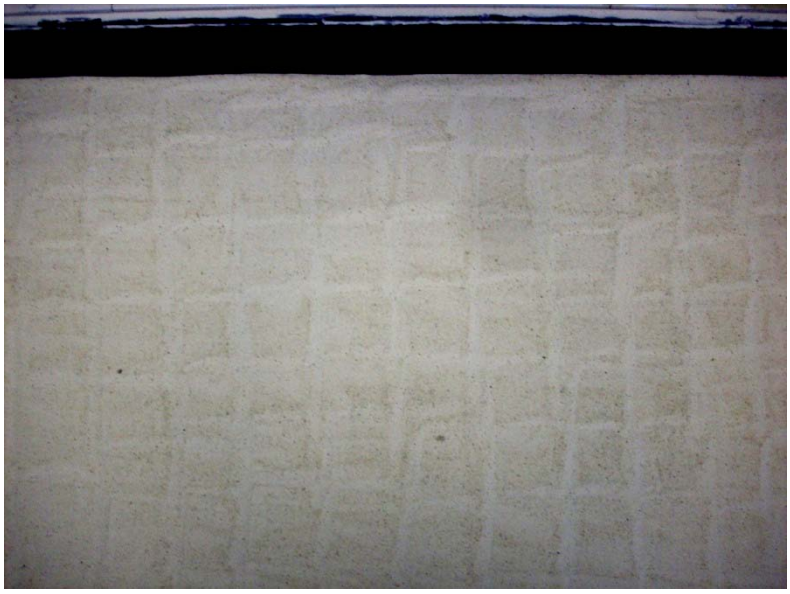

Figure 3-25. Overlapping pattern created by dropping tamper.

After the "run-up" region is created, the next step is to level the usable test length. This is done using a leveling blade attached to the terramechanics rig, which is used to automate the soil preparation process. This blade can be adjusted to a variety of heights, and is shown out of the soil and in use in Figures 3-26 and 3-27, respectively.

Figure 3-26. Blade used to level the test lane.

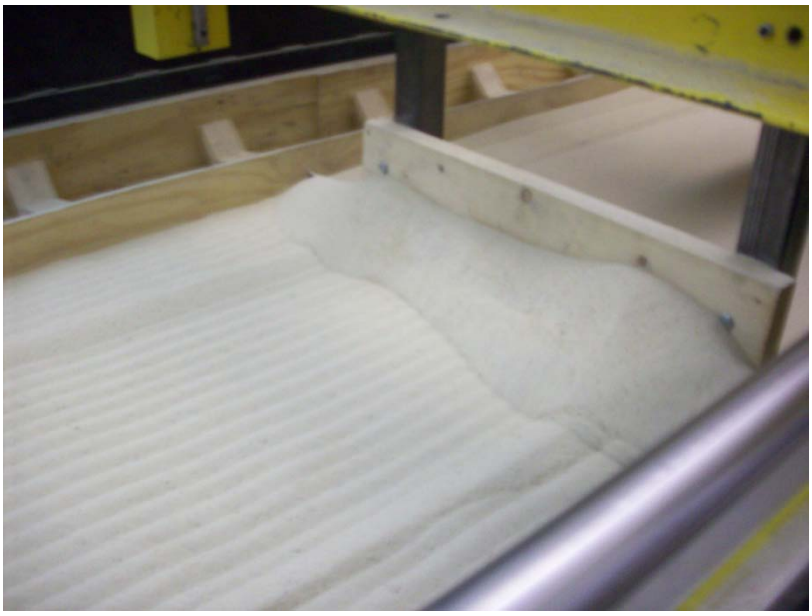

Figure 3-27. Leveling blade immersed in soil while leveling the terrain.

To maintain a non-compacted soil condition, the blade is set to predetermined height so that the board to which it is attached does not rest on the soil at any point in the process. The results of this step yield a level, unstressed soil, as shown in Figure 3-28.

Figure 3-28. Results of soil leveling procedure.

The fourth step in the soil preparation procedure is to compact the usable length of the test lane. This is done using a lawn roller filled with the GRC-1 sand. The lawn roller is first lowered into the soil at the end of the test lane where the carriage starts its motion. Then, the roller is pulled to the opposite end of the rig using a Warn RT-15 ATV winch. Figure 3-29 shows how the winch is used to pull the roller from one end of the test lane to the other.

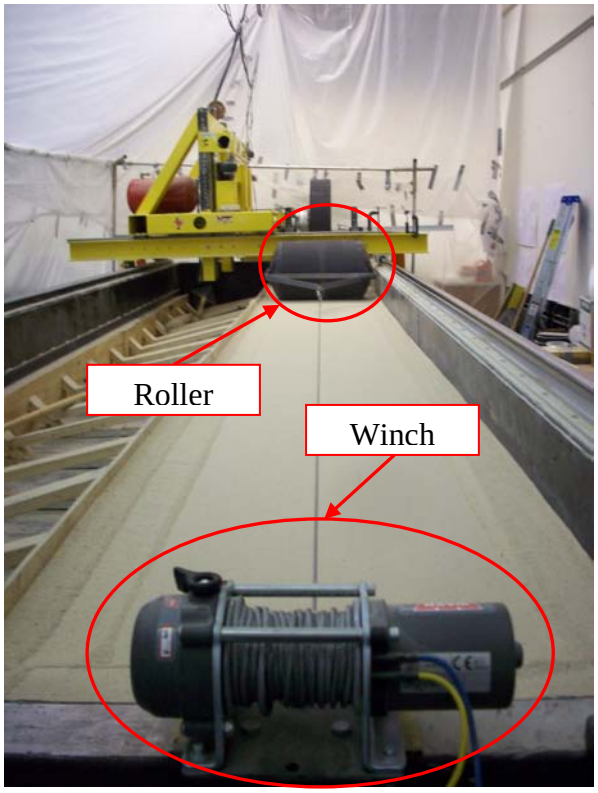

Figure 3-29. Winch and roller used to compact the soil.

Using the Warn winch allows the roller to be pulled at a constant speed, while also keeping the winch cable at a constant angle relative the ground. Once the roller has been pulled to the end of the test lane, it is removed from the soil. Figure 3-30 shows how the compacted terrain appears following the compaction step.

Figure 3-30. Test lane as it appears after being compacted with law roller.

The final step in the soil preparation process is to check the soil compaction gradient using the cone penetrometer. This procedure was discussed in section 3.1. Once the soil density has been confirmed, the test may begin. The steps described above must be carefully executed before each wheel test. This method has proven to be an accurate and repeatable means of achieving the desired soil density. From the rigid wheel tests that have been performed for this study, the average soil compaction gradient was 3.6 kPa/mm with a standard deviation of +/- 0.194 kPa/mm, which is well within the desired range of values.

3.5 Description of the Test Equipment: Summary

This chapter has outline the vast measurement tools utilized during the course of this study. The first section highlighted two soil measurement devices: the cone penetrometer used to measure soil compaction and the bevameter used to perform pressure-sinkage and shearing tests on different terrains. The cone penetrometer was used at the VT AVDL to ensure proper soil density when tests were carried out, and the bevameter was utilized at NASA-GRC to characterize the GRC-1 Lunar simulant soil.

The section portion of this chapter discussed the instrumentation with which the terramechanics rig has been outfitted. The TekScan I-Scan 3150 pressure pad was used to

measure contact pressure applied by the wheels covered in this study. The next instrument, and perhaps the most notable, was the Kistler RoaDyn P650 Wheel Force sensor. This device has the capability to measure forces in the *x*-, *y*-, and *z*-directions, as well as moments about each of those axes, and proved invaluable in this study. Next was the Celesco string potentiometer. While the string pot was not used during this particular study, it will most certainly be used in future projects. The information gathered using the Kistler sensor and string pot is fed into the LMS SCADAS III data acquisition system, and accessed via the LMS Test.Lab 8 user interface.

The next segment provided a general overview of the terramechanics rig's design and functional breakdown. The controls were discussed, as well as the axes of motion. Two normal-load-setting methods were introduced, as well. The motors used to propel the carriage's translational movement and the test wheel's rotation were described. The section ended with an explanation of the master-slave controller setup, followed by a table with conversion factors used to convert controller's units into SI units.

The final part of this chapter discussed the soil preparation method that was implemented for this study. The four basic steps included the following: 1) loosening the soil with a shovel, 2) raking the churned soil, 3) leveling the raked soil such that the surface is smooth and level, and 4) compacting the soil to the proper level using the compaction roller and Warn winch combination. The final step was to check for correct soil density using the cone penetrometer.

4. Design of Experiment

In this chapter the design of experiment will be described for both the single-wheel tests and the 4x4 vehicle tests. The single-wheel tests were performed with the terramechanics rig at VT AVDL using the controlled-slip technique discussed in Chapter Two. The 4x4 vehicle tests were performed at NASA Glenn Research Center (NASA GRC) in Cleveland, OH using the controlled-pull technique. Two sets of test conditions were assigned to the two test facilities, which include slip ratios and normal loads. The soil was prepared to similar relative densities (*RD*) at the two locations.

It should be noted that this chapter does not provide a full statistical design of experiment due to specifics of the study. Instead, this study is more of a parametric study. Nonetheless, this section has been called the Design of Experiment within the context of this study. The four different test wheels could be considered the experimental units of this experiment, with the drawbar pull and driving torque as the observational units. The changes to the wheel parameters, the four normal loads, and the slip ratios can all be considered the treatments for this study.

4.1 Design of Experiment: Single-wheel Testing

4.1.1 Single-wheel Experimental Conditions

The single-wheel tests performed at the Virginia Tech Advanced Vehicle Dynamics Lab were done using the terramechanics rig described in the preceding chapter. The wheel slip was controlled in a programmed-increasing manner, such that all the values were covered within the desired range. The values of slip ranged from -15% to 60%, and were unevenly spaced among 21 points. While earlier wheel tests discussed in [10] were performed by keeping wheel speed constant and decreasing carriage speed at a constant rate, at VT a different means of increasing slip was introduced. In contrast to the methods used in [10], the carriage speed was held at a constant 5 cm/s, and the wheel speed was increased using a step-wise pattern. The tests consisted of multiple slip ratios per trial for the rigid wheels; however, due to the dynamics of the spiral wheel, each of the tests for this wheel was carried out at a single slip ratio. The slip ratios of which the tests were run were:

$$s_d = [-15, -10, -5, -3, -1, 0, 1, 3, 5, 10, 15, 17, 19, 20, 21, 23, 25, 30, 40, 50, 60]\ \%$$

Shown in Figure 4-1 is a diagram showing how the slip is a result of the tangential velocity of the radius of the wheel directly below the wheel center (ωR) and the translational forward velocity at the wheel center (V_x).

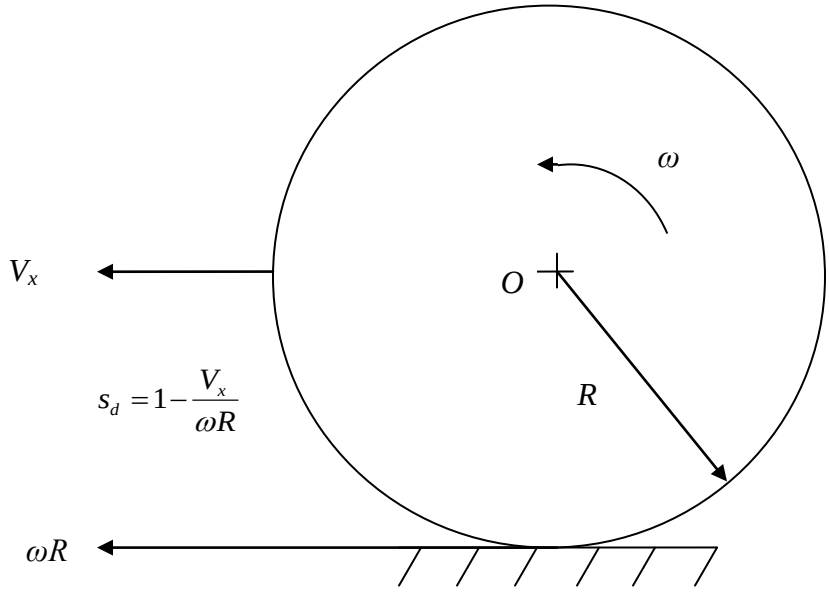

Figure 4-1. Diagram showing use of relative velocities to get slip ratio.

When testing the rigid wheels, all the slip ratios were used at each of the four normal loads. These loads ranged from 57 to 114 lb_f (253.5 to 507.1 N), which is approximately from 100% to 200% of the nominal load of the original Lunar Roving Vehicle (LRV) wheels. The four normal loads are shown here:

$$F_z = [57, 70, 80, 114]\ lb_f = [253.5, 311.4, 355.8, 507.1]\ N$$

It should be noted, however, that the flexible (spiral) wheel was only subjected to the 57-lb_f (253.5-N) load.

The desired relative density of the soil for both the single-wheel and 4x4 tests were equal. The density was 1.67 g/cc, or 24% relative density. Therefore, the compaction gradient needed to be 3.5 kPa/mm +/- 0.5 kPa/mm. Using the cone penetrometer at AVDL, it was found that the mean compaction gradient averaged over all of the tests was 3.6 kPa/mm +/- 0.194 kPa/mm and thus, well within the desired limits.

4.1.2 Single-wheel Experimental Procedure

At the beginning of each testing session, the terramechanics rig was powered up, and the Kistler hub was allowed to warm up for 15-30 minutes. This device requires a warm-up time due to the nature of its piezoelectric sensors, which are temperature-dependent and need to reach ambient temperature before accurate measurements can be made. This start-up procedure is thoroughly discussed in the Terramechanics Rig Operations Manual, which can be found in Appendix C of this document. While the rig was warming up, the soil preparation procedure discussed in Chapter Three was executed. Once the correct relative density had been obtained, the next step was to set the DC (signal) offset of the Kistler wheel force sensor. This step is discussed in the Operations Manual.

Next, the normal load was set. The combined weight of the wheel and Kistler sensor ("hanging" weight) was accounted for so that the correct normal load could be applied. Once the sensor-wheel weight had been noted, the difference between the desired normal load and the hanging weight was determined, as shown in equation (4.1) below, with a desired normal load ($F_{z,d}$) and a hanging weight (W_h) of 507.1 N and 203 N, respectively:

$$F_z = F_{z,d} - W_h = 507.1N - 203N = 304.1N \tag{4.1}$$

The value of F_z was applied to the wheel by setting the air pressure in the air springs described in Chapter 3. This was done by filling the on-board air tank, shown in Figure 4-2, and slowly bleeding the air out until the load was at the desired value.

Figure 4-2. On-board air tank used to set apply normal load to the wheel. The air tank was filled prior to each test run.

The valve connecting the tank to the two air springs was left open, allowing air to freely flow between the reservoirs. The idea behind this was to allow the wheel to travel vertically with variations in the terrain profile while keeping the normal load constant.

After setting the wheel load, the next step was to program the wheel speeds such that the desired slip ratios could be achieved. Using the slip ratio equation, the translational carriage speed (5 cm/s), and the radius of whichever wheel was being tested, a spreadsheet with the desired angular wheel velocities was created. An abbreviated sample of this sheet is shown in Table 4-1 below, including the converted controller speeds in Ladder Units per minute (LU/min). Recall that in Chapter 3 the conversion factors were provided.

Table 4-1. Sample spreadsheet used to set angular wheel velocities.

Desired Slip	Wheel Speed (rad/s)	Wheel Speed (LU/min)
-0.15	0.109	62270
-0.1	0.114	65101
-0.05	0.119	68201
-0.03	0.121	69525
-0.01	0.124	70902
0	0.125	71611
0.01	0.126	72334
0.03	0.129	73826
0.05	0.132	75380
0.1	0.139	79568
0.15	0.147	84248
0.17	0.151	86278
0.19	0.154	88408
0.2	0.156	89513
0.21	0.158	90647
0.23	0.162	93001
0.25	0.167	95481
0.3	0.179	102301
0.4	0.208	119351
0.5	0.250	143222

Note: The wheel radius for this example is 15.75 in. (40.005 cm).

The next step in the test procedure was to perform a walk-around of the terramechanics rig to make sure there were no obstructions to the motion of the carriage and wheel. Once this has been done, the test was started. Prior to starting the test, the LMS DAQ system began recording, as a stopwatch was simultaneously started. The stopwatch was used to record the times at which the wheel speed was changed to make data processing more straight-forward. The relevant data being recorded during these single-wheel tests were normal load, drawbar pull, driving torque, and wheel angle. While drawbar pull normally requires a load cell separate from the test equipment, because the wheel carriage is translating under its own power, the resistance forces acting opposite the direction of motion are cancelled out, leaving only the drawbar pull to be measured at the wheel center.

Then the test was run. Once each test trial was completed, data recording and the stopwatch were stopped at the same time, the data was saved for further processing, and the wheel was lifted off of the surface. Between the three rigid wheels, a total of 35 tests were performed; since the spiral wheel could only be tested for one slip ratio at a time, 21 tests were

performed for it to acquire the desired data. A picture of the 20-in. x 7-in. wheel is shown during a test run in Figure 4-3 below.

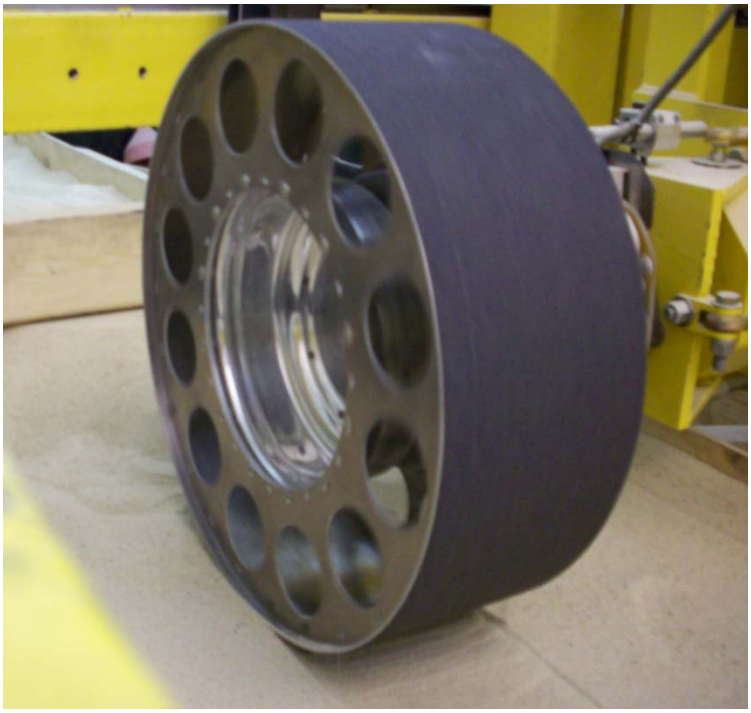

Figure 4-3. Photo of 20-in. x 7-in. rigid wheel during test, with a slip ratio of 60%.

4.2 Design of Experiment: 4x4 Vehicle Testing

4.2.1 4x4 Vehicle Experimental Conditions

The 4x4 vehicle tests were performed at NASA Glenn Research Center (NASA GRC) in Cleveland, OH using the controlled-pull technique. The testing facility is shown in Figure 4-4.

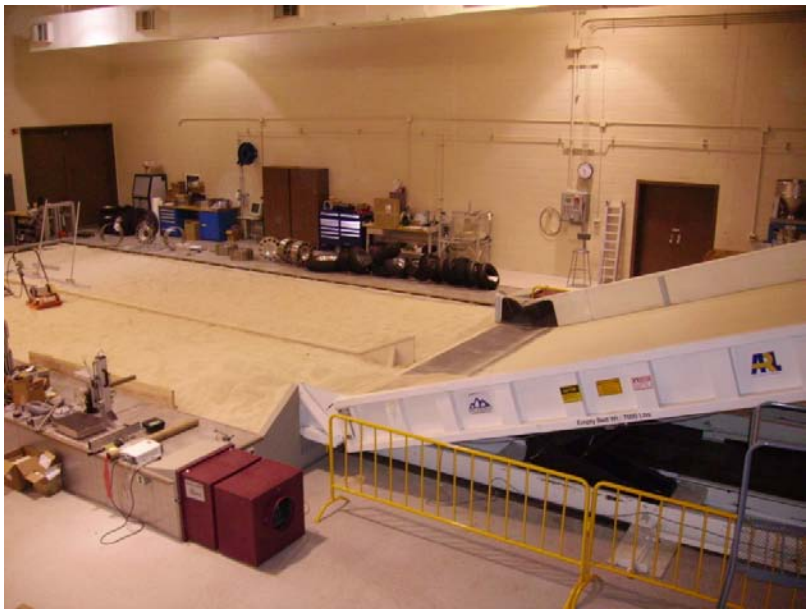

Figure 4-4. NASA GRC 4x4 vehicle testing facility.

The controlled-pull method involved spinning the vehicles drive wheels at a known constant speed, and incrementally increasing the force pulling against the vehicle's motion in a step-wise manner using a drawbar machine. A graphical representation of this is shown in Figure 4-5.

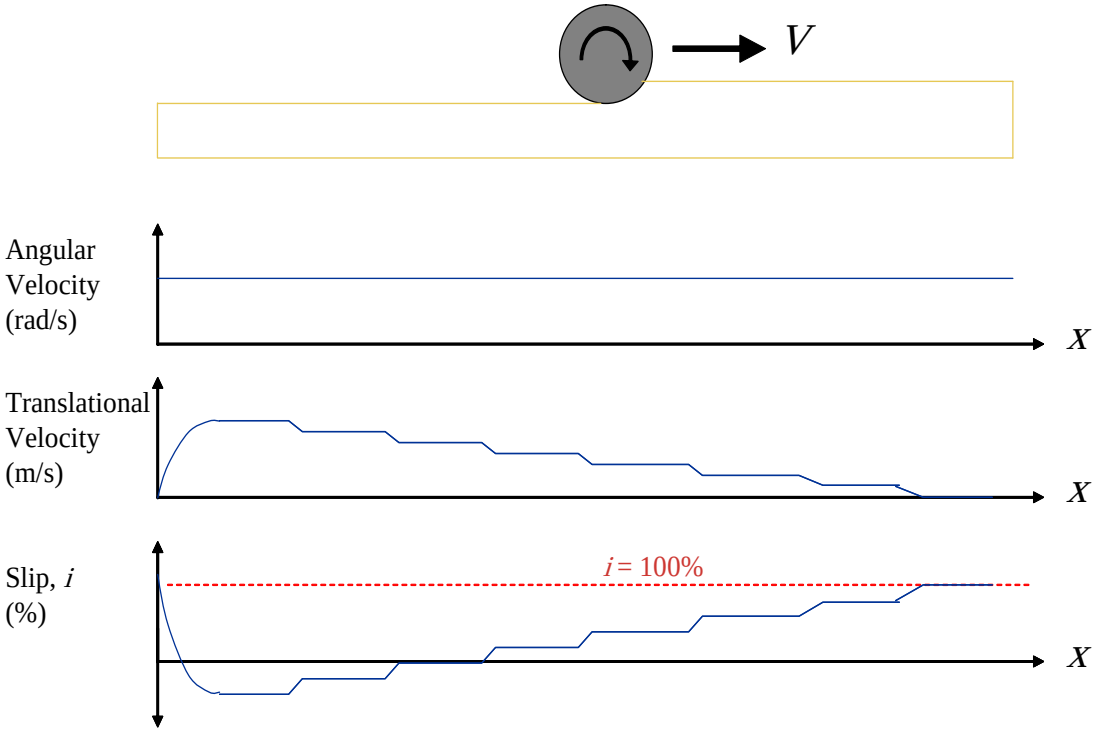

Figure 4-5. Quantitative representation of controlled-pull method of increasing slip in step-wise manner.

The drawbar machine was used to pull with a known amount of force against the vehicle. The range of slips covered by the 4x4 vehicle testing was 0% to 60%.

The normal loads applied to the wheels for these 4x4 tests are shown below:

$$F_z = [70, 80, 114]\ \text{lb}_\text{f} = [311.4, 355.8, 507.1]\ \text{N}$$

The 57-lb_f (253.5-N) load was not used because as it stands currently, the vehicle is too heavy. Steps are being taken to reduce the weight of the vehicle, and it should eventually be able to test at that wheel load. Shown in Figure 4-6 is a picture of the 4x4 vehicle currently being used at NASA GRC for these tests.

Figure 4-6. 4x4 vehicle used at NASA GRC for wheel tests, shown here with 32-in. x 7-in. rigid wheel. Attached circumferentially to each wheel are plastic grousers.

4.2.2 4x4 Vehicle Experimental Procedure

Prior to each test run, the soil was prepared in a method similar to that used on the VT terramechanics rig. Although the specifics of the soil preparation processes utilized at NASA GRC differed from those used at VT, the overall methodology was the same: loosen, rake, level, compact, and confirm that the relative density was correct.

The first step was to set the vehicle weight using corner-weight scales so that the normal load on each wheel could be recorded. Next, the vehicle was placed at one end of test bed and the drawbar machine cable was attached to the hitch as low as possible. This was done to reduce

the weight transfer to the rear wheels as the pulling force was increased. From here the slack in the cable was removed using the drawbar machine.

Next, data recording was started for test duration using a stopwatch, wheel rotation, distance of vehicle travel, drawbar pull using an inline load-cell connecting the vehicle and the drawbar machine cable, and wheel torque. Once all of the data had begun recording, the vehicle was driven at a constant speed. After the vehicle traveled a distance equal to twice its length, the drawbar pull was increased using the drawbar machine. It should be noted that only data from the second vehicle length was used, since this was where an approximately steady-state condition was reached. This step was repeated every two vehicle lengths until the test was completed. Just as for the single-wheel tests, the stopwatch was used to record these points of slip change. A test was said to be complete if either the vehicle had reached the end of the soil bin or if the vehicle had begun to dig significant ruts in the terrain and/or had began to get stuck. Once the test was completed, data recording was stopped, the drawbar pull was released, the vehicle was removed from the bin, and the rut depth was measured along the wheel path.

4.3 Design of Experiment: Summary

Presented in this chapter were two methods of performing drawbar tests using the terramechanics rig at Virginia Tech and the 4x4 vehicle in the soil bin at NASA Glenn Research Center. The tests conditions were presented in the first portion, which included slip ratios to be tested and normal loads to be applied to each wheel.

The second section introduced the testing method for utilization on the VT terramechanics rig using the controlled-slip technique. The first step in this process involved soil preparation steps discussed in Chapter Three. Next, the normal load to be applied to the wheel of interest was set. The third step was to set the wheel speeds to be covered during the test. The final step was to run the tests and record all required data.

In the third segment of this chapter, the test method implemented at NASA-GRC was covered, which employed a controlled-pull testing technique. The first step here was to prepare the soil in a method similar to that used at VT. The second step involved setting the wheel load using at set of corner-weight scales to ensure equal weight on each of the four wheels. Next, the vehicle was placed in the prepared soil, at which point the cable connecting the drawbar machine

to the test vehicle was tightened just enough to remove the slack. Finally, the data recording started and the test run began.

5. Experimental Results and Discussion

Presented in this chapter are the results of the single-wheel tests performed at the Virginia Tech Advanced Vehicle Dynamics Lab. The first part of this chapter provides results and discussions for each wheel that was tested. The second part benchmarks the results presented earlier, comparing the performance of the four wheels. The experimental data, including the normal load, used to create the plots in these sections can be found in Appendix A. The third part of this chapter presents the results of the pressure pad tests performed with a normal load of 57-lb_f (253.5-N) using the TekScan 3150 Pressure Pad. More pressure pad tests results are presented in Appendix A, as well.

5.1 Experimental Results and Discussion: Individual Wheel Performance

5.1.1 32-in. x 7-in. Rigid Wheel

This section covers the testing results of the 32-in. x 7in. rigid wheel. Because this wheel was considered the baseline wheel, it was tested first. The measured drawbar pull vs. slip ratio is shown in Figure 5-1 below.

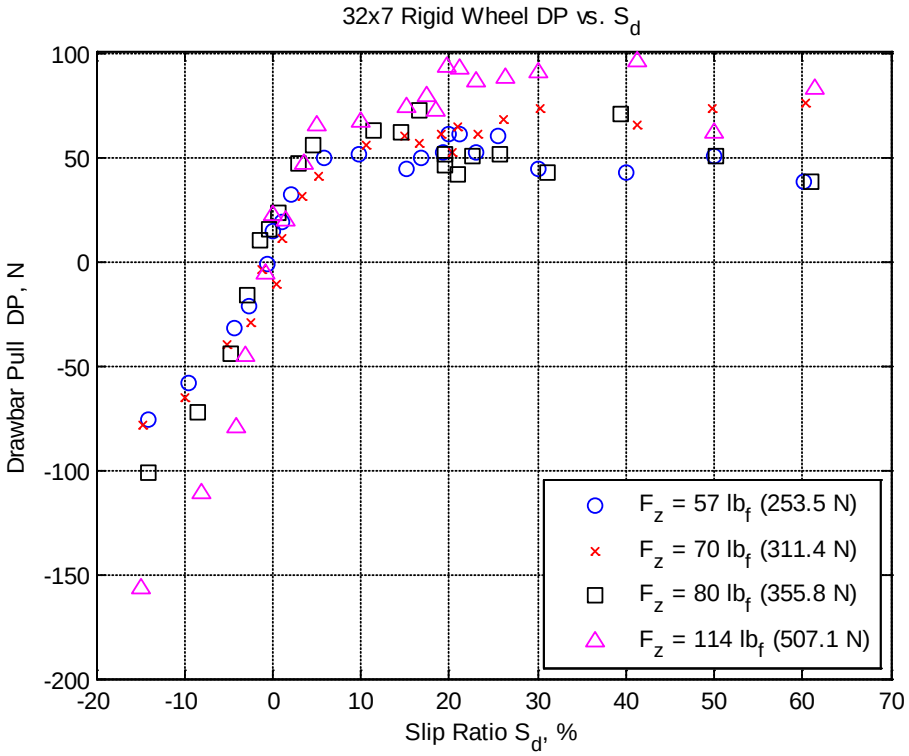

Figure 5-1. Drawbar pull vs. slip ratio for the 32-in. x 7-in. rigid wheel.

Analyzing this plot, it is clear that for all normal loads the pull in the negative slip (braking) region of the plot is significantly greater than that in the driving region. It can also be seen that around +20% slip, the slope levels off and does not see any more significant increases. These two observations are consistent with some of the observations made in [3]. After 20% slip the drawbar pull still increases; however, because of the large amount of wheel spin, the wheel would be wasting substantial energy and the vehicle's translational speed would become so low that it would become practically stuck, a very undesirable scenario. With this in mind, it should be pointed out that, in this plot, the tendency of the curves to level out signifies that the wheel has reached its traction limits these given normal loads.

Another observation drawn from this data is that the pull-values align in an expected, orderly manner for the negative slip range. On the other hand, around +10% slip a scattering of the results begins. This is interesting because the values should remain in order if the normal loads were constant. After studying the normal load traces of each test, it became obvious that, although the experiments were designed to maintain a constant normal load, the normal load varied significantly enough during testing. This was due to undulations in the terrain level created during the compaction step of the soil preparation procedure, combined with an insufficient method of setting the normal load, and possible friction in the vertical linear bearings of the test rig carriage. This situation should be resolved before further testing is done. This issue will be further addressed, with suggested solutions in Chapter 7. In light of this, the data for the slip ratios from -15% to +10% are reliable; however, beyond that the data becomes questionable.

Shown in Figure 5-2 is a 3-D plot of drawbar pull vs. normal load vs. slip ratio for all of the baseline wheel's tests.

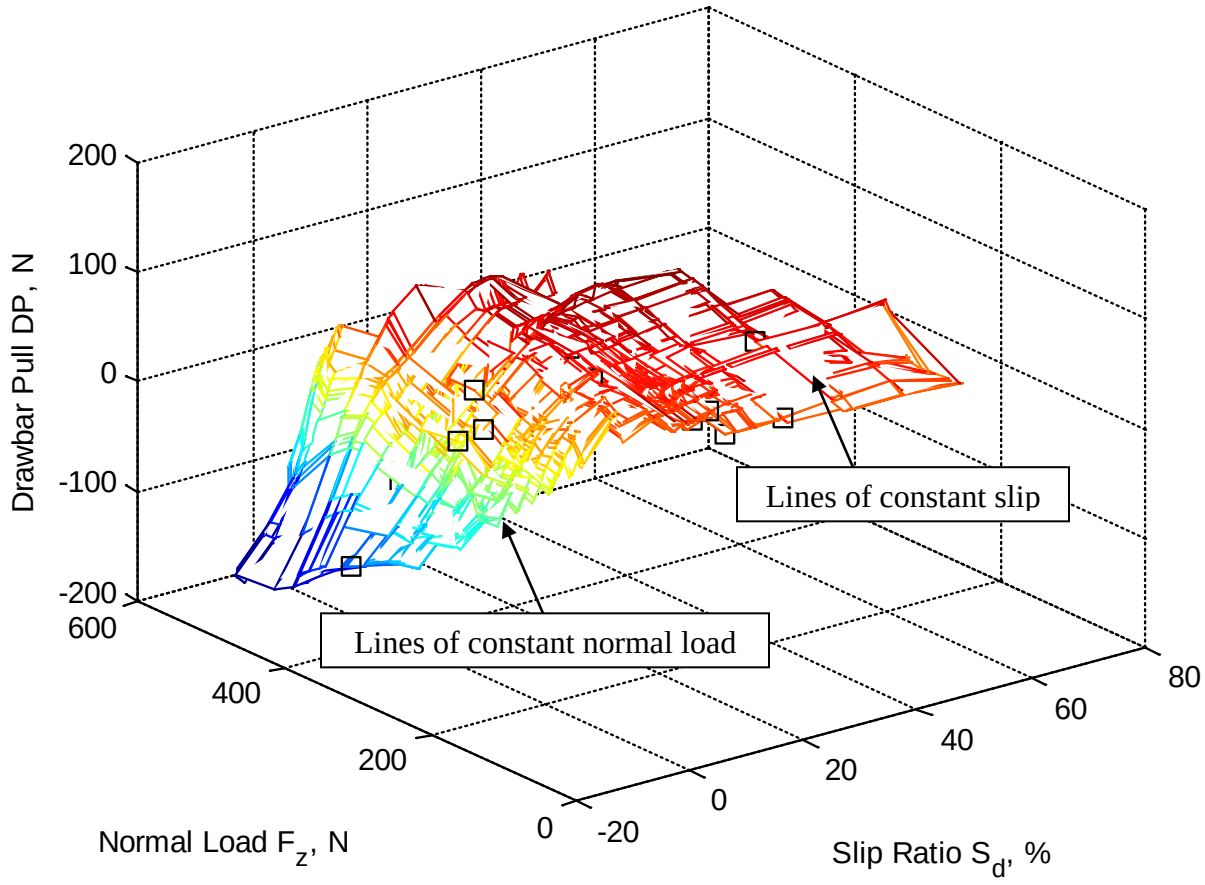

Figure 5-2. *DP* vs. F_z vs. S_d surface created with results of 32-in. x 7-in. baseline wheel tests.

The 3-D surface was created to understand how normal load and slip ratio affected the drawbar pull created. The black squares represent the data from the 355.8-N normal load test. In the figure, the color varies blue to red with increasing *DP*-values. The lines on the surface that run parallel to the slip ratio axis represent the lines of constant wheel slip. The lines running parallel to the normal load axis are the lines of constant normal load. The data from each wheel test was interpolated to create the surface, with varying levels of drawbar pull on the vertical axis. When the pull and normal load are projected onto the slip-ratio axis, the lines can be seen with their respective values, such as in Figure 5-3.

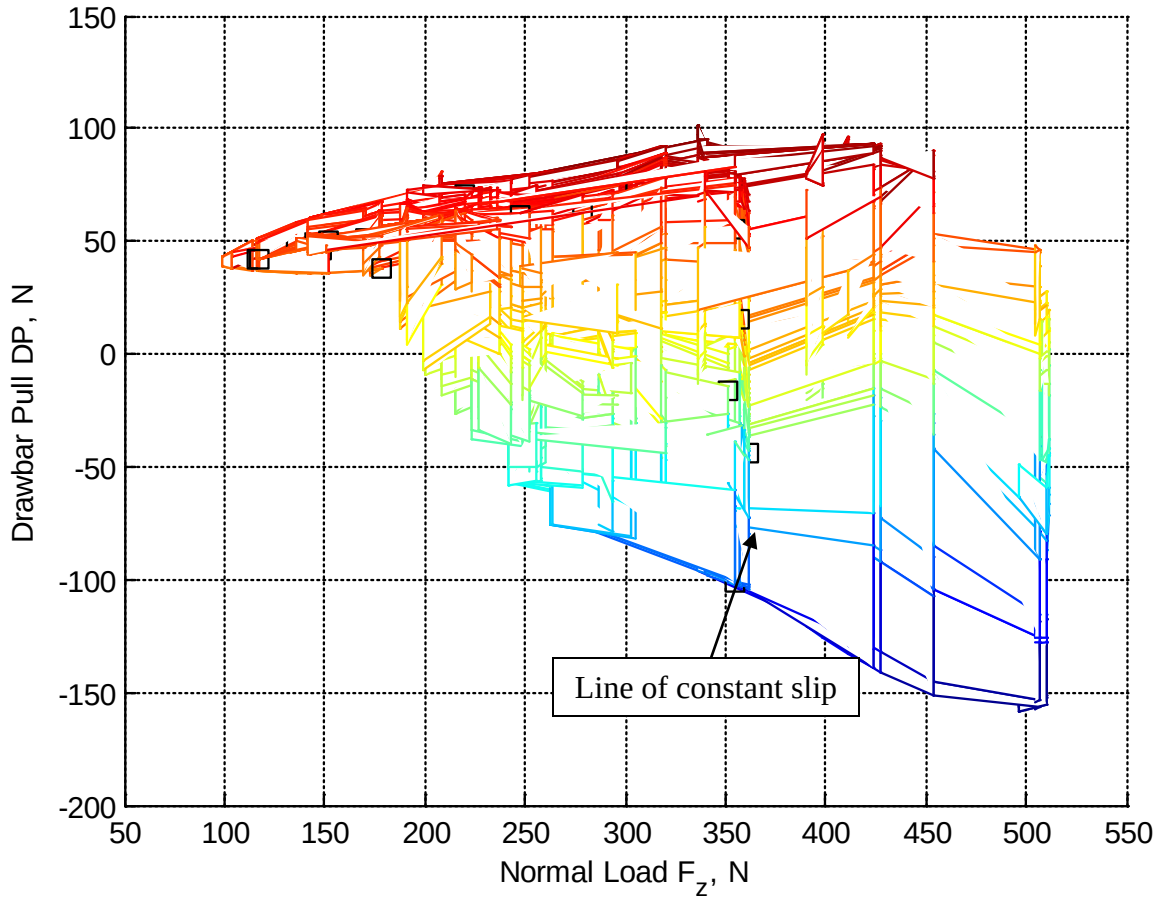

Figure 5-3. Projected view of *DP* vs. F_z for baseline wheel. The vertical lines represent lines of constant normal load.

The three-dimensional surfaces were created with the purpose of selecting values of normal load and slip ratio, and using these values to interpolate what the resulting drawbar pull would be. Utilizing this "drawbar pull map" can serve as a useful predictor of the performance of each wheel at any desired value of slip and normal load, and is very similar to mapping the performance characteristics of an internal combustion engine as a function of fuel and air inputs.

The measured driving torque required for motion in this test is shown in Figure 5-4 below.

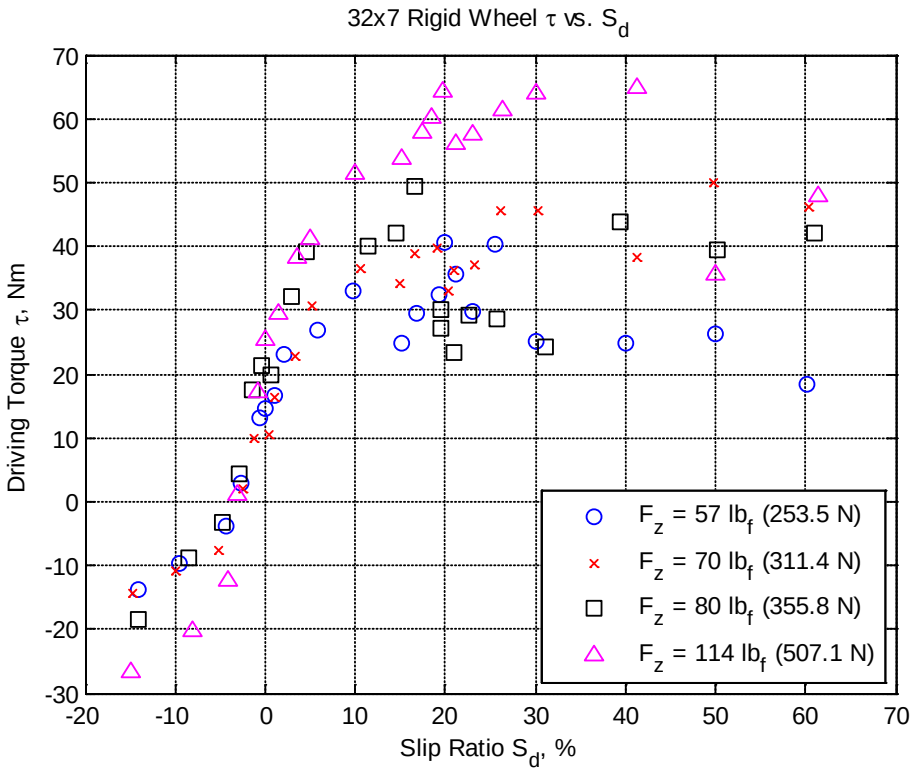

Figure 5-4. Driving torque vs. slip ratio for 32-in. x 7-in. wheel.

The torque tends to reach a maximum value between +15% and +20% slip. Because of the variation in normal load, the scatter seen in Figure 5-1 is again seen in Figure 5-4. A three-dimensional surface of the torque vs. normal load vs. slip ratio is shown in Figure 5-5, with the 355.8-N normal load case highlighted with black squares.

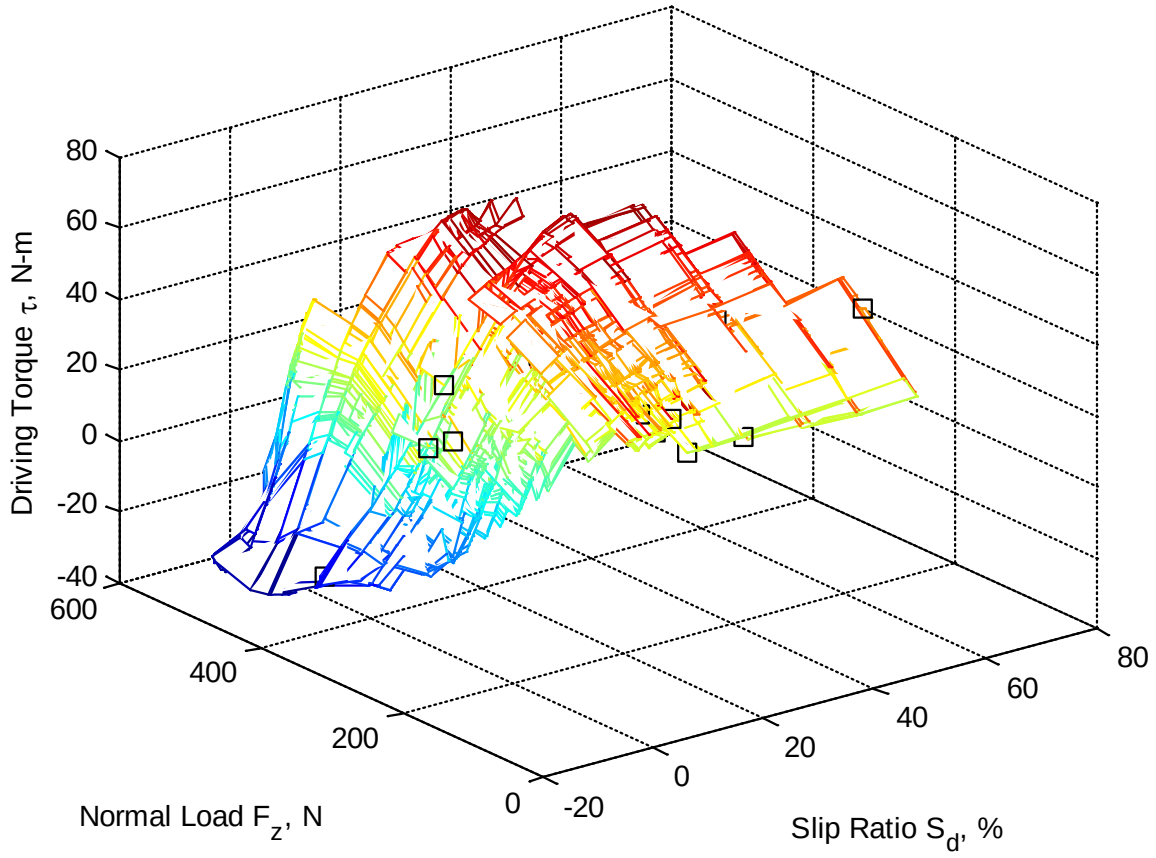

Figure 5-5. τ vs. F_z vs. S_d surface created with results of 32-in. x 7-in. baseline wheel tests.

Similar to that in Figure 5-3, this surface could be considered a driving torque map.

5.1.2 32-in. x 11-in. Rigid Wheel

Covered in this section are the results of testing the rigid 32-in.-x-11-in. wheel. The results for the drawbar pull versus slip ratio of this wheel are shown in Figure 5-6.

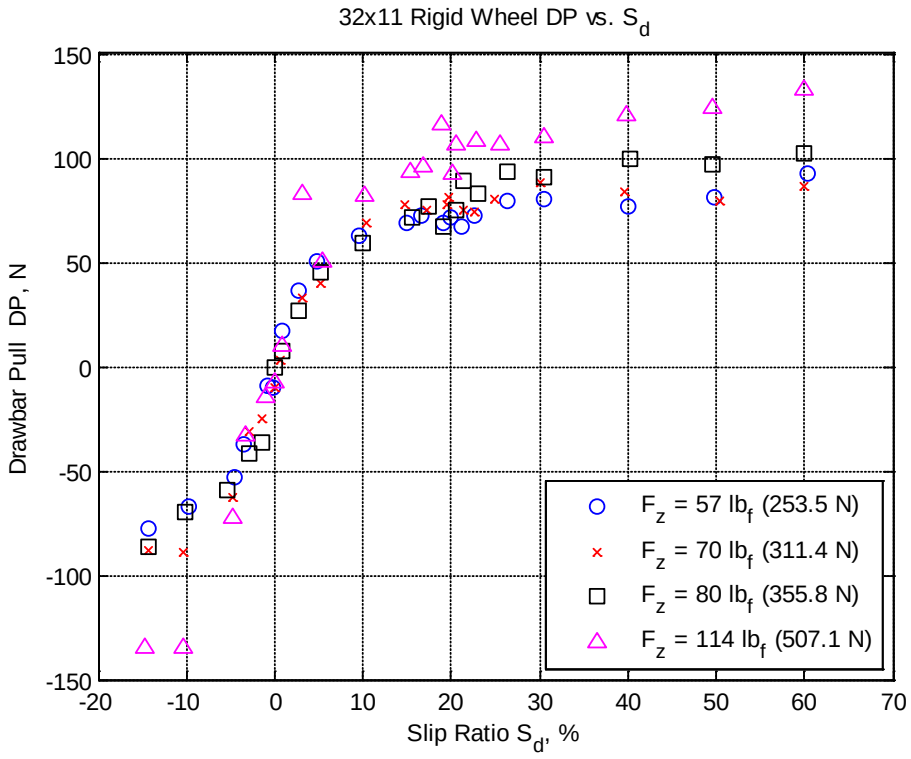

Figure 5-6. Drawbar pull vs. slip ratio experimental results for the 32-in. x 11-in. rigid wheel.

There seems to be a bit of symmetry in the shape of the data for the lowest three normal loads. For instance, for the 253.5-N load at -15% slip the pull is very near -75 N, and for the same load at +15% slip the drawbar pull is close to +75 N. At higher values of slip, there again exists the same scattering of data as seen in Figure 5-1. But on the other hand, the scatter is not as large. The traction limit of this wheel at the given loads is very clearly defined in Figure 5-6. A drawbar pull map for this wheel has been provided in Figure 5-7.

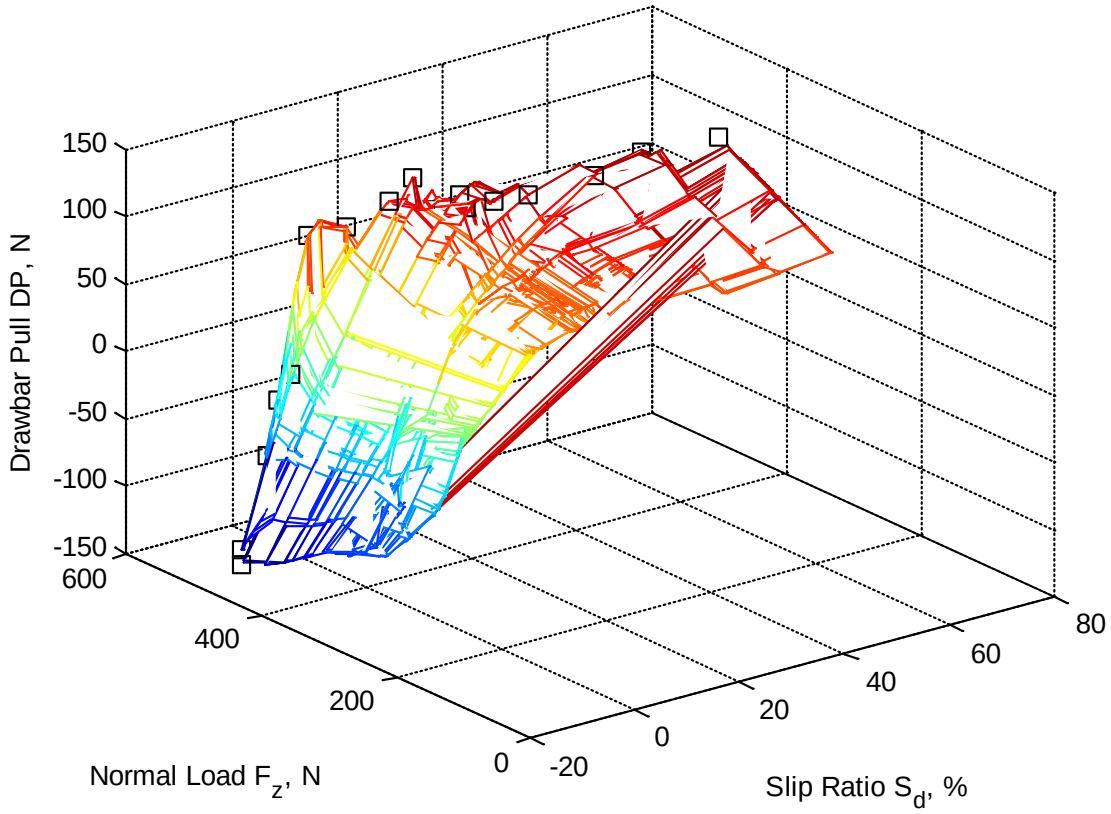

Figure 5-7. *DP* vs. F_z vs. S_d surface created from 32-in. x 11-in. wheel test results.

In Figure 5-7 the black squares represent the data taken during the tests performed with the 507.1-N normal load. The constant-slip and constant-load lines were created in the same fashion as the 32-in. x 7-in. *DP* map.

The torque vs. slip ratio results for this wheel can be seen in Figure 5-8.

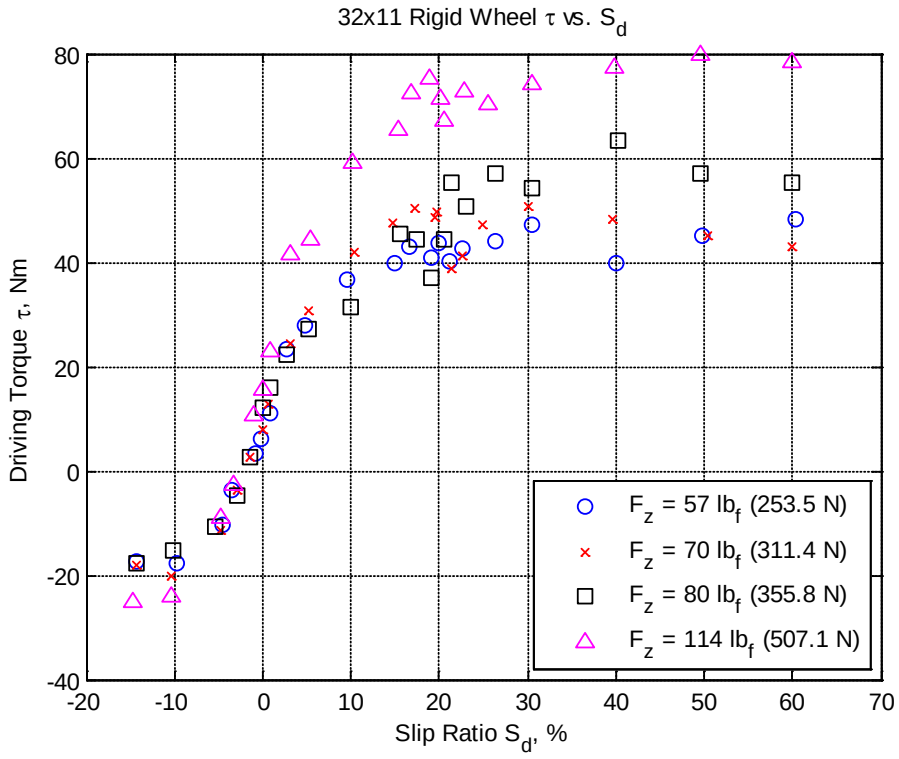

Figure 5-8. Driving torque vs. slip ratio plot for 32-in. x 11-in. rigid wheel.

In this plot it is firstly noticed that from -15% to +5% slip, the torque values of the lowest three loads seem to be independent of normal load, as they are nearly coincident through that range of slips. Again, a driving torque map was created to gain a better understanding of the wheel's performance, as shown in Figure 5-9.

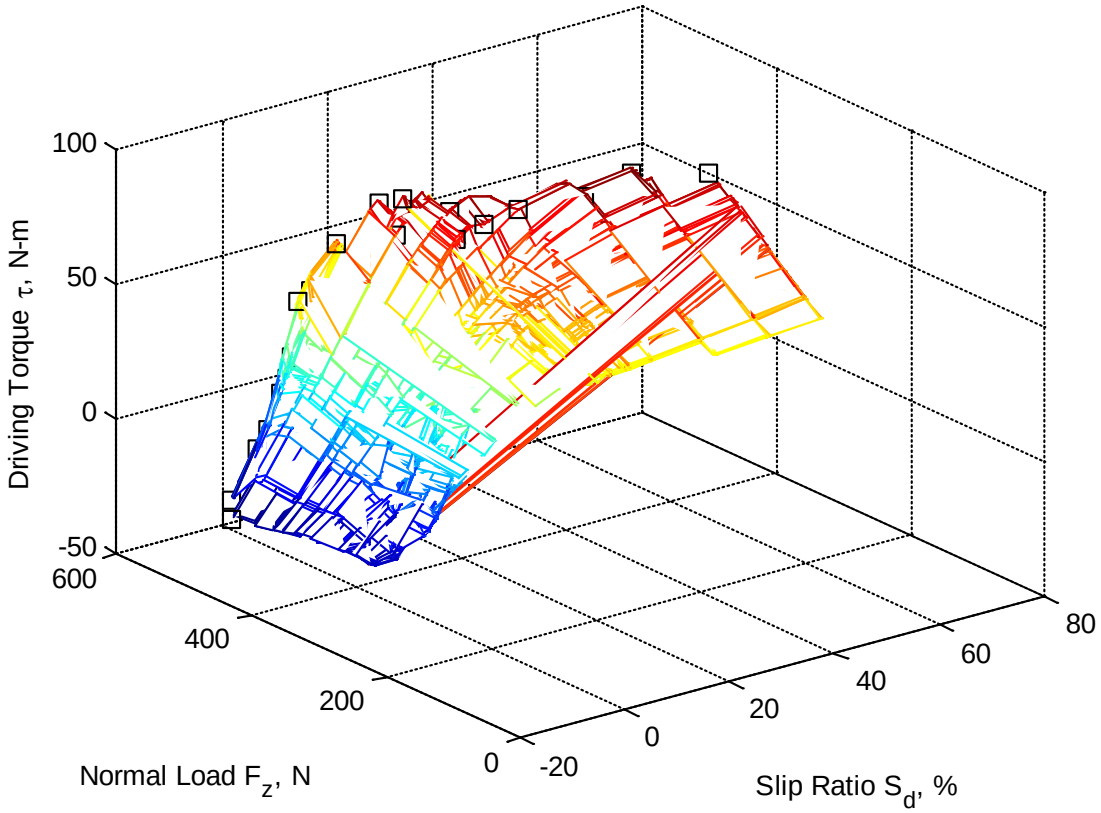

Figure 5-9. 3-D plot of τ vs. F_z vs. S_d for the 32-in. x 11-in. rigid wheel.

The black squares represent the 507.1-N normal load experimental results for this wheel.

5.1.3 20-in. x 7-in. Rigid Wheel

In this section the experimental results of the 20-in. x 7-in. rigid wheel will be covered. Shown in Figure 5-10 is the plot of drawbar pull vs. slip ratio for this wheel.

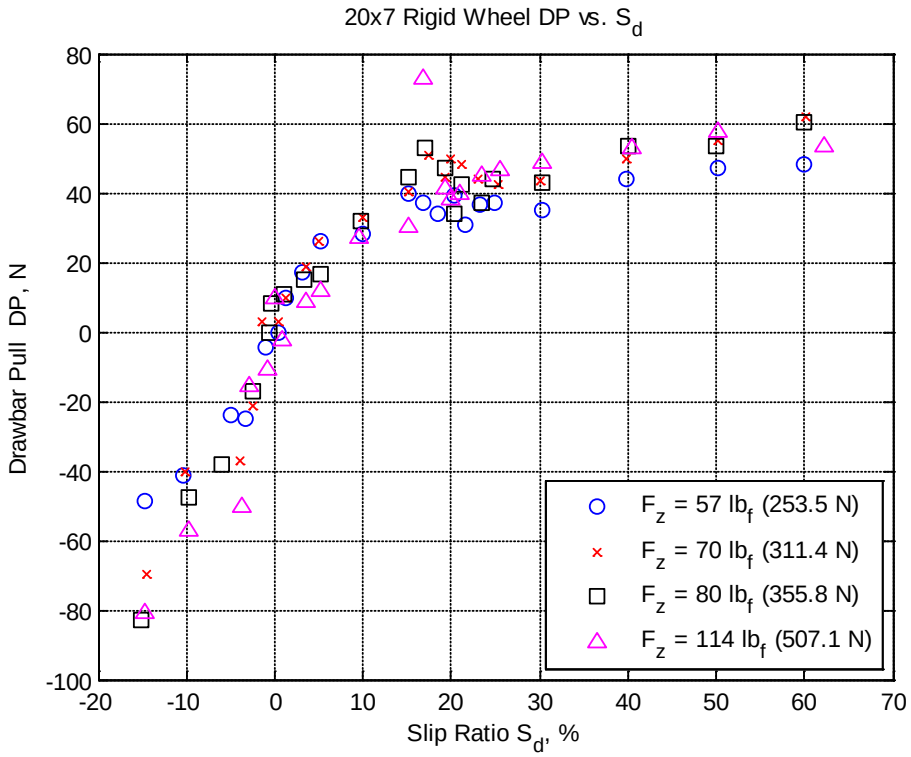

Figure 5-10. Drawbar pull vs. slip ratio curves for each load at which the 20-in. x 7-in. rigid wheel was tested.

Figure 5-10 shows clearly defined traction limits, beginning at about +15% slip. While the trends shown in this plot are clear, some of the data points do not seem to make much sense. For example, at +15% slip the drawbar pull created as a result of the 507-1-N test is less than that created by the other three tests. Because drawbar pull is known to be directly proportional to normal load, one can conclude that the normal load at this point was significantly less than the three greater values. The normal load trace can be seen in the *DP* map in Figure 5-11.

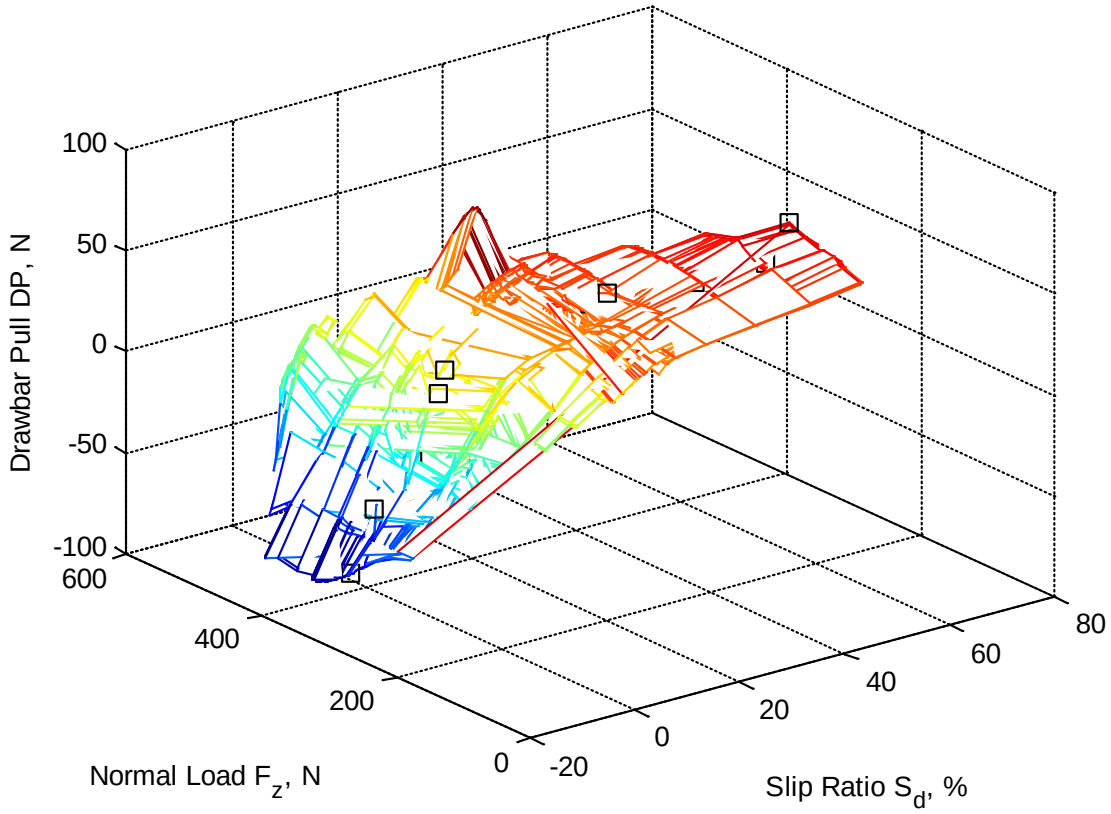

Figure 5-11. *DP* map for the 20-in. x 7-in. rigid wheel.

In Figure 5-11 the black squares represent the experimental results for the 311.4-N normal load.

The torque-versus-slip-ratio results and torque map are depicted in Figures 5-12 and 5-13, respectively.

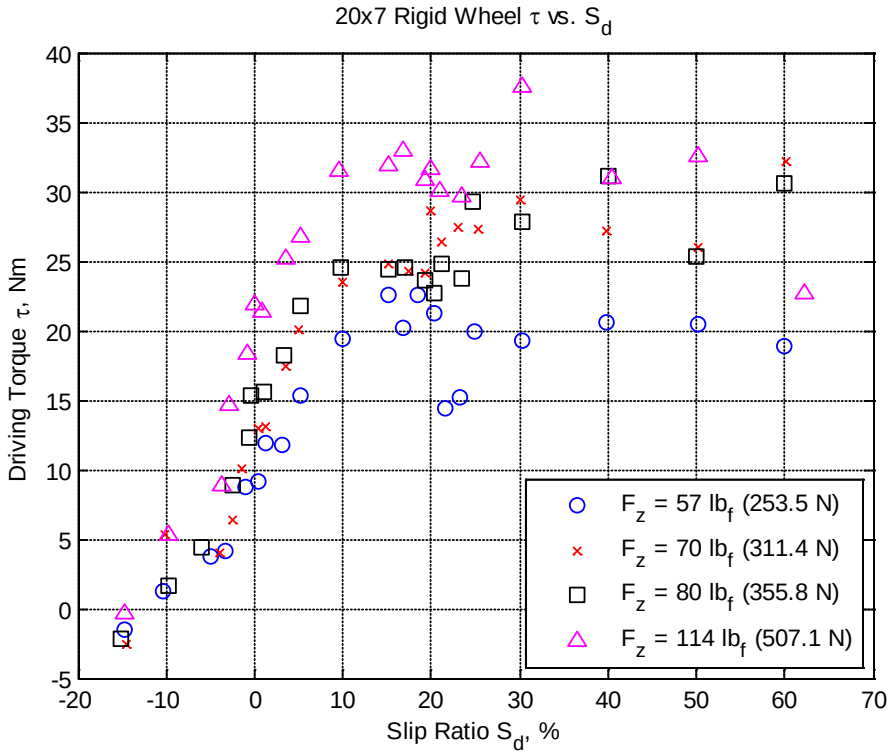

Figure 5-12. Driving torque vs. slip ratio for the 20-in. x 7-in. rigid wheel.

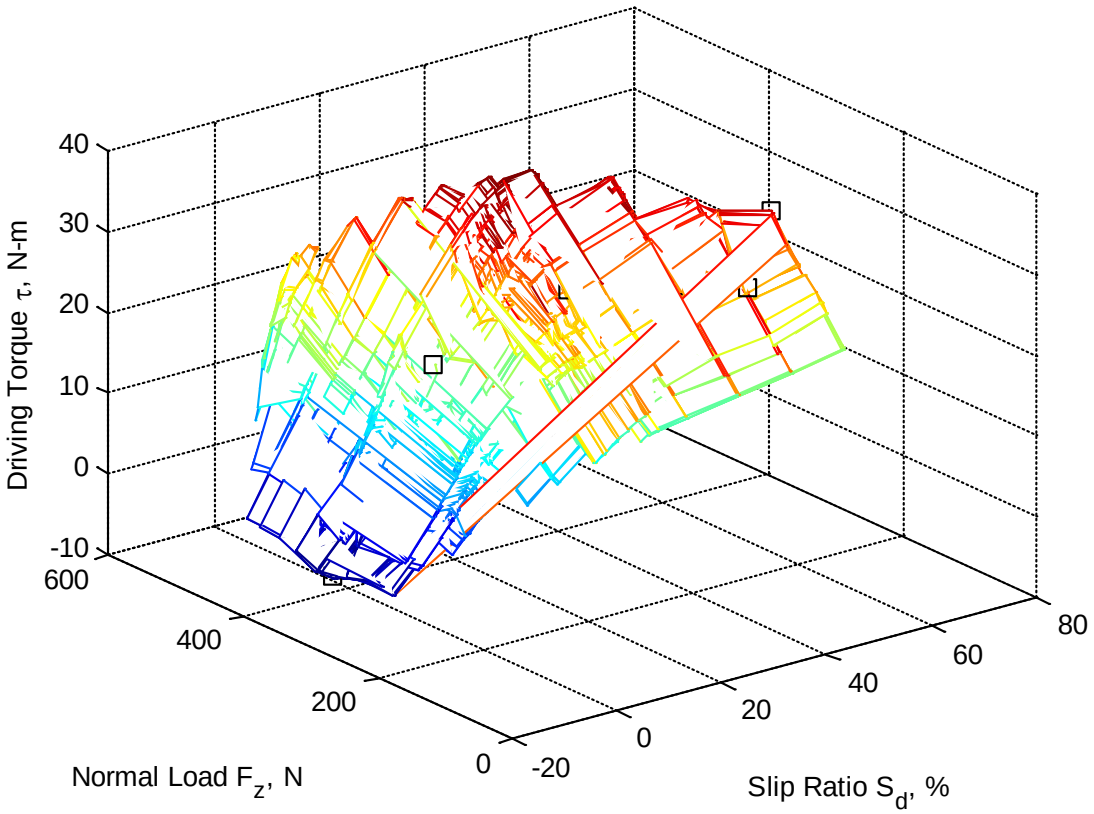

Figure 5-13. τ vs. F_z vs. S_d three-dimensional plot for the 20-in. x 7-in. rigid wheel.

The data displayed in Figure 5-12 is somewhat interesting. This is because the values of torque are greater than zero for every slip ratio except -15%. A reason for this may be because the wheel's radius is significantly smaller than the other wheels being presented in this study. A second observation is that the trend of the torque curves to increase at a greater rate and reach greater maximum values as the normal load increases. It also seems that the slope of each curve changes at a -5% slip, no matter what the wheel load is. The magnitude of the normal load does, however, seem to determine how greatly the slope changes. The scatter of data points shown in this plot is most likely due to a sudden drop in normal load after +10% slip. In Figure 5-13 the black squares provide markers for the 311.4-N normal load results.

5.1.4 32-in. x 7-in. Spiral Wheel

Covered in this section are the 32-in. x 7-in. spiral wheel results. Recall that this wheel was only tested at one load condition (253.5 N). Shown in Figures 5-14 and 5-15 are the experimental data from the drawbar pull and driving torque vs. slip, respectively.

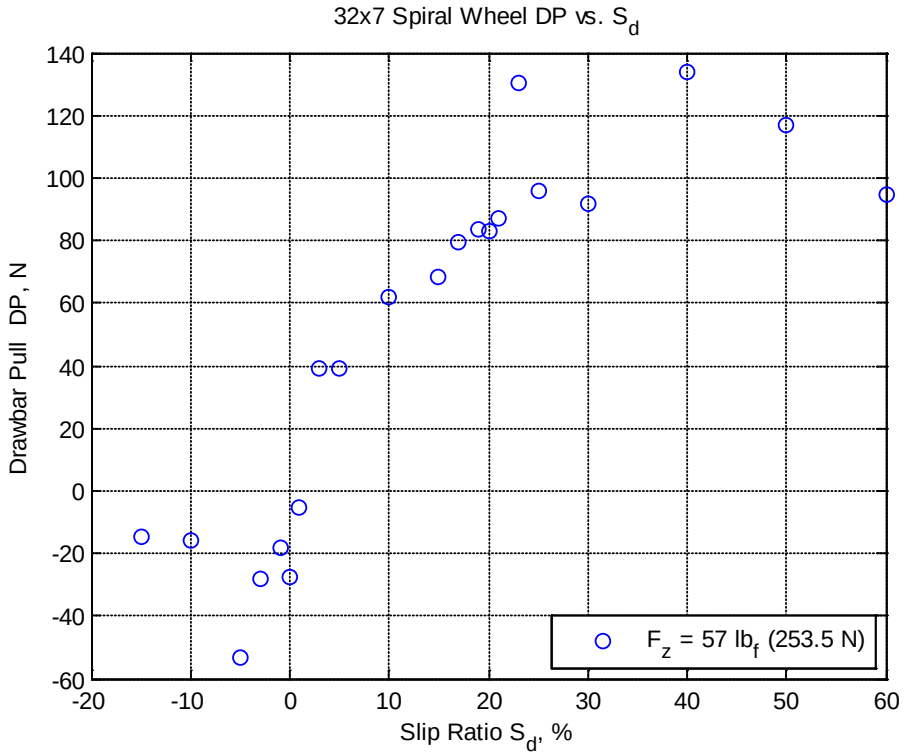

Figure 5-14. Plot of drawbar pull vs. slip ratio for the 32-in. x 7-in. spiral wheel.

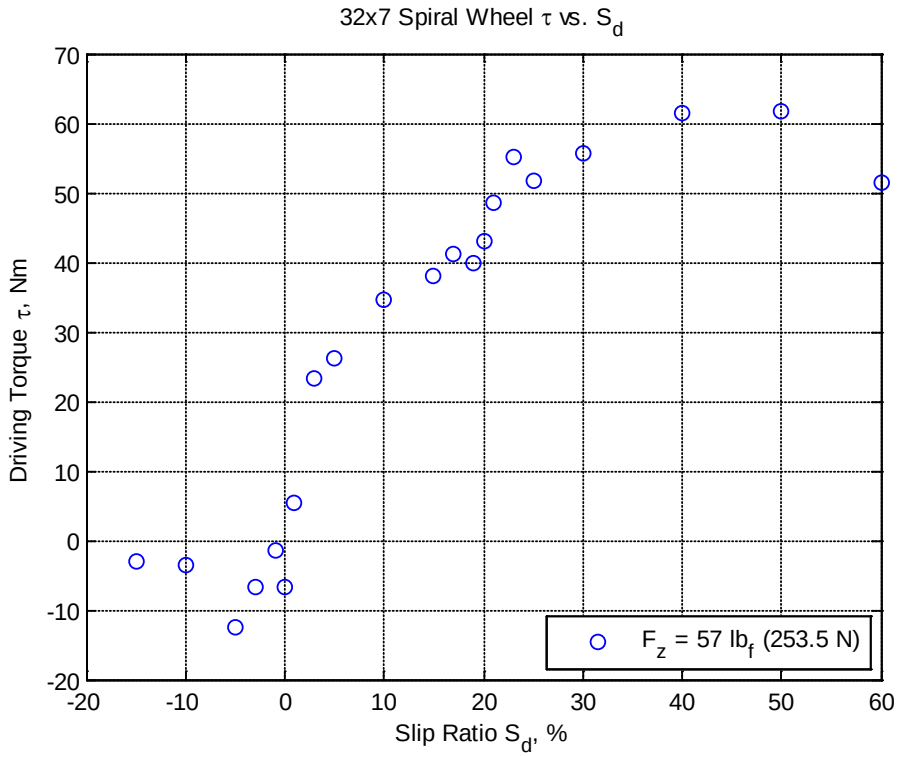

Figure 5-15. Plot of driving torque vs. slip ratio for the 32-in. x 7-in. spiral wheel.

Unlike the tests involving the first three wheels, during these flexible-wheel tests we were able to maintain a constant normal load for more than half of the experiments. The ability to do so was discovered near the completion of the entire testing ensemble, as it was found that setting the run-up lane (see Chapter 3) to a lower level than the test lane counteracted the normal-load drops seen at higher slip ratios. As previously mentioned, it was found that the variations in terrain height affect the normal load, and in an attempt to lessen these effects we started the wheel at the aforementioned lower soil height. The wheel's unique design created dynamics within the wheel system that were previously unseen, however. This wheel's design was similar to that of a torsion spring, which caused "wind-up" and "unloading" similar to what may be seen in an undamped torsion-type. This resulted in somewhat sporadic raw data; however, there were a sufficient number of steady-state data regions to study and present these results. For uniformity in presenting the results of this study, drawbar pull and torque maps were created for this wheel, as well, and are shown in Figures 5-16 and 5-17; experimental data are represented using the blue circles.

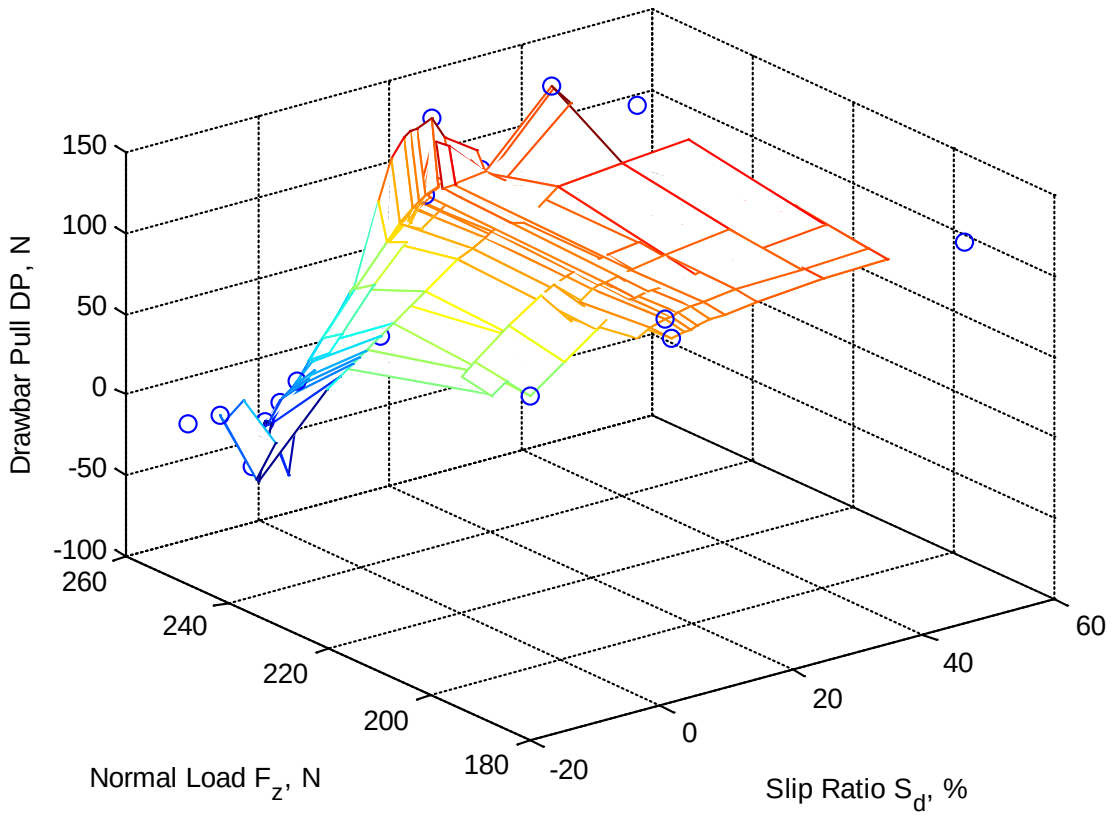

Figure 5-16. 3-D surface created using *DP* results of the 32-in. x 7-in. spiral wheel tests.

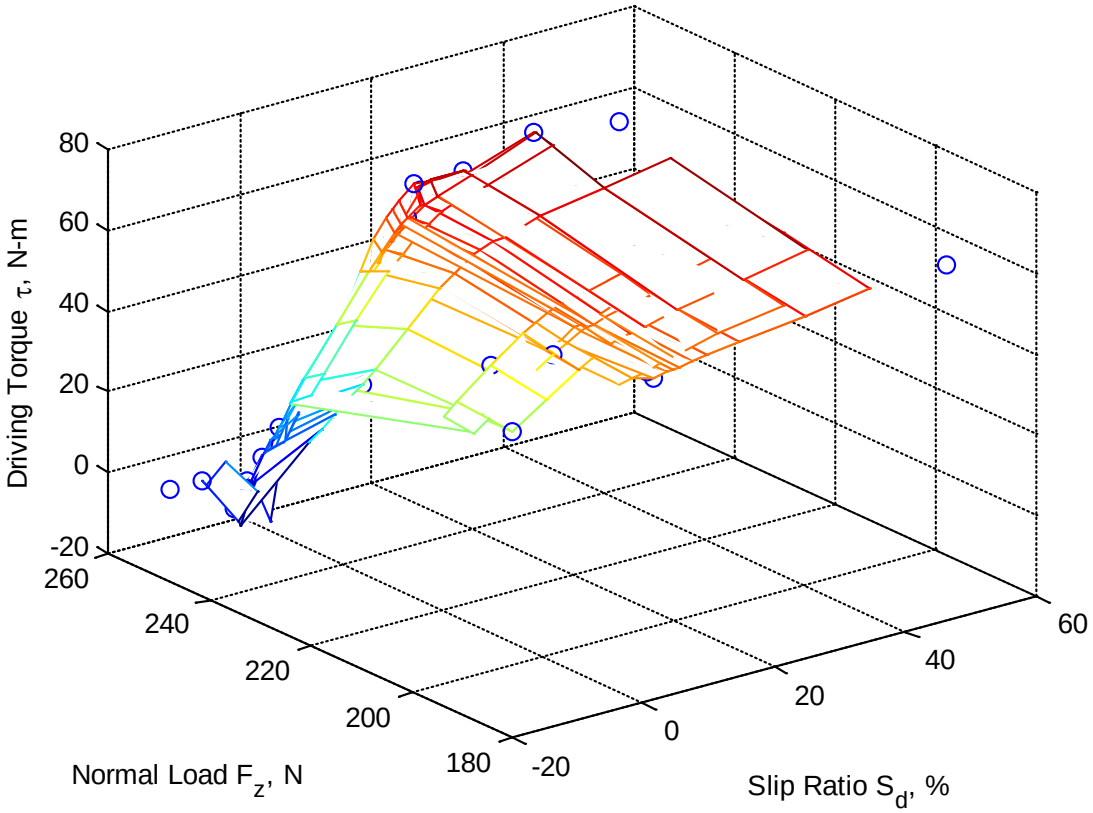

Figure 5-17. Torque map for the 32-in. x 7-in. spiral wheel.

5.2: Experimental Results and Discussion: Wheel Comparison

The purpose of this section is to provide a comparative look at the tractive performance of the four different wheels at each normal load. From these plots one can understand how the parameters of a wheel that influence the drawbar pull and driving torque of any particular wheel.

Shown in Figures 5-18 and 5-19 are the curves for the drawbar pull and torque versus slip ratio, respectively, with a normal load of 57 lb_f (253.5 N).

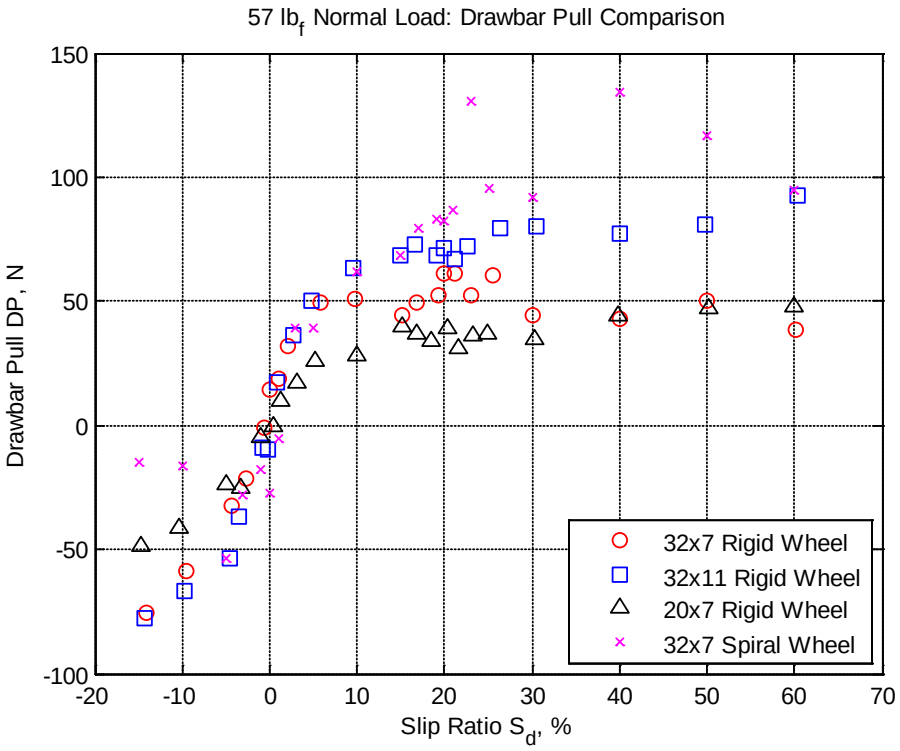

Figure 5-18. Plots of drawbar pull vs. slip ratio for all four wheels under the 253.5-N normal load.

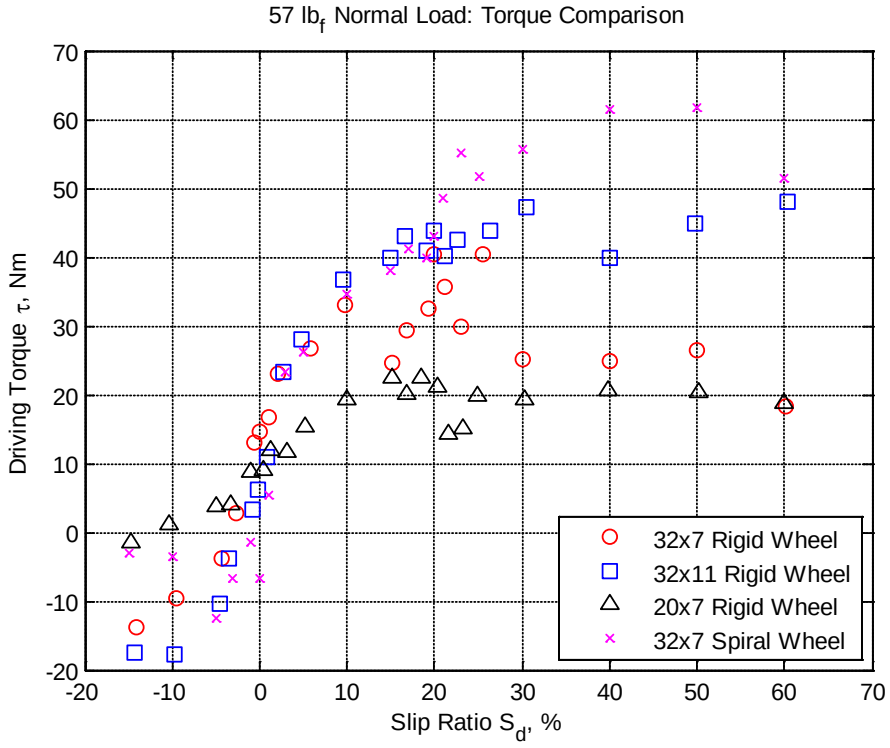

Figure 5-19. Wheel plots of driving torque vs. slip ratio for all four wheels at the 253.5-N normal load.

In Figure 5-18 the spiral wheel produced the greatest maximum drawbar pull. The wheel with the second-largest maximum pull value was the 11-in.-wide rigid wheel. Next was the baseline 32-in. x 7-in. rigid wheel. As was expected, the 20-in. wheel created the lowest maximum drawbar pull. The wheel that created the highest maximum driving torque as shown in Figure 5-19 was, again, the spiral wheel. Next was 32-in. x 11-in. rigid wheel followed, in order, by the rigid 32-in. x 7-in. and 20-in. x 7-in. wheels. Using relationships discussed in [1] and [17] that wheels with larger contact patch areas will require greater torque and create drawbar pull than wheels with smaller contact areas. The spiral wheel was designed to simulate a wheel of greater diameter than the baseline wheel, and the 11-in.-wide wheel was designed with the contact width in mind, and therefore, these two wheels should have performed the best. The 20-in. wheel had the lowest performance due to its shortened diameter. The smaller diameter created a smaller contact area and thus, lower pull values. The torque required by the 20-in. x 7-in. wheel was significantly lower than that of the other three wheels because torque is directly dependent on the wheel radius, as shown in the work of Wong and Reece ([1], [17]).

Plots comparing the drawbar pull and torque created by three rigid wheels when subjected to a 70-lb_f (311.4-N) normal load are shown in Figures 5-20 and 5-21, respectively.

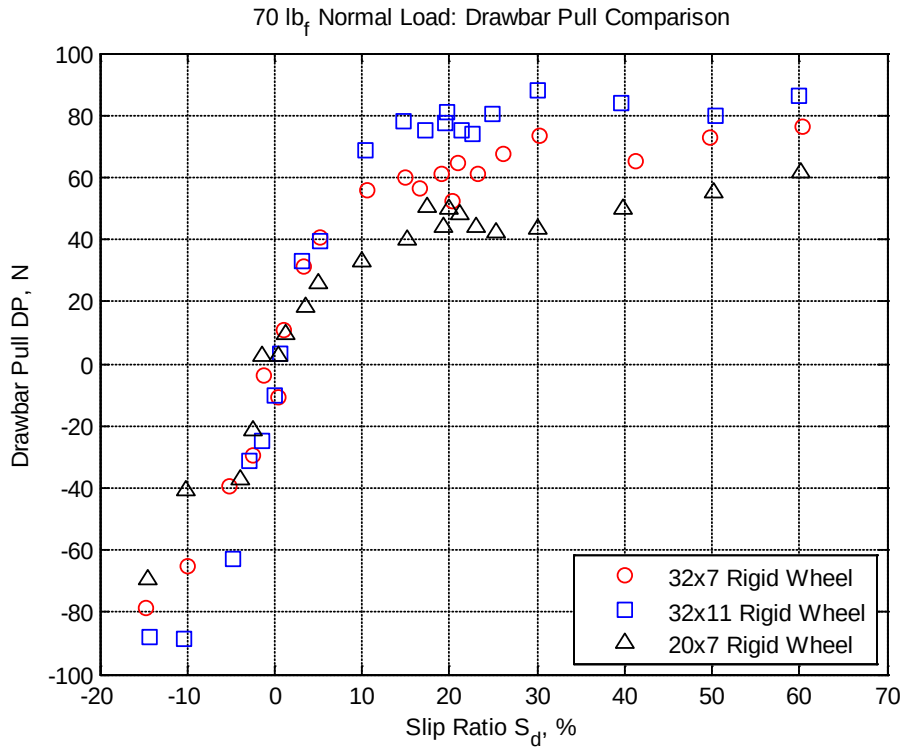

Figure 5-20. Plots of drawbar pull vs. slip ratio for the three rigid wheels under the 311.4-N normal load.

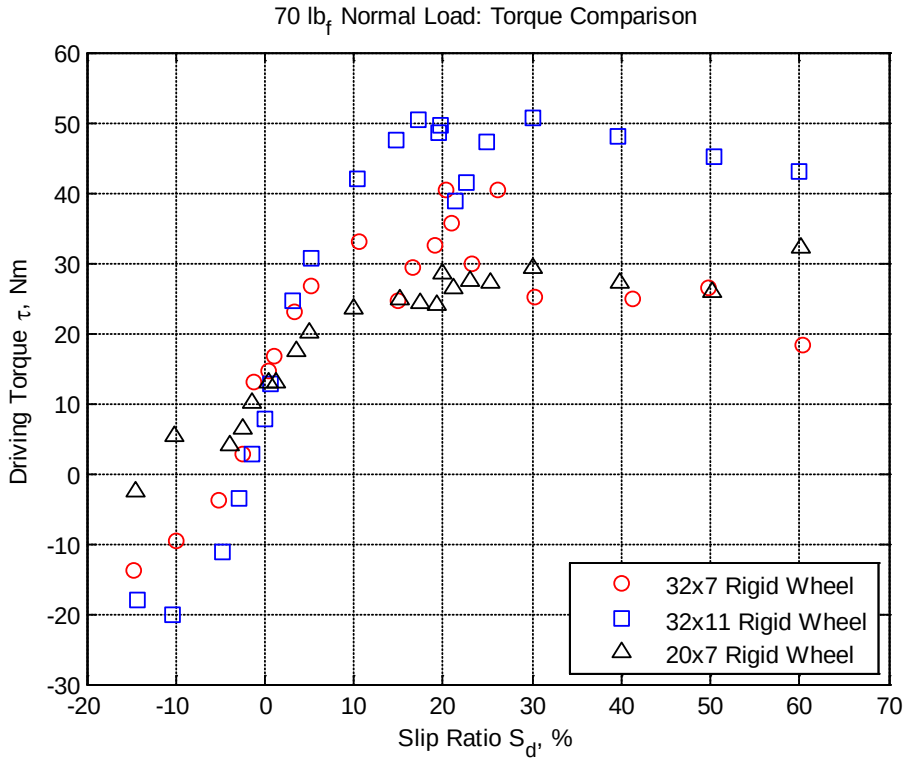

Figure 5-21. Comparison plots of torque vs. slip ratio for the three rigid wheels, considering a 311.4-N normal load.

As was the case with a 253.5-N normal load applied, the overall *DP*- and τ-values were the greatest for the 32-in. x 11-in. wheel, as can be seen in Figure 5-20 and 5-21. The second-greatest overall drawbar pull and torque were created by the baseline wheel and, as before, the 20-in.-diameter wheel produced the lowest overall pull and torque values. These results reaffirm the conclusion that the area of the contact patch directly affects the tractive performance of a wheel.

The results shown in Figures 5-22 through 5-25 further confirm the direct correlation between contact patch area and wheel performance. Figures 5-22 and 5-23 are the results of the tests with an applied normal load of 80 lb_f (355.8 N). Figure 5-24 and 5-25 provide the drawbar pull and torque versus slip ratio curves for the 114-lb_f (507.1-N) normal-load experiments.

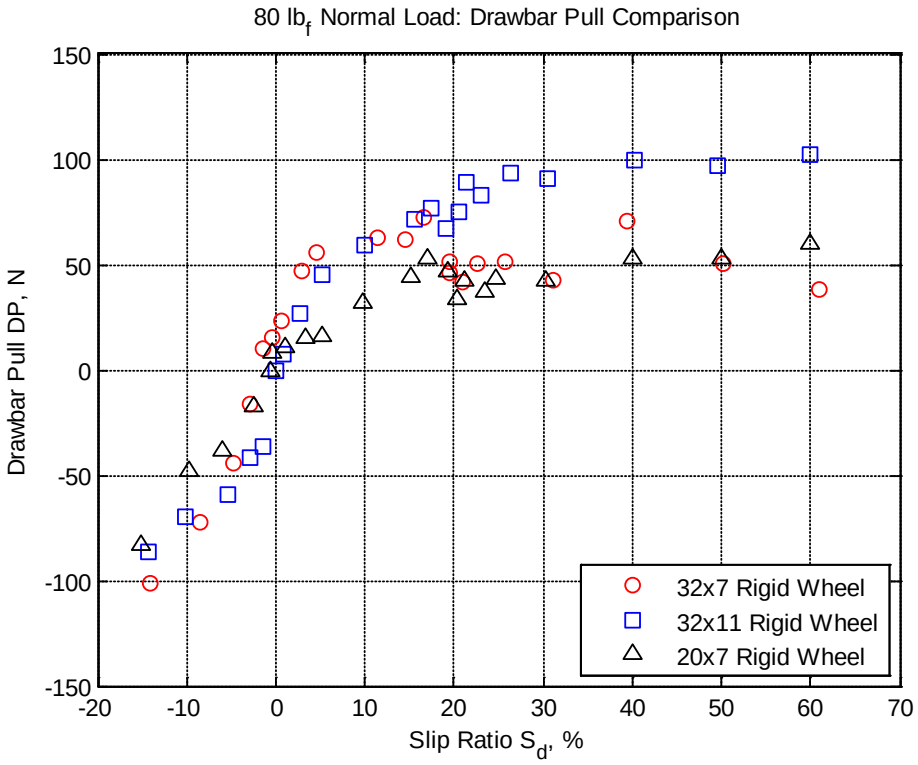

Figure 5-22. Plot comparing drawbar pull vs. wheel slip for the three rigid wheels with an applied normal load of 355.8 N.

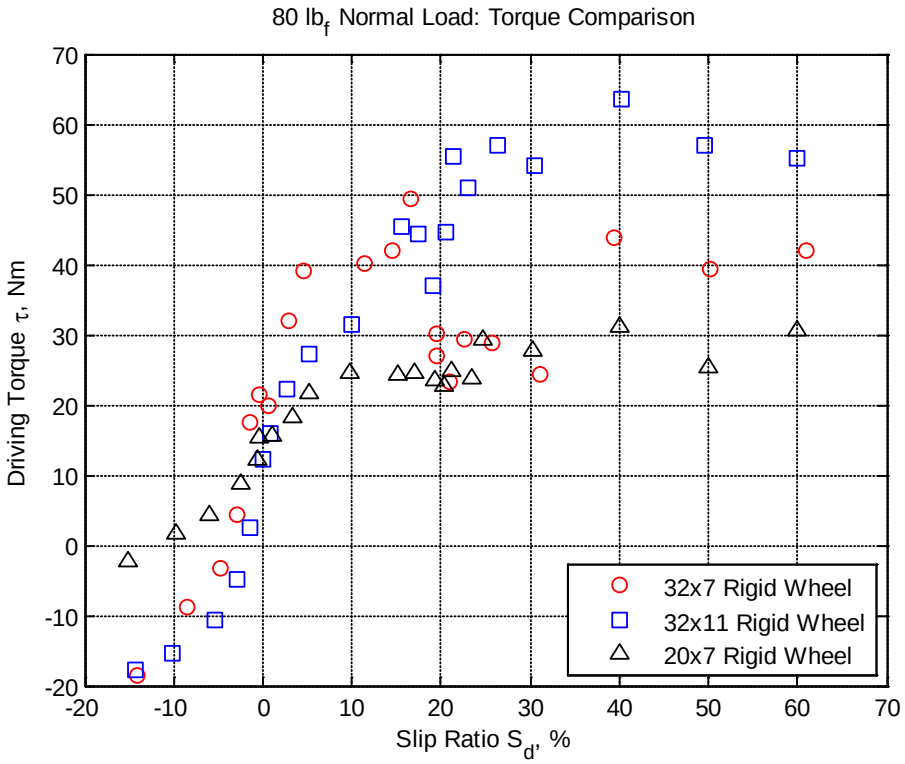

Figure 5-23. Plots of driving torque vs. slip ratio for the three rigid wheels with a 80-lb_f (355.8-N) applied.

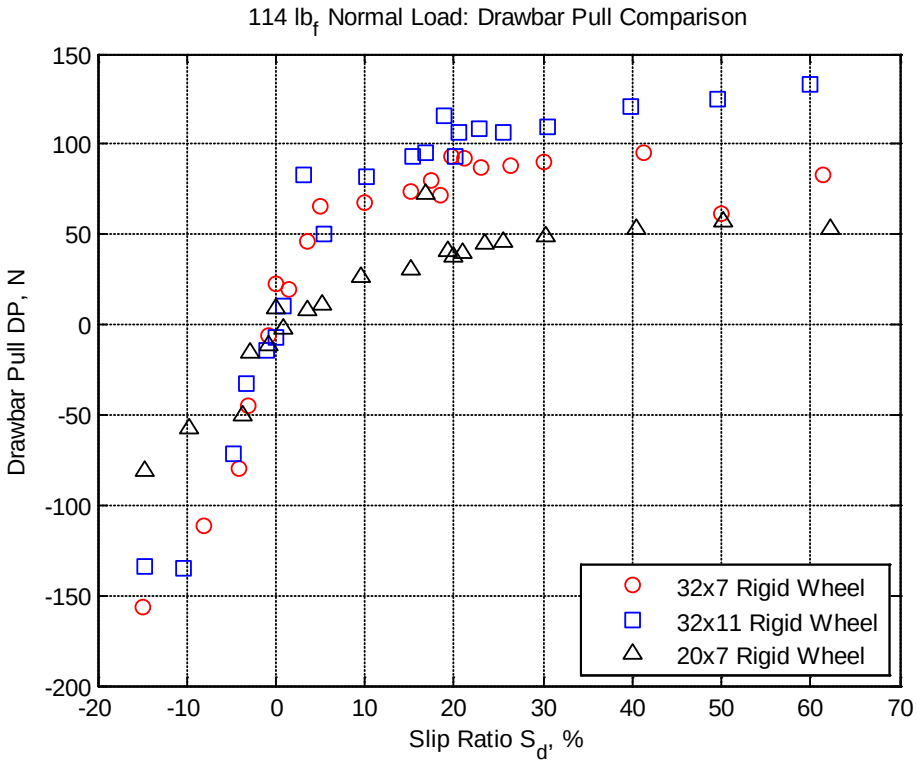

Figure 5-24. Drawbar pull vs. slip ratio for the three rigid wheels with an applied 114-lb_f (507.1-N) normal load.

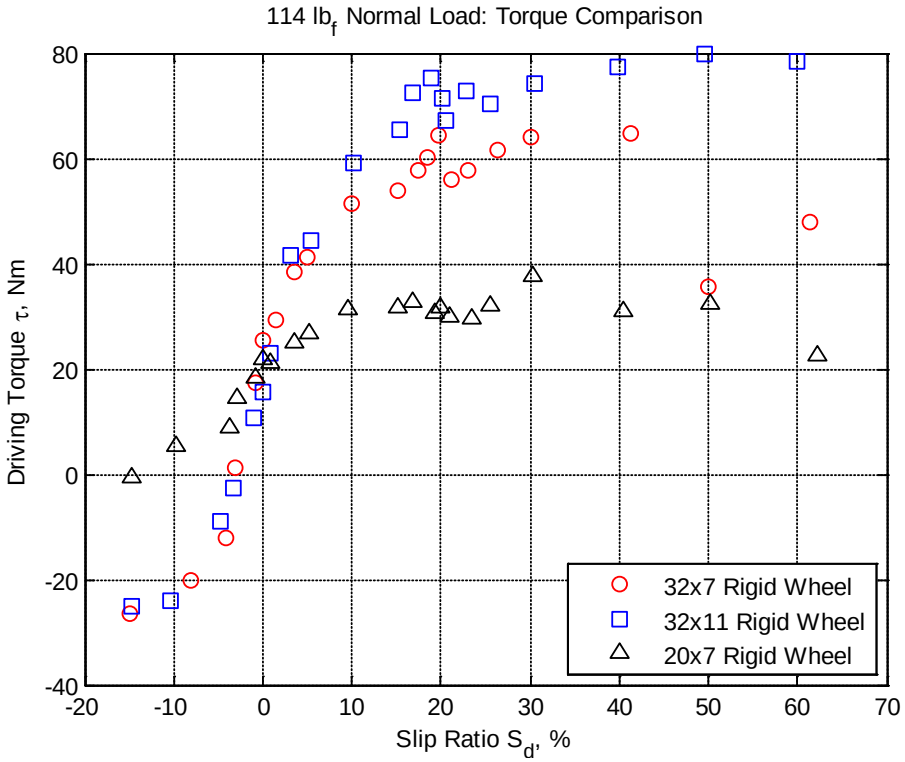

Figure 5-25. Driving torque versus wheel slip for all three rigid wheels with 114-lb_f (507.1-N) normal load.

The scatter of the data in the four plots shown above is due to the variation in normal load, as discussed in the preceding section of this chapter.

Based on the experimental results discussed in this section, it can be concluded that both contact length (wheel diameter) and wheel width directly affect the drawbar pull produced and torque required by a wheel. While wheels with larger torque requirements produce greater drawbar pull values, they also use more energy to achieve the pull values. Therefore, a balance between drawbar pull and energy usage is needed when designing wheels and tires for dry sand applications.

5.3 Experimental Results and Discussion: Pressure Pad Results

Presented in this section are some of the results of the static contact pressure tests performed using the TekScan 3150 pressure pad. The figures presented in this section are the results from the 57-lb_f (253.5-N) normal-load case. The rest of the results are presented in Appendix A.

Shown in Figure 5-26 is a snapshot of the averaged pressure distribution for the baseline 32-in. x 7-in. rigid (baseline) wheel. It should be noted that the region circled in Figure 5-26 is an area where the force read by the pressure pad was not read by the pad-computer connection. The averaging was performed to minimize the effects of the pad-computer discontinuity and random measurements caused by sensor drift and hysteresis, since the pressure pad utilizes piezoelectric measurement technology.

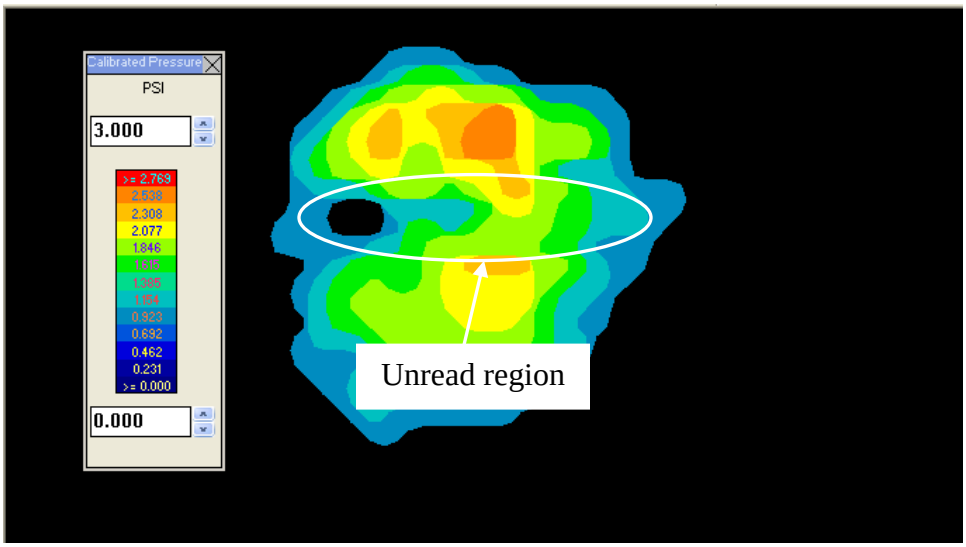

Figure 5-26. Plot of contact pressure underneath the baseline wheel.

The maximum contact pressure in this was 2.54 psi (17.51 kPa), measured over a 30.9-in.^{2} (0.01995-m^2) area.

In Figure 5-27 the averaged pressure distribution for the 32-in. x 11-in. rigid wheel is displayed with the 57-lb$_f$ (253.5-N) normal load applied.

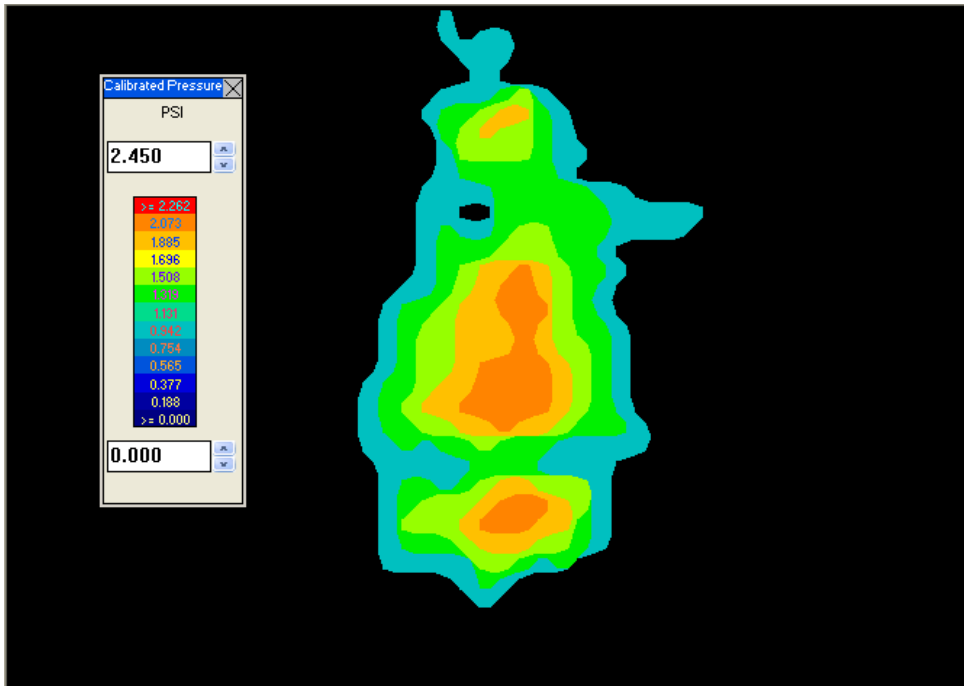

Figure 5-27. Averaged pressure distribution of the 32-in. x 11-in. rigid wheel.

As shown in Figure 5-27, the maximum contact pressure is 2.07 psi (14.27 kPa), which was over an area of 32.2 in.^{2} (0.0208 m^2).

Figure 5-28 provides a depiction of the averaged contact pressure distribution of the 20-in. x 7-in. wheel.

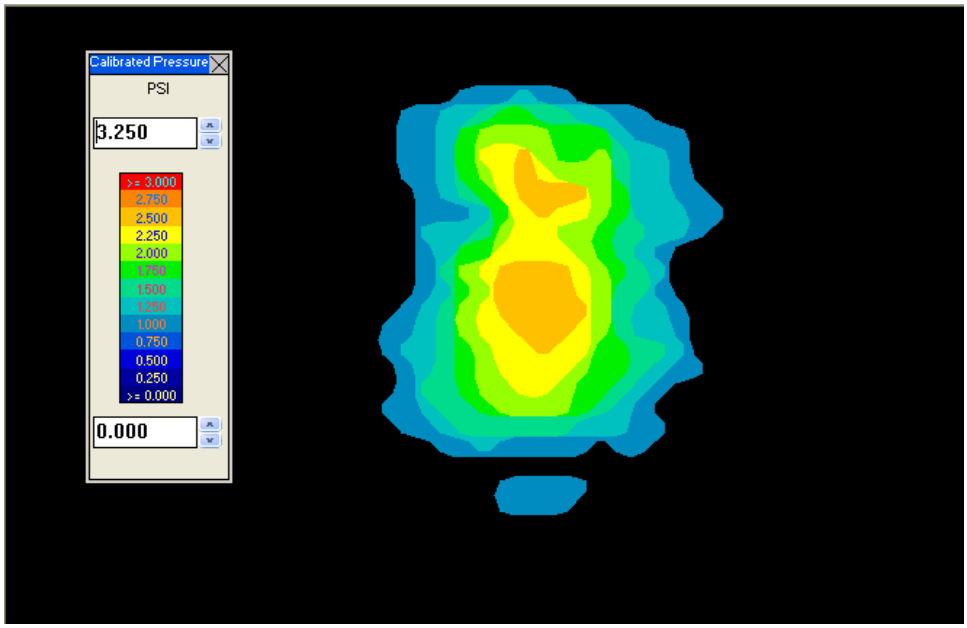

Figure 5-28. Averaged contact pressure distribution for 20-in. x 7-in. rigid wheel.

The maximum contact pressure in the above figure was measured to be 2.50 psi (17.24 kPa). The contact area over which this pressure was read was found to be 29.73 in.^{2} (0.01918 m^2).

The contact pressure distribution for the spiral wheel is shown in Figure 5-29 below.

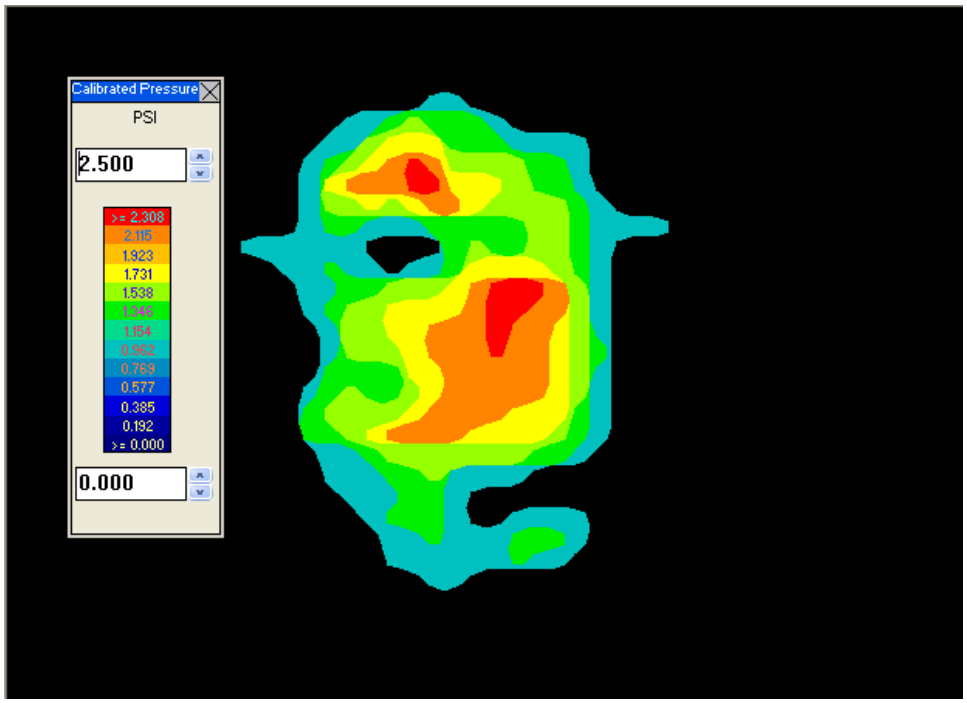

Figure 5-29. Pressure distribution plot for the spiral wheel under 57-lb$_f$ (253.5-N) normal load.

The maximum pressure that was measured for this wheel at the 57-lb_f (253.5-N) normal load was 2.48 psi (17.10 kPa) measured over an area of 31.5 $in.^2$ (0.0203 m^2).

Looking at Figures 5-26 through 5-29, it becomes apparent that the shape of the contact patches is rectangular. This can be contributed to the fact that there was no sidewall deflection in any of the wheels: three of them were rigid, and the one flexible wheel only deflected in the direction parallel to the contact length. Another observation is that for the three rigid wheels, the centers of pressure seem to converge to the center of the contact length. If the tests were performed for the rolling wheels, the centers of pressure would converge at locations more towards the front (right side in Figures 5-26 through 5-29) of the contact patch as the slip ratios increase ([1], [17], [18]). The contact areas of each wheel have been provided in Table 5-1, arranged by wheel.

Table 5-1. Tabulated contact areas for each tested wheel under experimental loading conditions.

Load Case [lb_f] (N)	**Contact Area**			
	32-in. x 7-in. Rigid	**32-in. x 11-in. Rigid**	**20-in. x 7-in. Rigid**	**32-in. x 7-in. Spiral**
57 lb_f (253.5 N)	30.9 $in.^2$ (0.01995 m^2)	32.2 $in.^2$ (0.0208 m^2)	29.7 $in.^2$ (0.01918 m^2)	31.5 $in.^2$ (0.0203 m^2)
70 lb_f (311.4 N)	32.2 in^2 (0.0208 m^2)	36.8 $in.^2$ (0.0238 m^2)	33.4 $in.^2$ (0.0216 m^2)	
80 lb_f (355.8 N)	38.0 $in.^2$ (0.0245 m^2)	44.3 $in.^2$ (0.0286 m^2)	38.0 $in.^2$ (0.0245 m^2)	
114 lb_f (507.1 N)	46.9 $in.^2$ (0.0303 m^2)	52.5 $in.^2$ (0.0339 m^2)	44.2 $in.^2$ (0.0285 m^2)	

Comparing the contact areas in Table 5-1 with the drawbar pull and torque plots discussed in the preceding section, a general correlation between contact area and tractive performance can be made for dry sand: the larger a wheel's contact patch is, the better tractive performance the wheel can achieve. This explains why people who surf-fish on sandy beaches decrease the air pressure in their vehicles' tires as to increase traction on the sand.

5.4 Experimental Results and Discussion: Summary

In this chapter we have presented experimental results of the testing performed using the four wheels discussed in this study. The first section of this chapter has provided results and discussions for each of the experimental wheels. A method of representing wheel performance

in a three-dimensional manner was introduced, and these drawbar pull and torque maps have allowed us to observe the relationship between the normal wheel load, slip ratio, and each of the dependent variables (*DP* and τ).

The second segment of this chapter has compared the performance of the four wheels, and multiple conclusions were made. Firstly, a wheel with a wider contact patch will produce higher values of driving torque and drawbar pull than a wheel of the similar diameter and smaller width. Secondly, the drawbar pull and driving torque are directly correlated to the contact patch length, as we saw that the spiral wheel performed better than the baseline rigid wheel. From this, and the observation that the 20-in.-diameter wheel produced the lowest measures of drawbar pull, one can deduce that the drawbar pull and driving torque are directly correlated with the diameter of a wheel. Because the driving torque required at the running gear of a vehicle, determines the energy requirements for any and all vehicle designs, wheel contact area should be considered in the design of wheels for any application: wheels with larger contact patch areas require more energy, according to:

$$E = \tau \cdot \omega \cdot t \tag{5.1}$$

where *E* is the energy consumed by providing a given amount of torque (τ) at a specific angular velocity (ω) over a duration of time (t). The experimental data used to create the plots in this section can be found in Appendix A.

In the final portion of this chapter, the results of the pressure pad tests are presented. These tests were performed using the TekScan 3150 Pressure Pad to determine wheel contact area on the pad, which was placed at a depth of 3 inches. The contact pressure was measured at this depth, as well. The figures shown in this section were the results of the 57-lb_f (253.5-N). The remaining pressure pad results are presented in Appendix A.

Before moving on, it should be noted that the effective radii of these wheels was not known. The effective radius is measured as the distance from the wheel center to the shearing plane within the soil. To calculate the effective radius (R_{eff}), the wheel of interest needs to be run at 0% slip, and calculated from using equation (5.2), as:

$$R_{eff} = \frac{V_x}{\omega} \tag{5.2}$$

Thus, the results presented versus the slip in this chapter should be viewed in the light of the fact that we came as close as possible to those values, but there still may be a misalignment on the slip axis of the plots shown in this chapter.

6. Modeling Results and Discussion

The wheel model employed in this study has been extensively discussed in [18], and it will be briefly introduced here. Simulation results from the three rigid wheels tested are presented in this chapter for each load case. Comparisons of the tractive performance of these three wheels, as predicted by the simulation models will be provided here as well. The final section in this chapter will compare the experimental and the modeling results in an effort to validate the simulation model. Supplemental plots are shown in Appendix A. It should be mentioned that this is a preliminary attempt to bring this rigid ring model into comparison with experimental data.

The model that was used in this study utilizes the inputs of slip ratio (s_d), normal load (F_z), slip angle (α_c), camber angle (γ), and angular wheel velocity (ω) for a wheel with a given width (b) and undeflected radius (R_u); it outputs the drawbar pull (DP), driving torque (τ), lateral force (F_c), aligning moment (M_z), overturning moment (M_x), and wheel sinkage (z). Also, it outputs the normal stress, the soil shear stress (in both *x*- and *y*-directions), and a projection of the wheel shape, in the soil, from the side. The relevant outputs that will be discussed in this chapter are the drawbar pull, driving torque, and wheel sinkage, since the simulations will be run with neither steering nor cambering involved.

6.1 Modeling Results and Discussion: Individual Wheel Performance

The purpose of this section is to present the results obtained applying the model discussed in [18] for each of the rigid wheels tested in this study. The results of the 32-in. x 7-in. wheel under all four normal loads are shown in Figures 6-1 and 6-2.

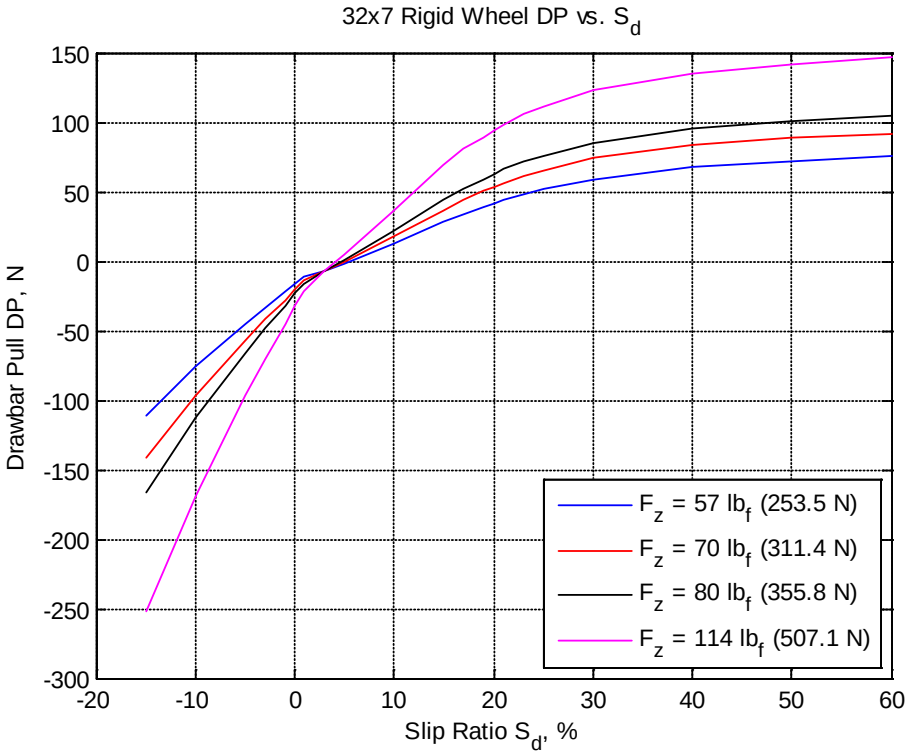

Figure 6-1. *DP* vs. S_d for the 32-in. x 7-in. rigid wheel for all four normal loads.

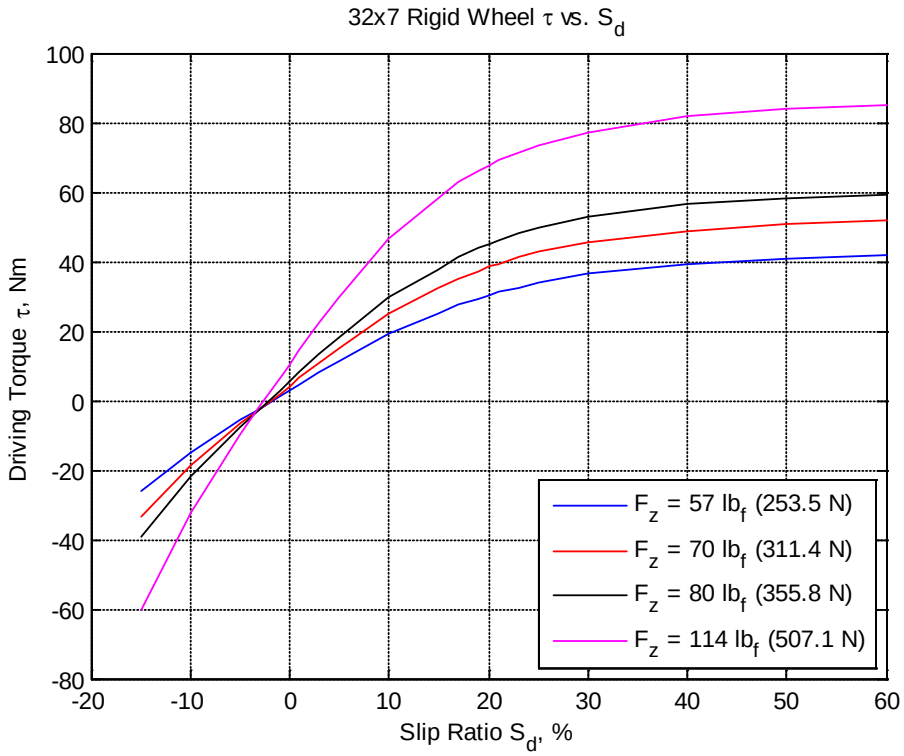

Figure 6-2. Torque vs. slip ratio for the 32-in. x 7-in. rigid wheel for all four normal loads.

In Figure 6-1 there is a clear asymmetric alignment of the drawbar pull values, which is leaning towards the negative slip range. This can be compared to a real-world scenario in which a vehicle is braking and the wheels would begin digging into the sand; at higher slip values this piling of sand would become very obvious. The wheel also begins to reach its traction limit around +20% slip. While the drawbar pull still increases beyond this point, running wheeled vehicles at slips higher than this would lead to a decrease in vehicle forward speed and could eventually cause the vehicle to get stuck. The driving-torque curves in Figure 6-2 begin to level off around +20% slip, as well.

Shown in Figures 6-3 and 6-4 are the pull and torque curves versus slip ratio for the 32-in. x 11-in. rigid wheel.

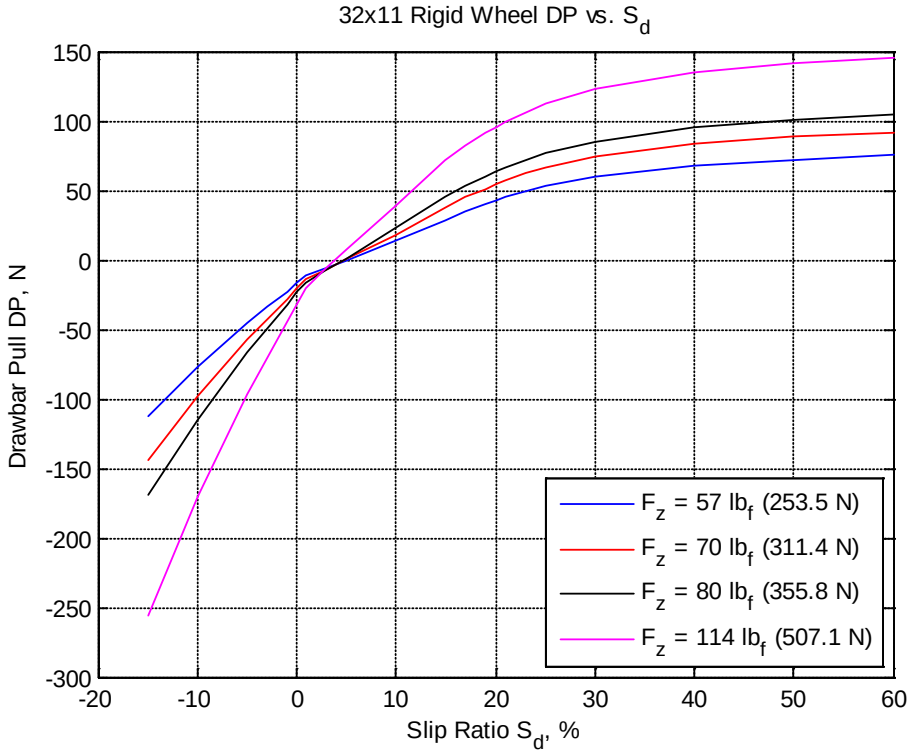

Figure 6-3. Pull vs. slip ratio for the 32-in. x 11-in. rigid wheel for all normal loads.

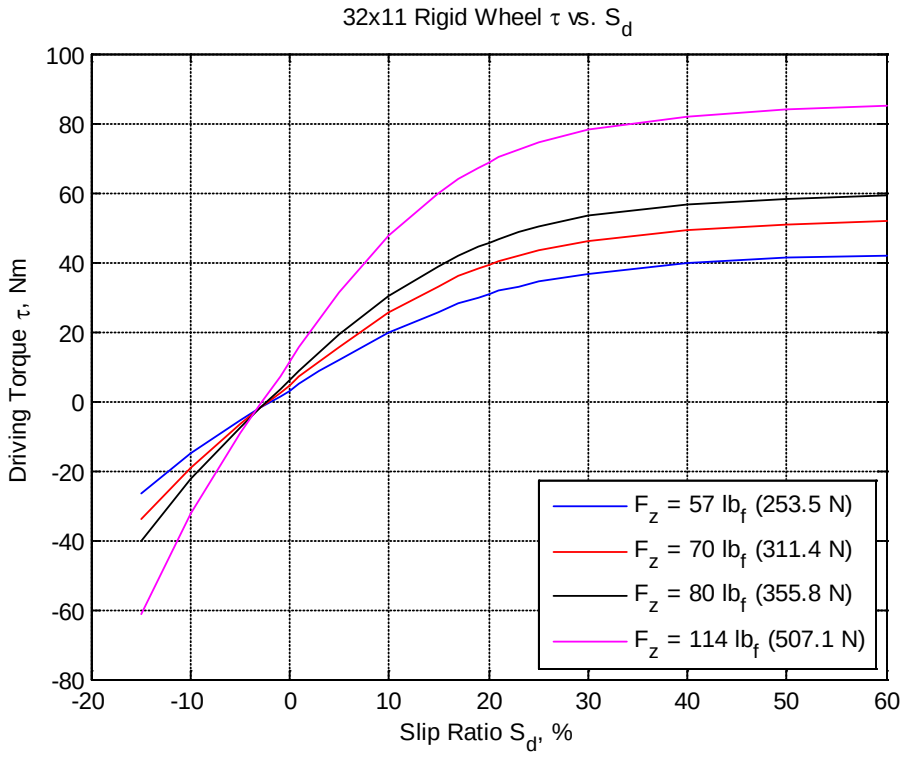

Figure 6-4. Torque versus slip ratio for the 32-in. x 11-in. wheel for all four normal loads.

Similar to the baseline wheel, this 11-in.-wide wheel is asymmetric, favoring the negative slip range. Also similar is fact that at +20% slip, the *DP*-values began to level off and approach the traction limit. From Figure 6-4 the torque-values start to reach their limit around +20% slip, as well.

Figures 6-5 and 6-6 provide visual representations of the drawbar pull and torque curves for the 20-in. x 7-in. rigid wheel when subjected to all four normal loads.

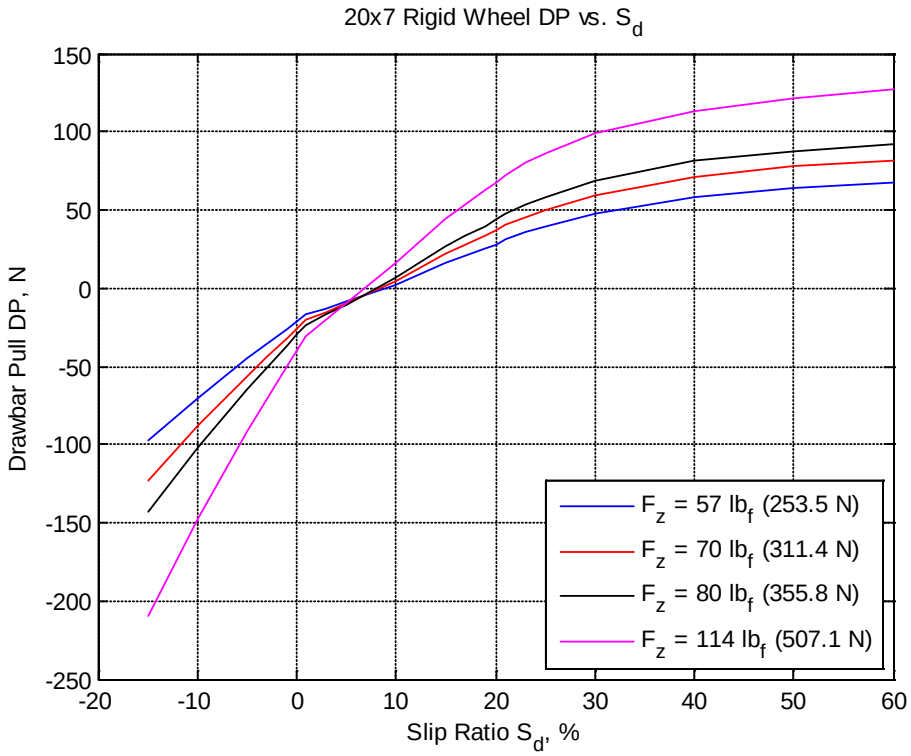

Figure 6-5. Drawbar pull vs. slip ratio for the 20-in. x 7-in. wheel for all normal loads.

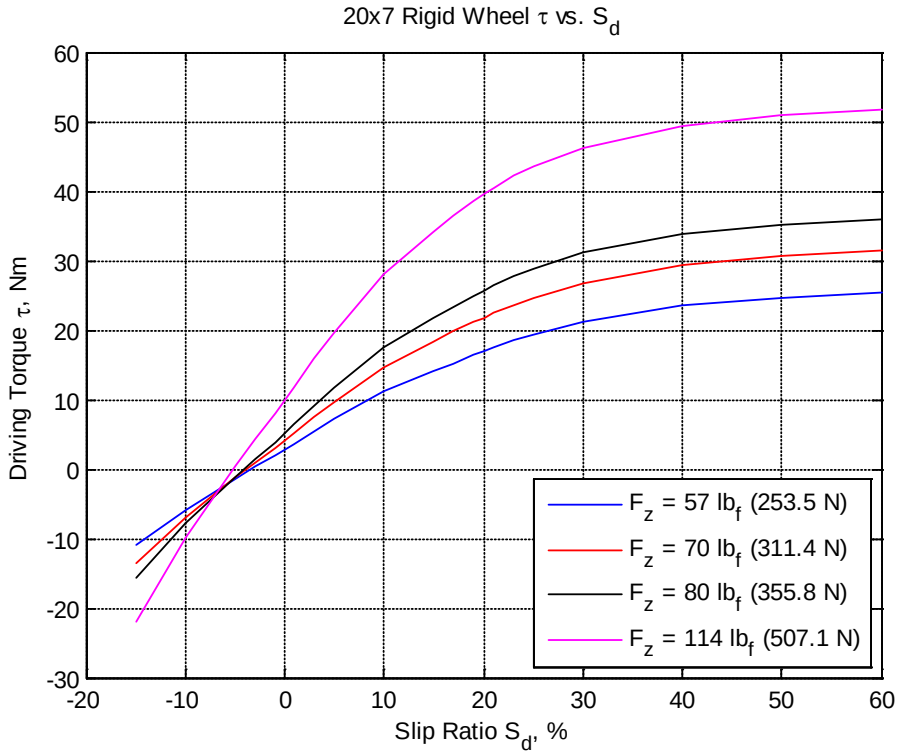

Figure 6-6. τ vs. S_d for 20-in. x 7-in. wheel under all four normal loads.

Much like with the preceding two wheels, Figure 6-5 shows that the 20-in. x 7-in. rigid wheel is heavily weighted towards the negative slip range in terms of maximum absolute values. But unlike the preceding two wheels, this wheel's traction limit did not become obvious until about +23% slip. As for the wheel torque-versus-slip plot in Figure 6-6, the values of torque start to level off around +20% slip. This seems to be a common trend among the three wheels that have been modeled.

6.2 Modeling Results and Discussion: Wheel Comparison

This section will be used to compare the performance of the three rigid wheels that were modeled. Before beginning the presentation of results, some clarification about the method used in finding the exit angles is provided in this section.

6.2.1 Exit Angle Determination

While the relevant modeling inputs discussed in the beginning of this chapter are similar to the experimental inputs discussed in Chapter 4, the model includes another "input" that was not part of the discussion on the design of experiment: the wheel exit angle (θ_b). The exit angle is important since it is used as one of the limits of integration to compute the normal wheel load, the drawbar pull, and the wheel toque, as shown in equations (2.18) - (2.20). As shown in Figure 2-1, the exit angle is formed by the normal to the contact patch and the radial direction given by the last point of contact between the wheel and the soil. As such, exit angles are, in general, very difficult parameters to estimate, because they depend on several factors. For example, the soil type is very important. For a rigid wheel and a given normal load, if the soil is plastic, the exit angle will be very small, since the last point of contact between the wheel and the terrain will be almost identical to the projection point of the normal to the contact patch. If, on the other hand, the soil has some elasticity in it, during the unloading phase the soil behind the wheel will achieve a larger height than the plastic soil, and thus the exit angle will be larger in this case. The exit angle is also dependent on the slip, since higher slips may induce piling of soil behind the wheel, as well as an increase in sinkage. The normal load is one of the important factors related to the exit angle, too. For the same wheel, an increase in the wheel load will lead to more sinkage, and, consequently, to a larger exit angle. Of course, the wheel sinkage and the exit

angle are related, regardless of the means by which a certain sinkage occurs. This will be discussed in more details later in this chapter.

While the exit angle cannot be accurately predicted by a theoretical model, an empirical equation discussed in [21] and shown here in equation (6.1) may be employed to estimate it.

$$\theta_b = \frac{F_z}{1000} a \tag{6.1}$$

where a is a dimensionless coefficient that depends on terrain factors. For example, for the sandy loam used to model the tire in [18], a = [0.8, 1.2]. This parameter is usually considered based on experimental measurements and experience.

While equation (6.1) may be one means of determining the exit angle of certain tires and wheels, there is nothing relating wheel slip to the exit angle of a rigid wheel. It is this author's argument that slip ratio also plays a significant role in predicting the exit angle of wheels and tires. With this in mind, the results presented in the first section of this chapter have been found using the same range of exit angles for all three wheels. In the second part of this chapter, the performance of the three rigid wheels is compared using the same exit angles. However, the wheels' performance are also compared using different exit angles for the 32-in. x 11-in. wheel to observe how these changes affect the modeling output, since using the same exit angle for two wheels of the same diameter, under the same load, but with different widths imposes the same sinkage for the two rigid wheels, which is unrealistic. Shown in Figure 6-7 is a wheel diagram with a small exit angle, and in Figure 6-8 is a wheel with a larger exit angle.

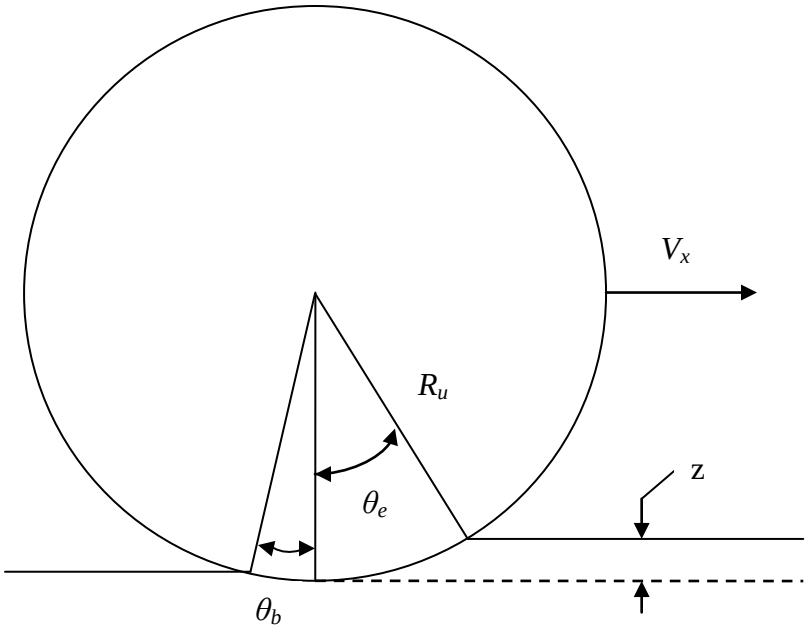

Figure 6-7. Diagram of wheel with small exit angle.

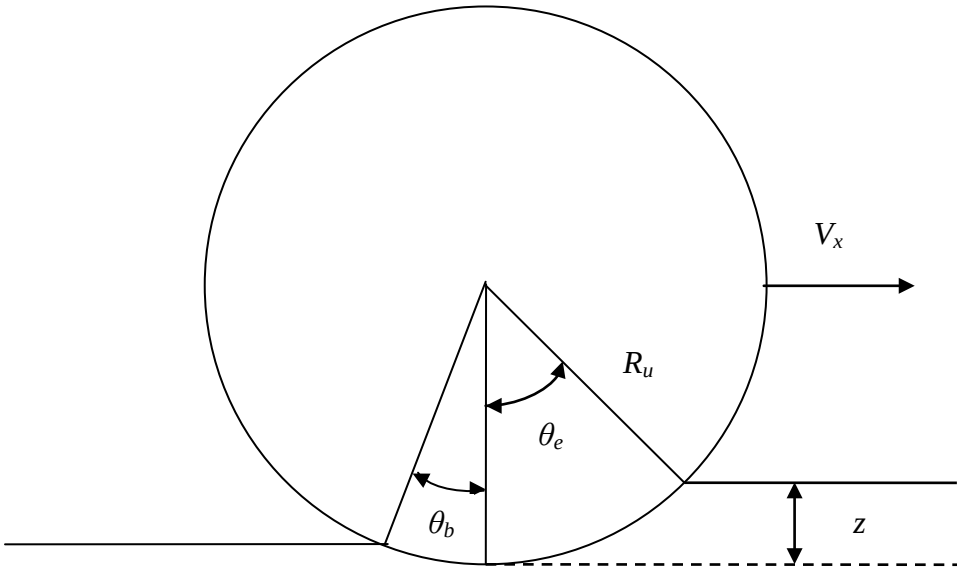

Figure 6-8. Diagram of wheel with large exit angle.

The exit angles used in the model are displayed in Table 6-1, and vary based on slip ratio.

Table 6-1. Exit angles used to model the rigid wheels.

S_d (%)	$\theta_{b,1}\left(^\circ\right)$	$\theta_{b,2}\left(^\circ\right)$
-15	0	0
-10	0	0
-5	0	0
-3	0	0
-1	0	0
0	0	0
1	-1.0	-0.6363
3	-1.0	-0.6363
5	-2	-1.090
10	-5.1	-5.01
15	-5.75	-5.05
17	-5.875	-5.075
19	-6.0	-5.10
20	-6.25	-5.1125
21	-6.50	-5.125
23	-6.75	-5.1375
25	-7.0	-5.1625
30	-7.5	-5.2025
40	-8.0	-5.305
50	-8.5	-5.4075
60	-9.0	-5.51

The reason for changing the exit angles in the third column of the table, and only applying them to the 11-in.-wide wheel, stemmed from concern over wheel-sinkage values predicted by the model using the exit angles listed in the second column. The simulation results obtained with the exit angle values from the second column were counterintuitive in that under the same normal load, the 32-in. x 11-in. wheel sank deeper than the 32-in. x 7-in. wheel. From the pressure pad results in Chapter 5, it is clear that the 7-in.-wide wheel exerts greater contact pressure than the 11-in.-wide wheel.

The exit angles listed in the third column were originally determined using a ratio of the 11-in.-wide wheel to the 7-in.-wide wheel, such that a factor of $b_{11"}/b_{7"} = 1.5715$ was used. A downside to using this factor was that it could not be used for slip ratios greater than or equal to +10%; the resulting exit angles caused the model to output an error message. Thus, the minimum allowable exit angles were used for the remainder of the slip range. Plots of the

sinkage values using equal exit angles and unequal exit angles are presented in Figures 6-9 and 6-10, respectively.

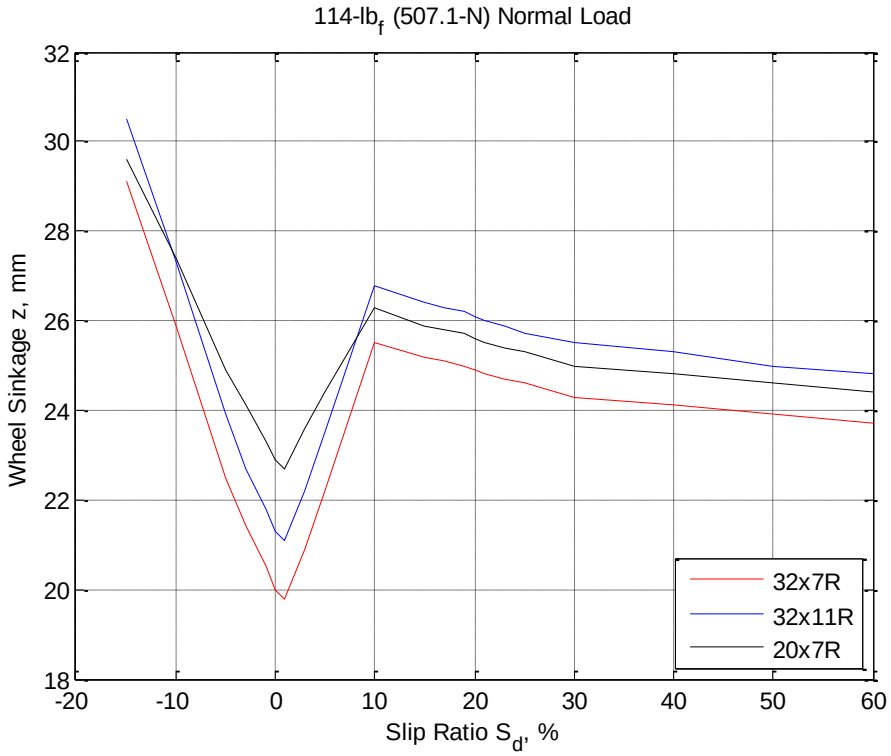

Figure 6-9. Modeling output of sinkage vs. slip ratios for the three rigid wheels with equal exit angles.

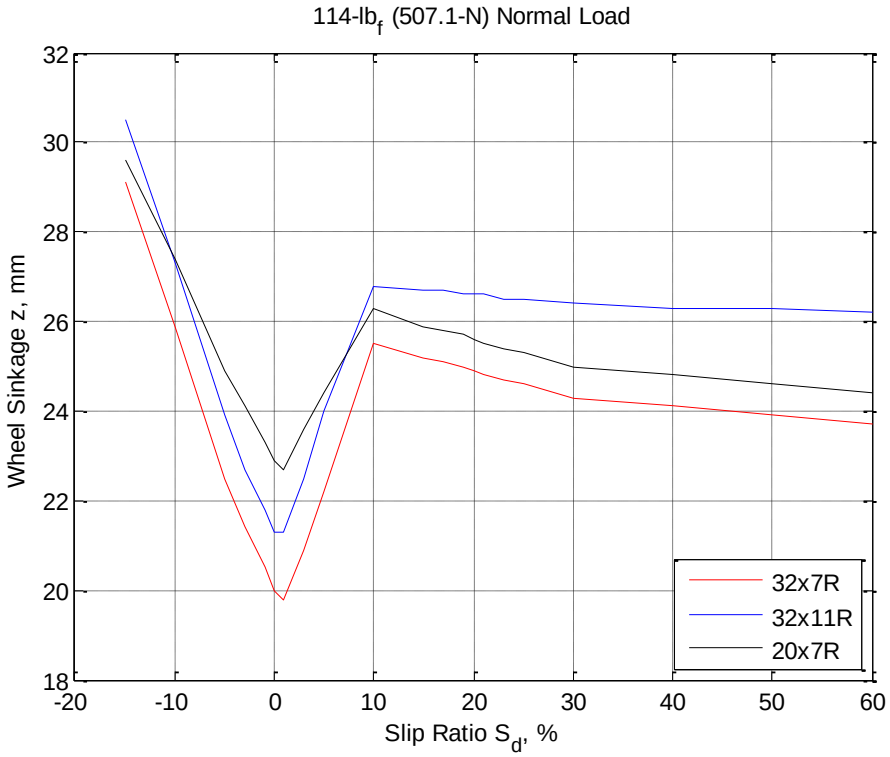

Figure 6-10. Modeling output of sinkage vs. slip ratios for the three rigid wheels with unequal exit angles.

The results depicted in Figure 6-9 and 6-10 are counterintuitive to what seems like common sense: that a wider wheel will sink less than a thinner one if both are the same diameter, on the same terrain, and subjected to the same normal load. Even though the cause of such a discrepancy most likely results from the exit angles used in the model, the difference in sinkage between the 32-in. x 7-in. and the 32-in. x 11-in. wheels does not change very much at all, staying between 0.5 mm and 0.75 mm for slip ratios values below +10%, and between 1 and 2 mm for slip ratios above +10%.

The issue of correctly estimating the exit angle to be used in the simulation model of rigid wheels calls for further studies to be done in evaluating exit angles while performing wheel tests, and perhaps even deriving an empirical method of estimating them based on normal load, slip ratio, contact area, and terrain conditions. A suggested method of measuring exit angles during tests is presented in the Recommendations portion of Chapter 7.

6.2.2 Results Using Same Exit Angles

In Figures 6-11 through 6-14, the drawbar pull versus slip ratio model results are presented, with respect to the each normal load.

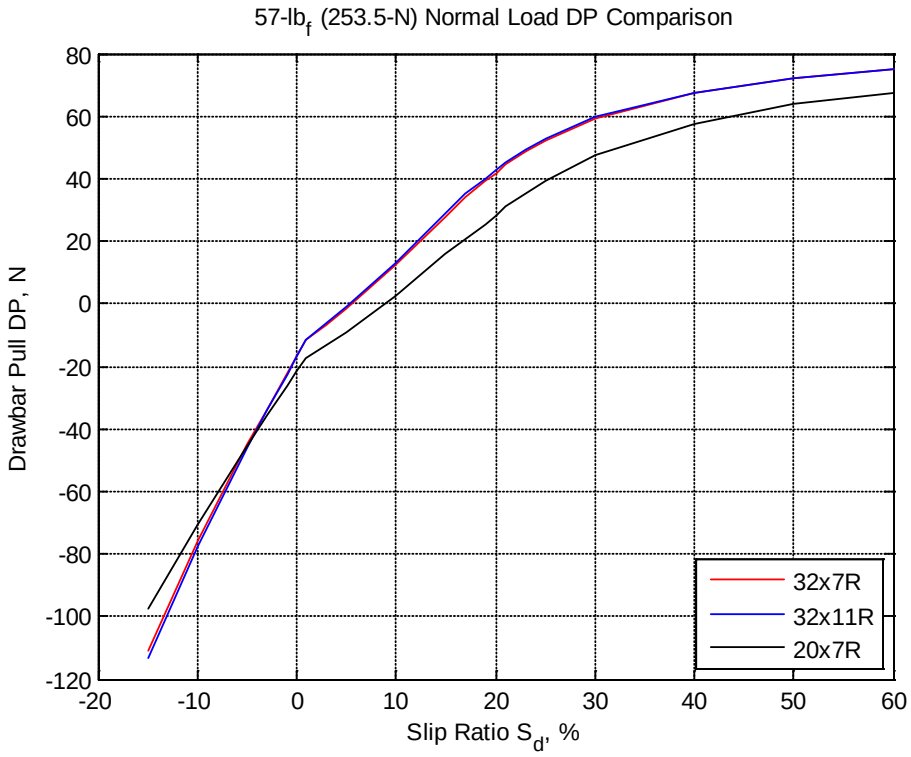

Figure 6-11. *DP* vs. S_d model results for the 57-lb_f (253.5-N) normal load.

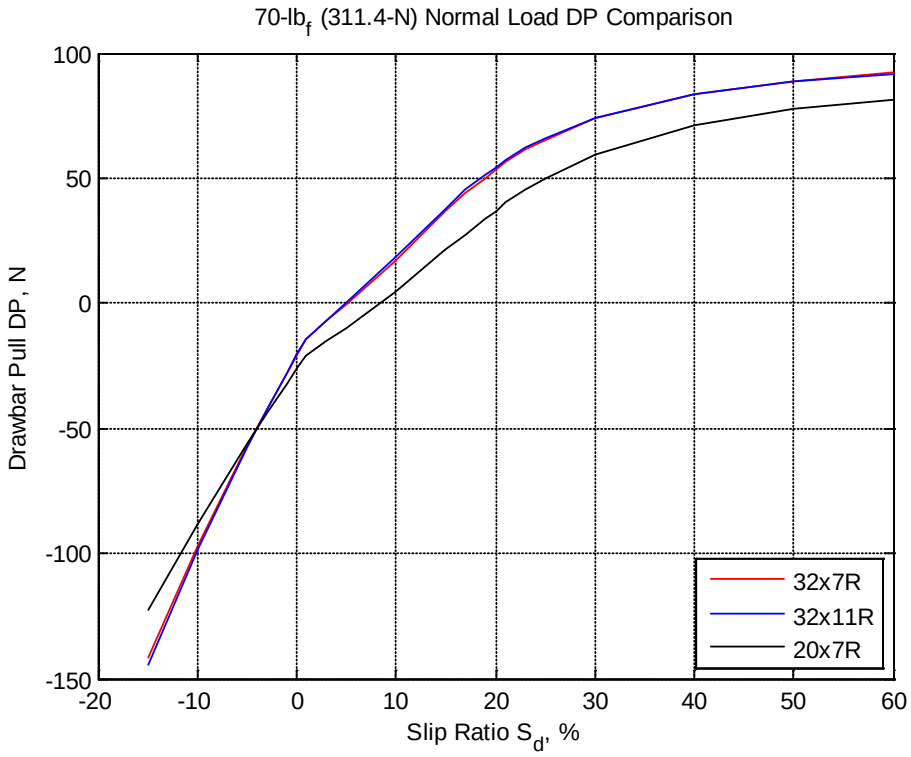

Figure 6-12. *DP* vs. S_d model results for the 70-lb_f (311.4-N) normal load.

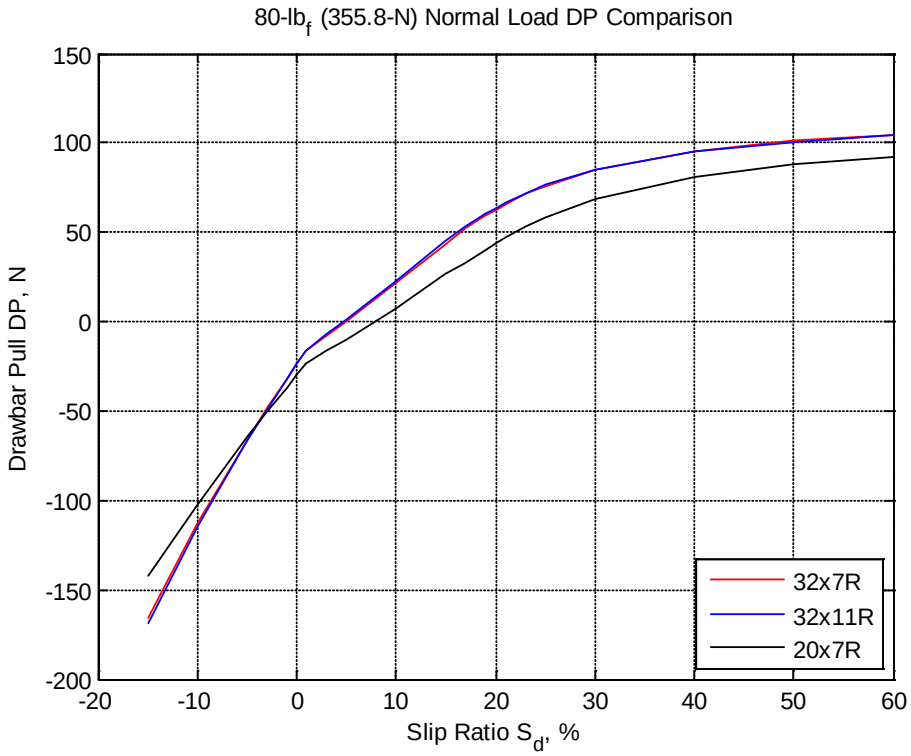

Figure 6-13. *DP* vs. S_d model results for the 80-lb_f (355.8-N) normal load.

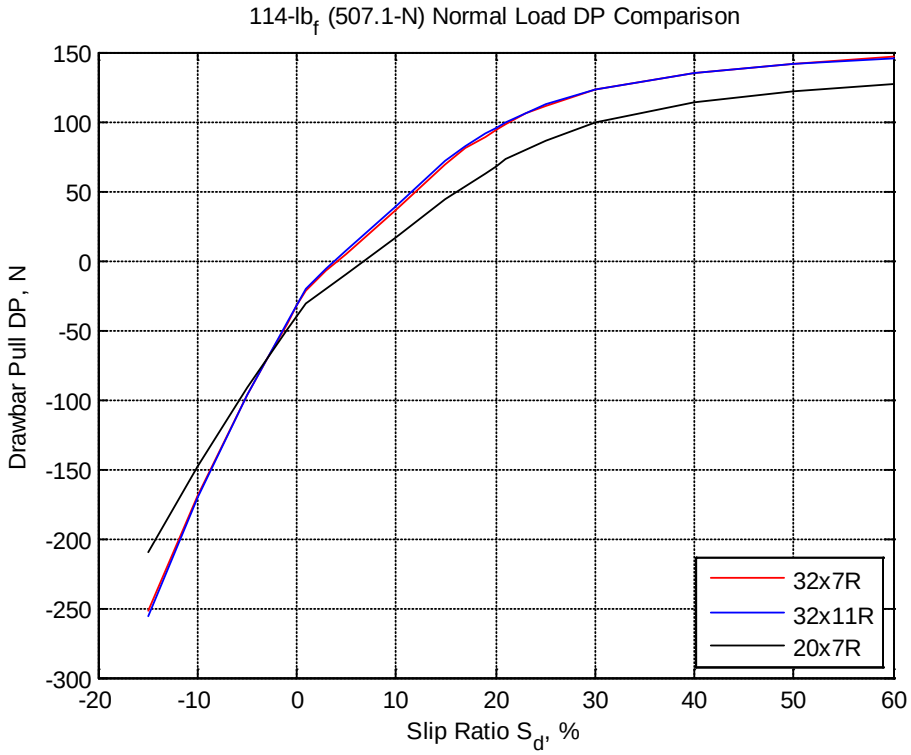

Figure 6-14. *DP* vs. S_d model results for the 114-lb_f (507.1-N) normal load.

The plots shown in Figures 6-11 through 6-14 are correct in that the 20-in. x 7-in. wheel's performance ranks last among the three wheels. On the other hand, both the baseline wheel and the 11-in.-wide wheel perform at virtually the same level. This is also counterintuitive because in the model, the drawbar pull is directly correlated to wheel width, as discussed in the literature review chapter, and revisited here:

$$DP = R_u b\left(\int_{-\theta_r}^{\theta_e} \tau_x(\theta)\cos(\theta)\,d\theta - \int_{-\theta_r}^{\theta_e} \sigma_n(\theta)\sin(\theta)\,d\theta\right) \tag{6.2}$$

where R_u is the wheel radius, b is the wheel width, θ is any angle made with the vertical axis that lies between the entry (θ_e) and exit (θ_r) angles of the wheel-soil contact patch, and τ_x and σ_n are the shear and radial (normal) stresses on the soil, respectively [18]. From this relationship, the wider wheel should produce greater pull values. It should be noted that the discrepancy discussed here originally led to the investigation into the exit angle's impact on the modeling results.

Shown in Figures 6-15 through 6-18 are the results of the driving torque predicted for the three wheels by the model for each normal load.

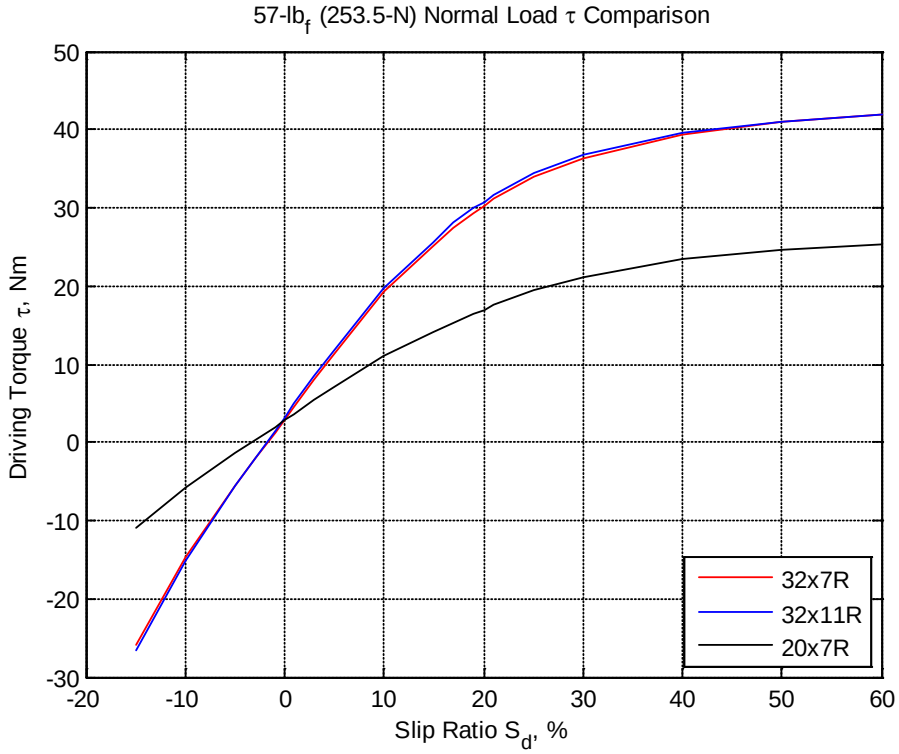

Figure 6-15. Driving torque vs. slip ratio for three wheels at 57-lb_f (253.5-N) normal load.

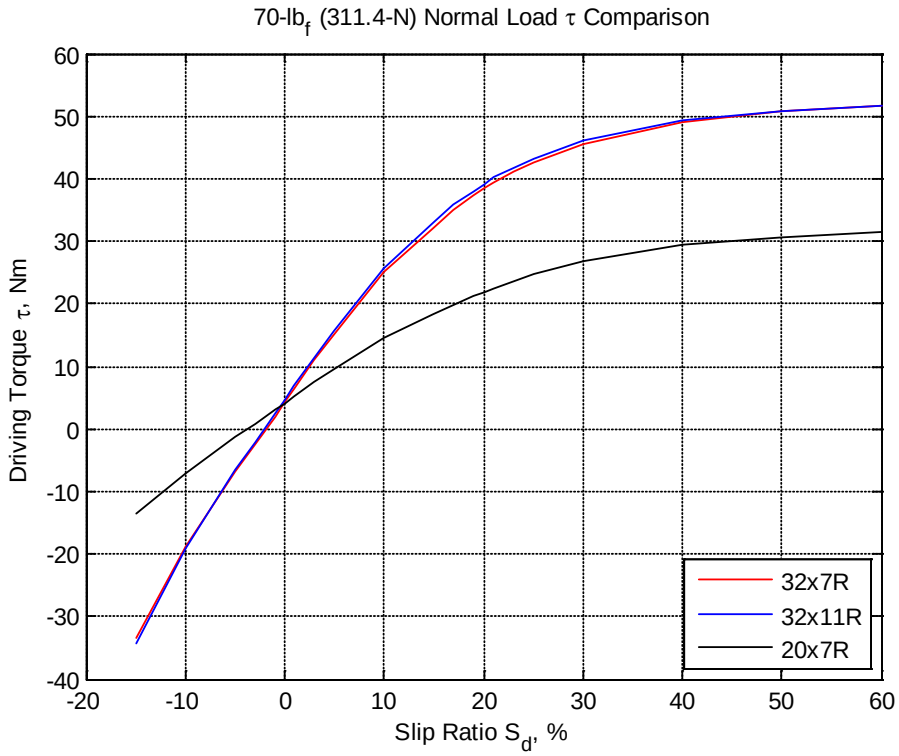

Figure 6-16. Driving torque vs. slip ratio for three wheels at 70-lb_f (311.4-N) normal load.

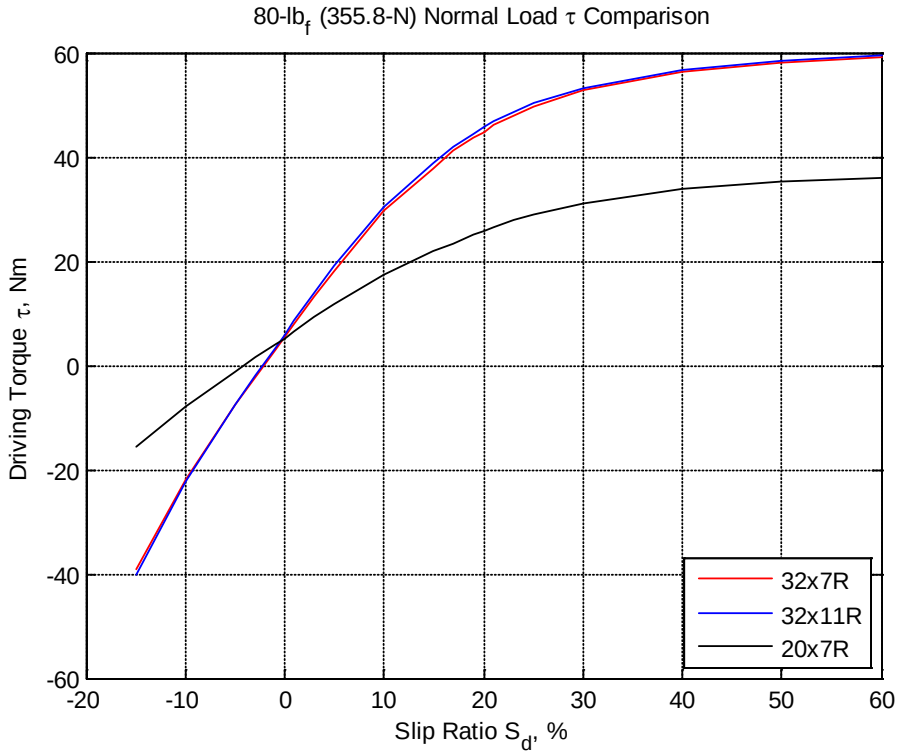

Figure 6-17. Driving torque vs. slip ratio for three wheels at 80-lb_f (355.8-N) normal load.

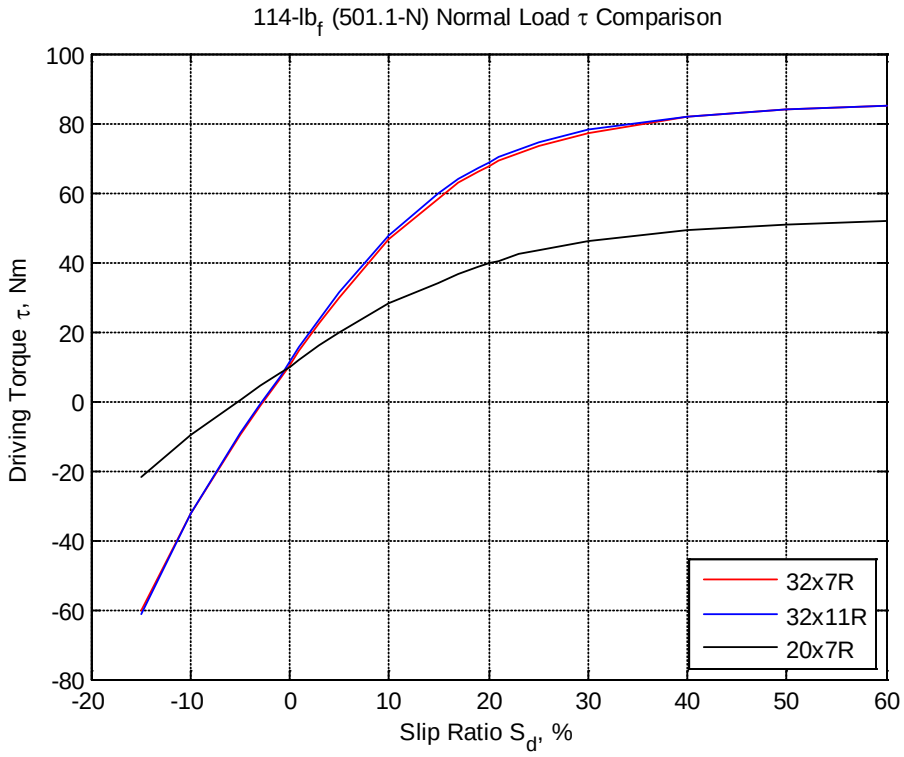

Figure 6-18. Driving torque vs. slip ratio for three wheels at 114-lb_f (507.1-N) normal load.

The results plotted in Figures 6-15 through 6-18 show that the 20-in.-diameter wheel needed less driving torque than the other two wheels, as would be expected. Recall driving torque and the square of the wheel radius are directly correlated, as:

$$T = R_u^2 b \int_{-\theta_r}^{\theta_e} \tau_x(\theta)\, d\theta \tag{6.3}$$

As for the 32-in. x 7-in. and the 32-in. x 11-in. wheels, the results are virtually coincident, just as they were in the drawbar pull comparison plots. The only conclusion that can be made at with the current data is that the driving torque for the 20-in.-diameter wheel is significantly less than for both 32-in.-diameter wheels.

6.2.2 Results Using Different Exit Angles

The results presented in this portion of the chapter were found using the second set of exit angles, listed in the third column of Table 6-1, as the exit angles or the 32-in. x 11-in. wheel. Drawbar pull results are presented in Figures 6-19 through 6-22.

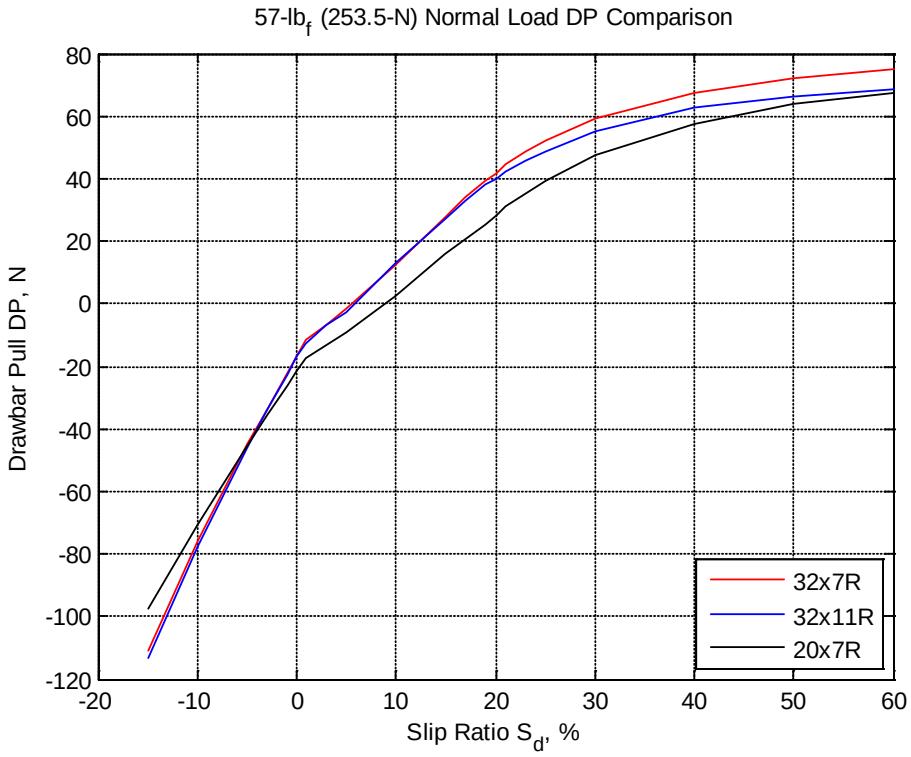

Figure 6-19. *DP* vs. S_d plots for three wheels under 57-lb_f (253.5-N) normal load, using unequal exit angles.

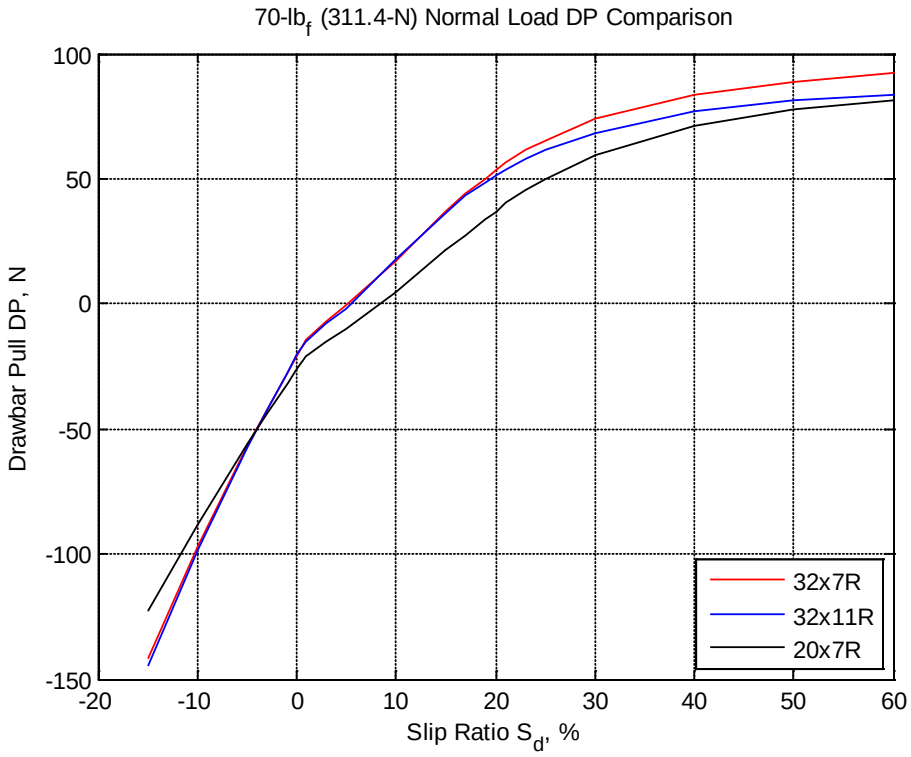

Figure 6-20. *DP* vs. S_d plots for three wheels under 70-lb_f (311.4-N) normal load, using unequal exit angles.

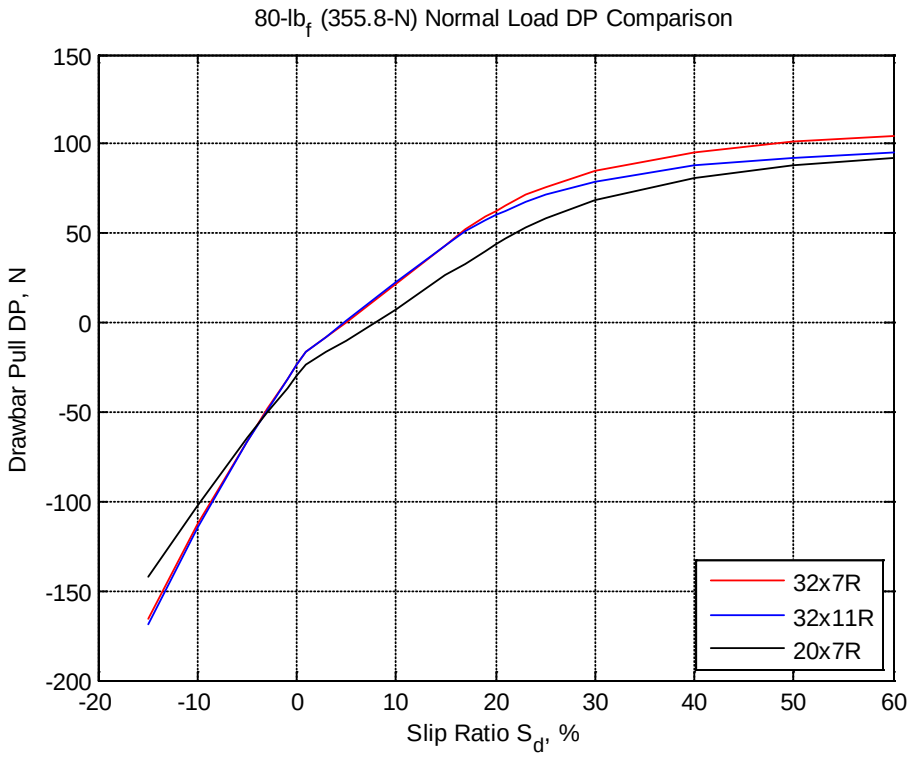

Figure 6-21. *DP* vs. S_d plots for three wheels under 80-lb_f (355.8-N) normal load, using unequal exit angles.

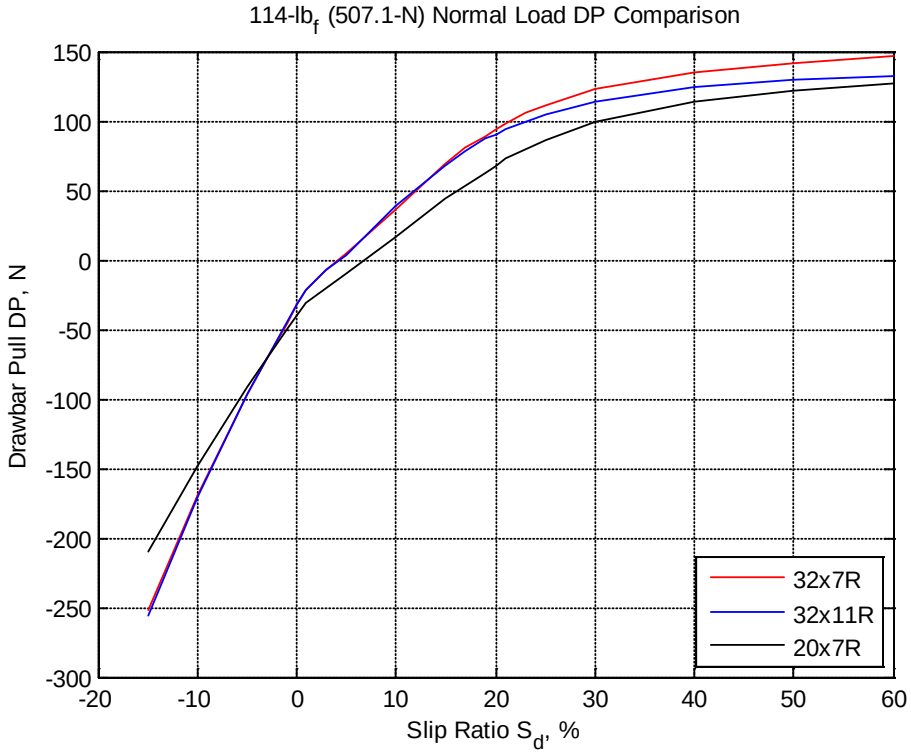

Figure 6-22. *DP* vs. S_d plots for three wheels under 114-lb_f (507.1-N) normal load, using unequal exit angles.

In the drawbar pull plots shown above, the 32-in. wheels' results remain coincident until reaching of slip ratio near +17%, at which point the 11-in.-wide wheel actually produces less drawbar pull than its 7-in.-wide counterpart.

The driving torque modeling results are shown in Figures 6-23 through 6-26.

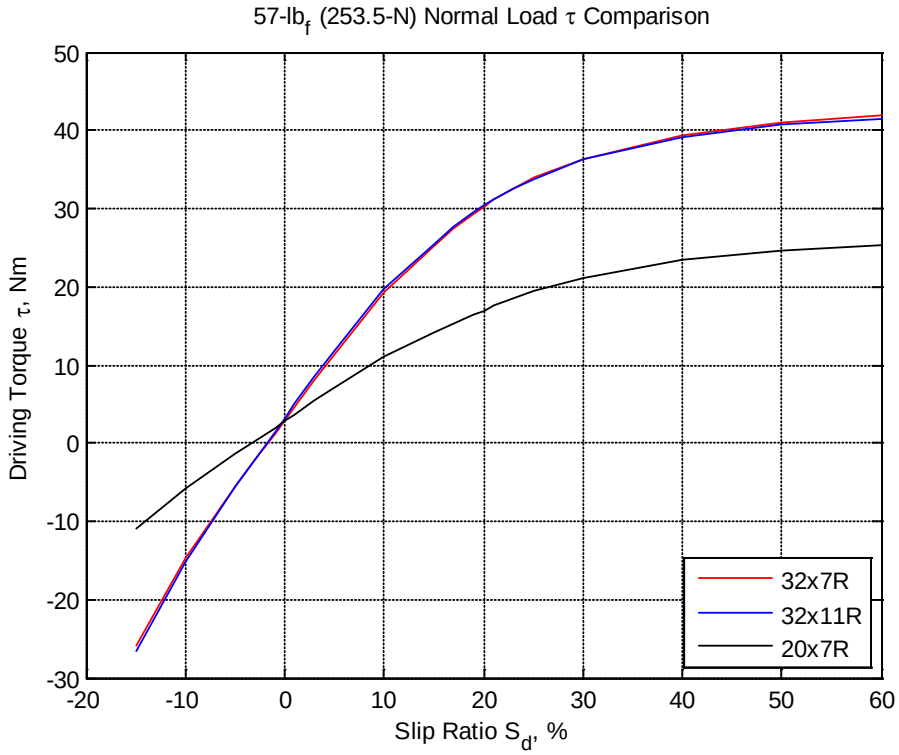

Figure 6-23. τ vs. S_d plots for three wheels under 57-lb$_f$ (253.5-N) normal load, using unequal exit angles.

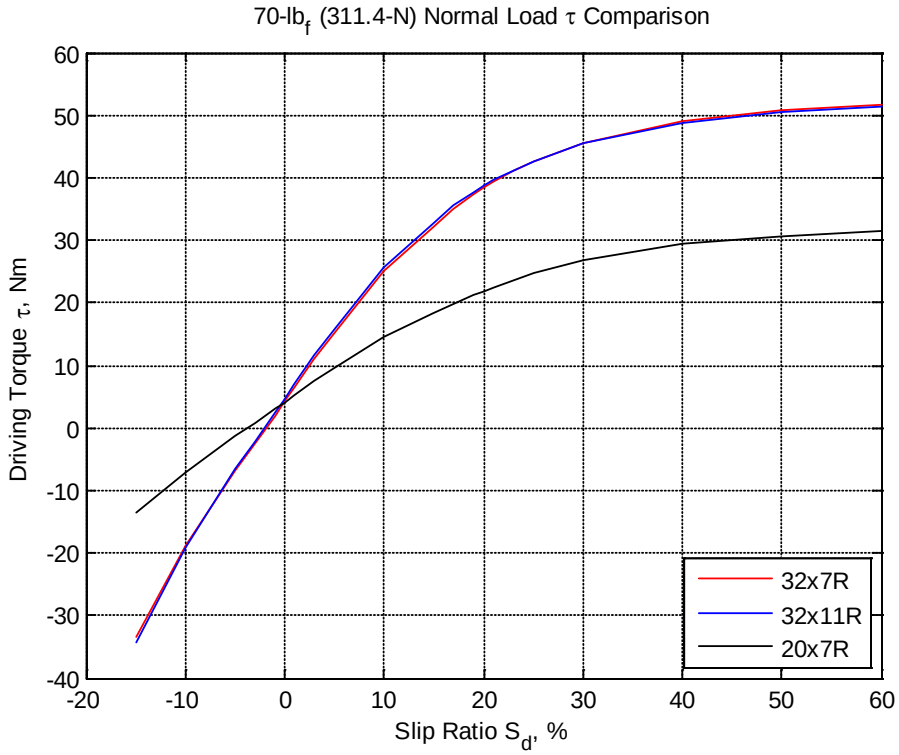

Figure 6-24. τ vs. S_d plots for three wheels under 70-lb$_f$ (311.4-N) normal load, using unequal exit angles.

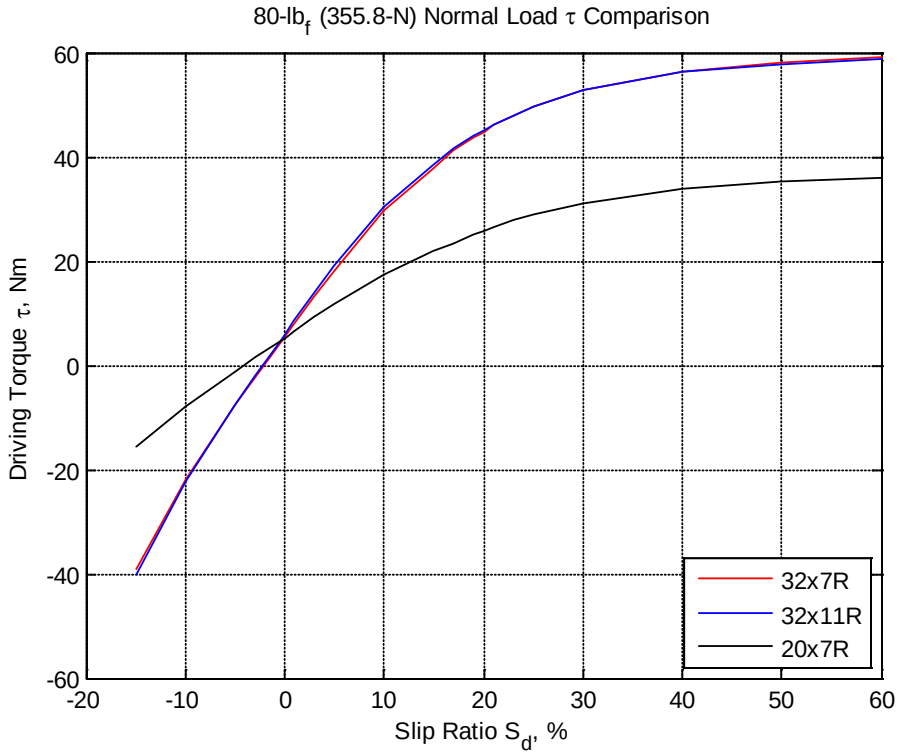

Figure 6-25. τ vs. S_d plots for three wheels under 80-lb$_f$ (355.8-N) normal load, using unequal exit angles.

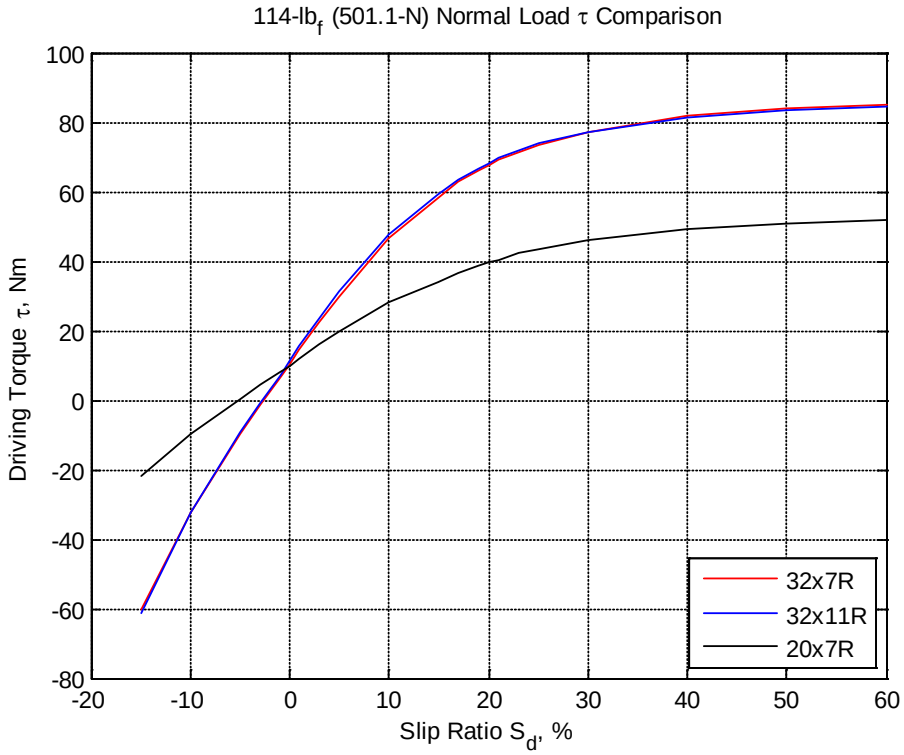

Figure 6-26. τ vs. S_d plots for three wheels under 114-lb_f (507.1-N) normal load, using unequal exit angles.

Despite the change in exit angles, the torque curves in Figures 6-23 through 6-26 remained virtually unchanged. The 20-in.-diameter wheel needed less driving torque, compared to the two 32-in.-diameter wheels. Again, the torque curves of the 32-in. x 7-in. and 32-in. x 11-in. wheels were nearly coincident over the entire range of slip ratios.

6.3 Modeling Results and Discussion: Validation

In this section the modeling results will be plotted on the same axes as the wheel experimental results in an attempt to validate the model. The remaining validation plots are located in Appendix A. Shown in Figures 6-27 and 6-28 are the plots of drawbar pull and driving torque versus slip ratio for the baseline 32-in. x 7-in. wheel under the 57-lb_f (253.5-N) and 70-lb_f (311.4-N) normal loads.

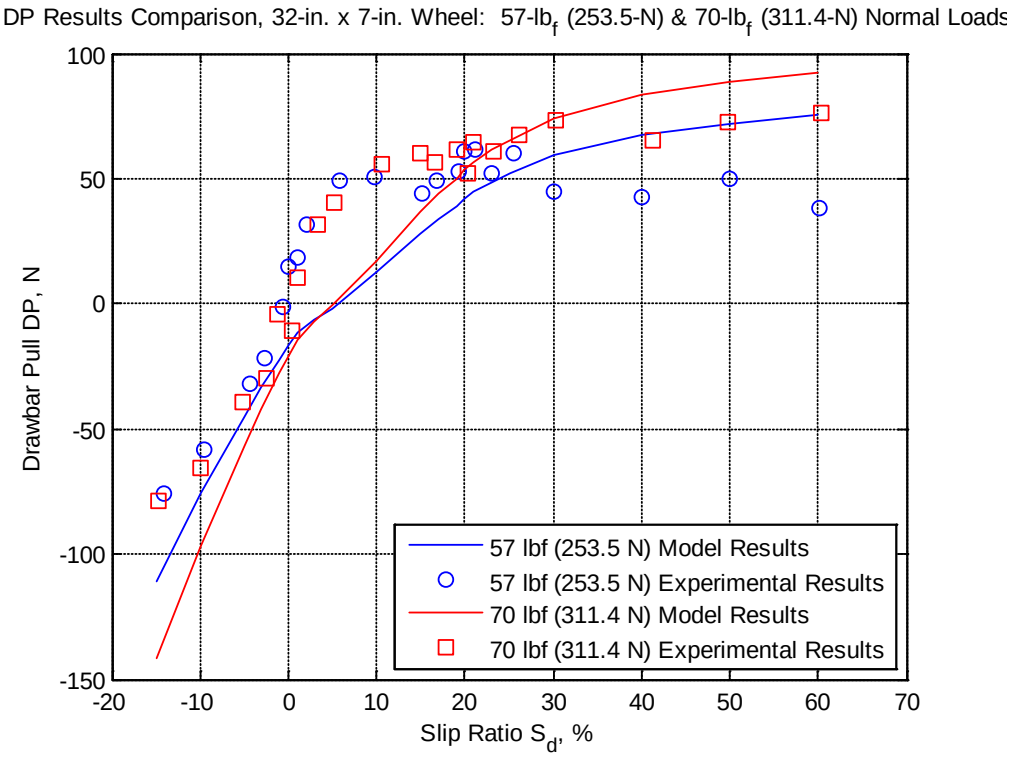

Figure 6-27. Modeling and experimental results for *DP* vs. S_d for 32-in. x 7-in. wheel at 253.5-N and 311.4-N normal loads.

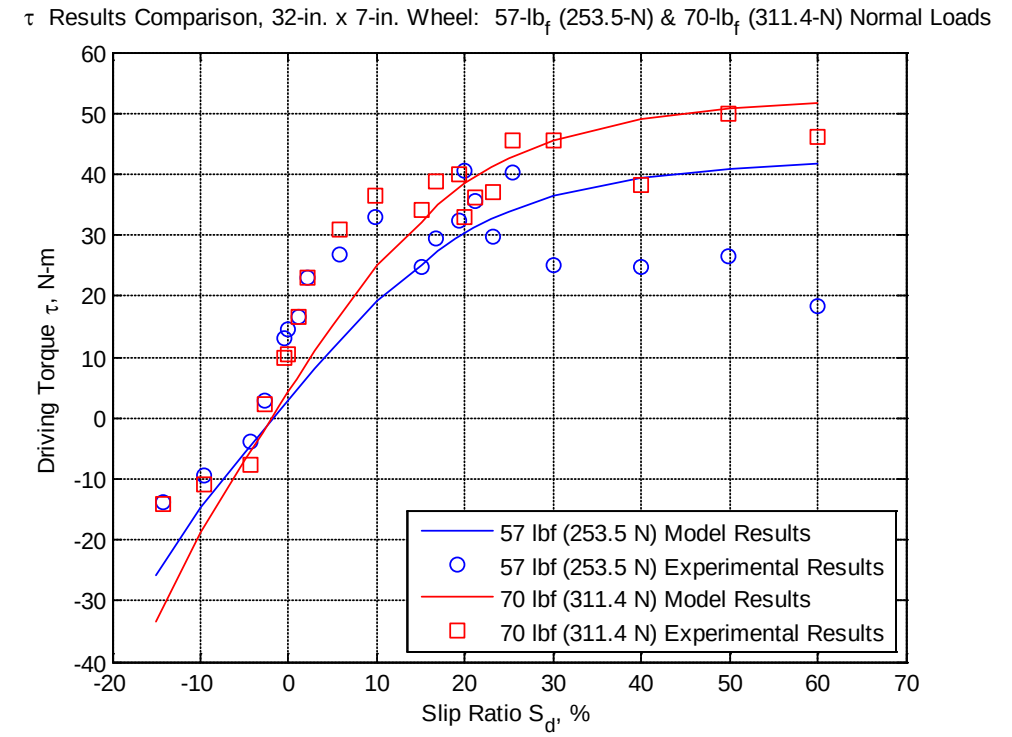

Figure 6-28. Modeling and experimental results for τ vs. S_d for 32-in. x 7-in. wheel at 253.5-N and 311.4-N normal loads.

Figures 6-29 and 6-30 provide similar graphical comparisons for the 32-in. x 11-in. wheel.

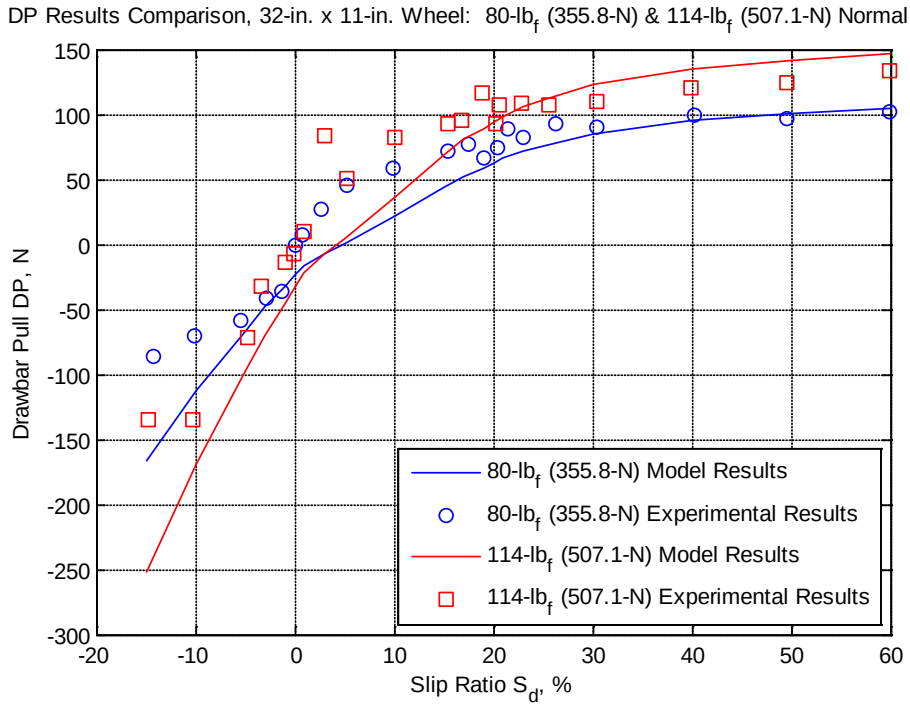

Figure 6-29. Modeling and experimental results for *DP* vs. S_d for 32-in. x 11-in. wheel at 355.8-N and 507.1-N normal loads.

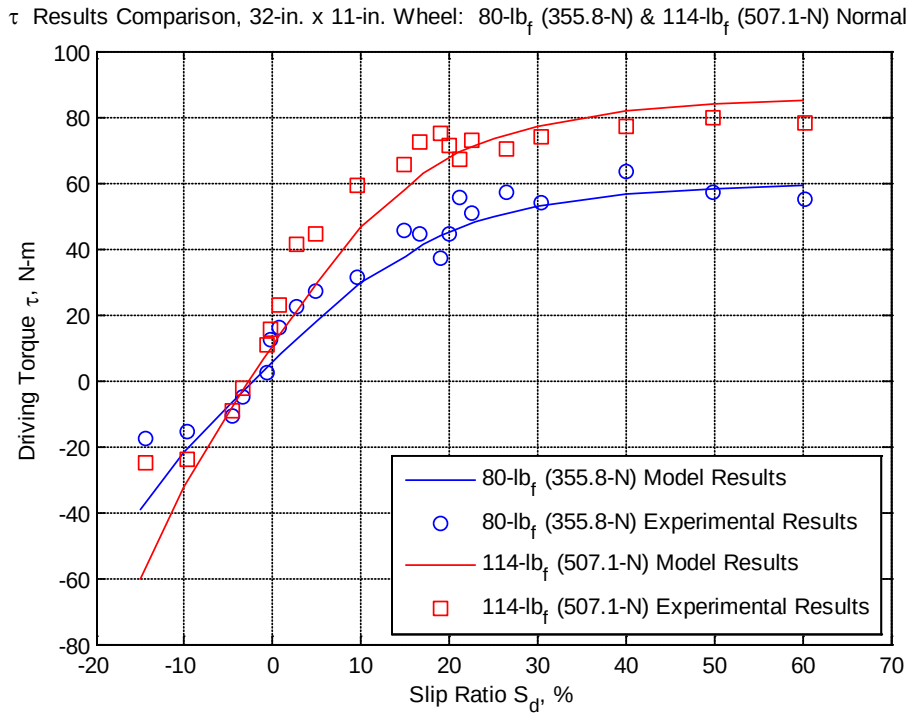

Figure 6-30. Modeling and experimental results for τ vs. S_d for 32-in. x 11-in. wheel at 355.8-N and 507.1-N normal loads.

The comparative results for the 20-in. x 7-in. wheel are shown in Figures 6-31 and 6-32.

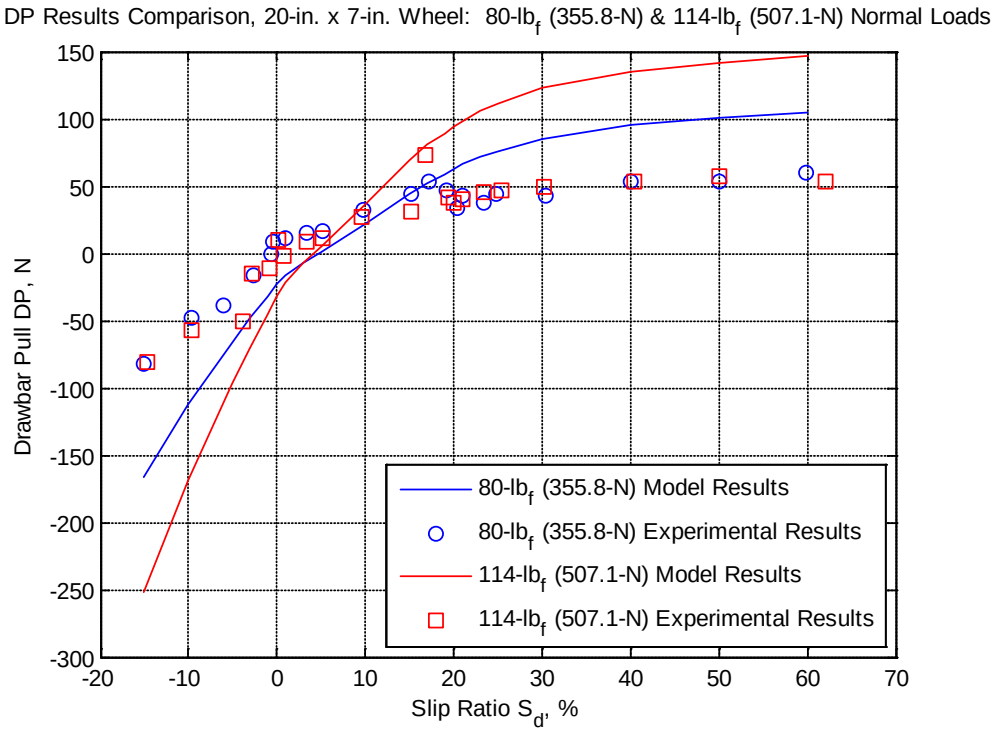

Figure 6-31. Modeling and experimental results for *DP* vs. S_d for 20-in. x 7-in. wheel at 355.8-N and 507.1-N normal loads.

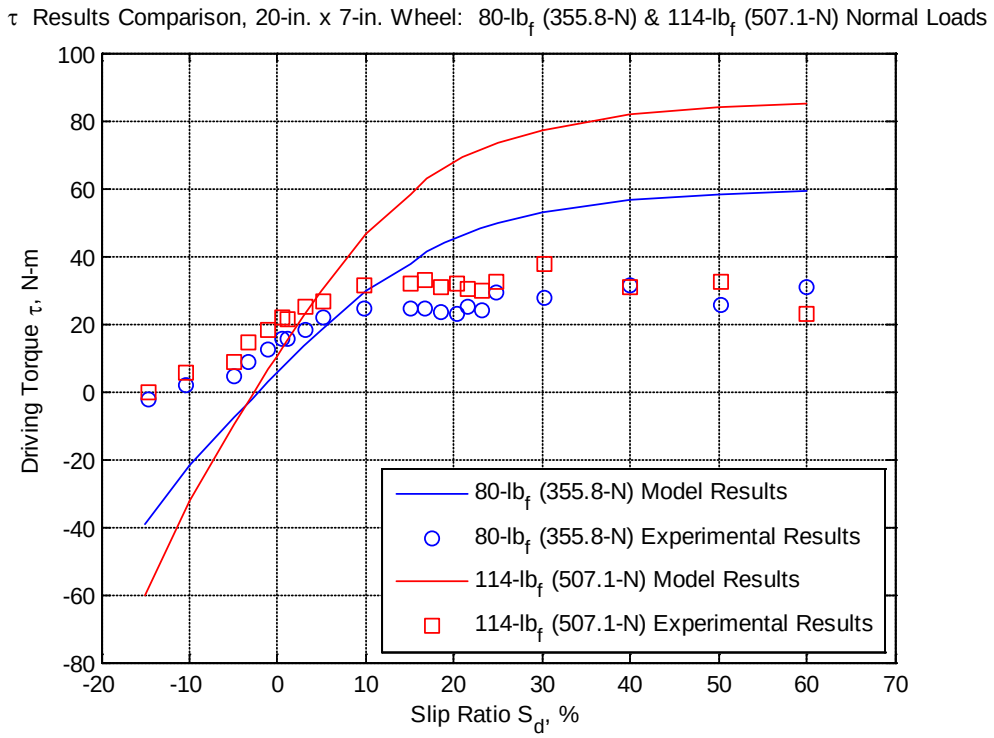

Figure 6-32. Modeling and experimental results for τ vs. S_d for 20-in. x 7-in. wheel at 355.8-N and 507.1-N normal loads.

From the plots provided in this section, one can easily observe that the simulation results for the 32-in. x 11 in. obtained using the rigid wheel model described in [18] correlated well with the experimental data, as shown in Figure 6-30 plot of torque versus slip ratio for the 80-lb_f (355.8-N) and 114-lb_f (507.1-N) normal loads. For the other two wheels the results did not correlate very well. Most of the modeling results for these two wheels conservatively estimated the wheel performance at lower slip ratios, and then overestimated the performance at the higher ranges of slip. Put another way, the experimental and modeling results showed consistency below +10% slip; however, at higher slip ratios there does not seem to be any pattern between the results. The variation in normal load partially explains this discrepancy. These results also indicate that further investigation into the exit angle's effects on drawbar pull, torque, and wheel sinkage is needed.

6.4 Modeling Results and Discussion: Conclusions

In this chapter, we presented simulation results using the semi-analytical model developed in [18] to predict the tractive performance of the three rigid wheels discussed in this study. The simulation results focused on benchmarking the wheel sinkage, drawbar pull, and driving torque for the three rigid wheels at different normal loads and slips. Finally, the simulation results were compared with data collected experimentally using the terramechanics rig at AVDL.

During the benchmarking of each performance parameter for the three wheels, the results indicated a qualitatively realistic behavior for the 20 in. x 7 in. wheel, with respect to the larger diameter wheels. Still, an important issue has been identified when comparing the results for the larger wheels: a more precise estimation of the exit angle needs to be investigated.

During the validation phase of the simulation model versus experimental data, the model predicted the wheel performance well at the desired normal loads only for the 32 in. x 11 in. wheel, while for the 32 in. x 7 in. and the 20 in. x 7 in. wheels the model was either too conservative (at negative slips), or overestimated the performance (at higher slips). This behavior reinforces the need to perform a more detailed analysis of the impact of the exit angle on the wheel performance, and in particular its accurate estimation on the Lunar soil simulant.

7. Supplemental Testing, Research Summary, and Future Work

This chapter includes additional tests performed and remarks pertaining to this study. First, wheel-slip tests using a fiber optic Doppler LIDAR system will be briefly covered. Next, concluding remarks on the work performed in this study will be presented, followed by recommendations for future work. Included in these recommendations are suggested modifications to the terramechanics rig.

7.1 Fiber Optic Doppler LIDAR Testing

The term "LIDAR" is an acronym for Light Detection and Ranging. LIDAR systems utilize light scatter to collect information about a specific target, such as velocity. In this study, LIDAR was used to measure the velocity difference (V_R), or relative velocity, between the translational motion of the terramechanics rig carriage and the tangential velocity of the slipping 32-in.-by-7-in. spiral wheel. This method for measuring wheel slip is provided in [22]. The objective was to find the angular wheel velocity at the zero-slip condition, in order to calculate the effective wheel radius. An example of an experimental setup of this system, mounted on a test vehicle, is shown in Figure 7-1.

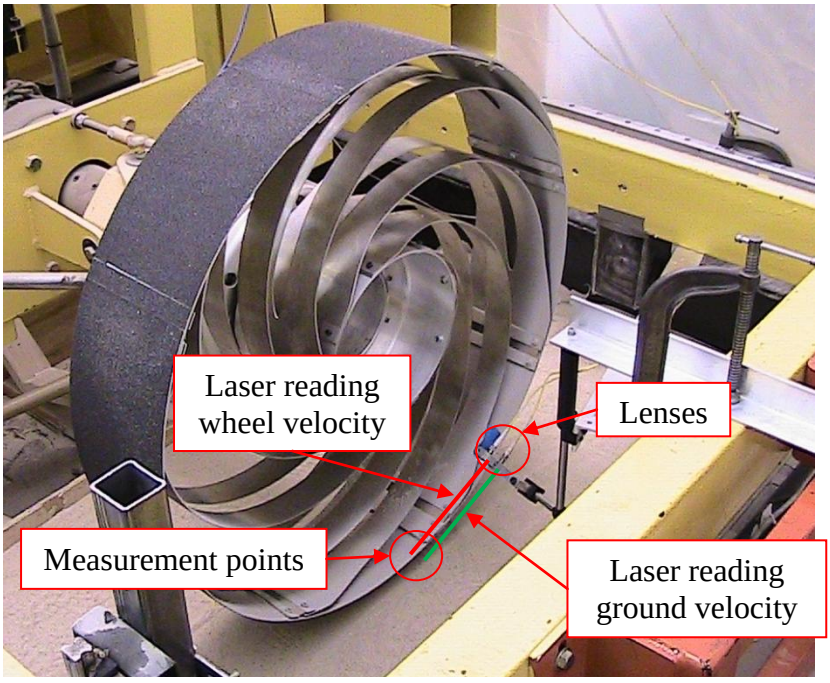

Figure 7-1. Diagram of LIDAR system.

The optical fibers (fiber-optic cables), which are commonly used in telecommunications, were attached to a pair of lenses used to focus on the points at which the two velocities were measured. The fibers work by detecting changes in the light frequency due to scatter caused by the target's motion [22]. This change in frequency is 580 kHz/mph $\left(\approx 1.298 \text{ x } 10^6 \text{ kHz / } \left(\text{m/s}\right)\right)$. In these experiments, the moving targets were the spinning wheel (directly below at its centerline) and the carriage's motion relative to the stationary terrain. The signal is very noisy, and, therefore, is recovered via post-experiment filtering methods.

The first step in the testing procedure was to prepare the soil via the method outlined in Chapter 3. One of the most important steps—if not the most important—was to perform a calibration run. In this step, the carriage was translated along the rig at the predetermined velocity of 5 cm/s while the fiber optics recorded the ground (carriage) speed so that the optics could be calibrated as to account for their angles relative to ground. Figure 7-2 shows a diagram of how these velocities were calibrated.

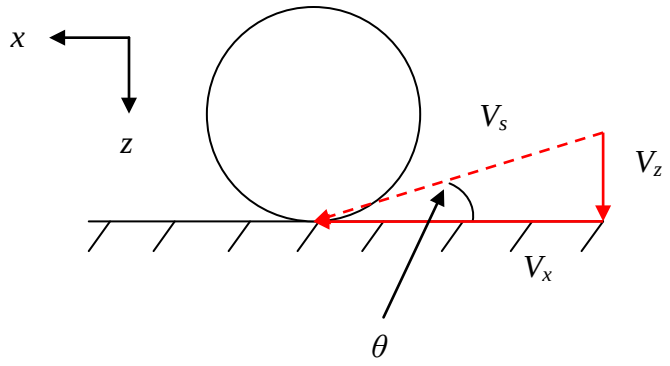

$V_s \equiv$ velocity "seen" by optical fibers.
$V_z \equiv$ velocity in z-direction (can be used to find terrain profile).
$V_x \equiv$ ground velocity, relative to which tangential wheel speed is compared.
$\theta \equiv$ angle optical laser makes with ground.

$$V_x = V_s \cos\theta$$

Figure 7-2. Velocity calibration diagram for fiber-optic cables.

This calibration was carried out for both optical lasers. Note that in order to calibrate the fiber optics, the wheel was removed from rig to avoid interfering with the calibration procedure. The next step was to position the wheel in line with its respective optical fiber. The third step

was to set the normal wheel load to 57 lb_f (253.5 N). After the load was set, the wheel speed was programmed, based on the assumed effective radius. From here, the test was performed. The end result of these tests was that using the known translational and angular velocities and the measured slip, the effective radius was found to be 16.00 inches (40.65 cm). The plot used to determine the correct effective radius can be found in Appendix A.

The Doppler LIDAR wheel slip measurement system proved to be an effective and accurate means of directly measuring wheel slip ratios. The effective radii of a wide variety of wheels/tires at various normal loads should be determined by utilizing this system. Similarly, wheel sinkage should also be measured by integrating the *z*-axis velocity [22].

7.2 Summary of Work

Before any testing could begin, a vast amount of work was dedicated to finalizing the terramechanics rig. At the beginning of this project, the terramechanics rig consisted of the soil bin, on top of which sat the incomplete carriage, and the carriage drive motor-gearbox combination. Part of the work dedicated to preparing the terramechanics rig for testing included completing the assembly of the terramechanics rig. This involved installing the wheel motor and gearbox, installing and calibrating the Kistler P650 wheel force measurement system, and installing/calibrating the G&L motion controllers, to name a few. A substantial amount of time and effort was also put into modifying the rig as to compensate for items and tasks unforeseen during the design process, such as designing, fabricating, and installing the original off-loading system that was needed to produce the light normal loads required by this study, along with developing a soil preparation method that can be executed in a timely fashion while yielding repeatable results. Included in the soil preparation development were the design, fabrication, and installation of the devices used during the procedure, such as the leveling blade and the method of moving the compaction roller along the sand using the Warn ATV winch. Currently, the terramechanics rig is fully-functional, and its capabilities are as discussed in Chapter 3.

The research presented in this study has provided an experimental perspective for understanding how specific wheel parameters affect the tractive performance of rigid wheels on Lunar soil simulant, and the findings could be extrapolated to other types of dry sand, as well. Three rigid wheels were used to examine how changing the contact width and decreasing the diameter cause the wheels' performance to deviate from that of a baseline wheel. Using the ring-

shaped spiral wheel, instead of a toroid-shaped tire, has allowed the use of a flexible wheel to determine the effect of increasing wheel diameter and contact patch length. Moreover, presenting the experimental results in the pull- and torque-map manner has provided means of predicting wheel performance versus two independent variables. The performance parameters can be anything, including - but not limited to - drawbar pull, driving torque, and sinkage.

Alongside the experimental results, modeling results have been obtained and discussed in this study. Per the results presented in Chapter 6, the model did not accurately predict the wheel performance at the desired normal loads for all simulation scenarios. This lead to the conclusion that more work in understanding the variables that affect a wheel's exit angle in various terrains is needed.

7.3 Recommendations for Future Work

Although the terramechanics rig at AVDL is fully operational, there are a few recommended modifications that should be considered before the next experimental study is performed. First and foremost, the method of setting and maintaining of the normal load should be changed. As previously mentioned in Chapter 5, maintaining a perfectly constant normal load throughout the duration of a test run is currently not possible in the low load range tested. The original concept behind the air-spring-and-tank system currently installed on the rig was that with the open air passages between the tank and the springs, the load would remain constant while allowing the wheel to traverse the terrain, regardless of any variations in the terrain profile. As observed experimentally and shown in Chapter 5, this was not the case.

An alternative idea to this method goes back to the original load-setting method: using free weights, pulleys, and linear rails to counterbalance the weight of the vertically-constrained carriage. One of the problems with this system was that there existed too much friction in the cables that connected the weights to the vertical carriage. To resolve this issue in a cost-effective manner, pulleys and straps commonly used on exercise equipment should be installed [23]. The straps usually consist of a Kevlar core coated in rubber, and utilizing this virtually friction-free system, the issue of maintaining a constant normal load should be resolved.

Another suggestion for the terramechanics rig is to make the winch used during the compaction process mobile, from side-to-side. This could be done by mounting the linear rails

on the soil bin door, and mounting linear bearings to the winch base. Making such a modification adds the ability to use the winch at any lateral position on the bin.

One area in which the terramechanics rig could also be improved is the measurement of the translational carriage velocity. Currently, there is no means of measuring the true velocity of the carriage. While the velocity is predetermined and manually entered into the controller code, having the ability to measure and record it would be very useful in accurately recording the testing conditions. To make the needed measurement and record the data, a string potentiometer could be utilized. Several companies design and manufacture a string potentiometer large enough to extend the length of the soil bin, such as UniMeasure [24]. The derivative of this device's position output could be taken with respect to time, from which the velocity would be found. The downside of using a string pot with such a long range is that the cable's weight could possibly cause it to sag under its own weight; however, this device is one of the more cost-effective options.

An alternative to using a string pot to measure the translational carriage velocity is a laser measurement device. The laser system shown above is used on a variety of applications, ranging from hoisting applications to measuring fill levels of high-volume materials. This particular device has a range of 0.1 to 30 m, and is accurate to within +/- 2.5 mm [25]. Many of these measurement tools have analog outputs, which is a requirement because the LMS data acquisition frontend has only analog inputs. One of the few downsides to using laser measurement systems is the cost of the systems. The price for these systems depends on measurement quality and range; however, such a high quality system could be worth the investment. The two measurement systems presented here are only a small fraction of the possible methods that can be used to measure the translational velocity of the terramechanics rig carriage.

An experimental recommendation for which the terramechanics rig could be used is to study and develop a relationship for accurately predicting the exit angle of wheels. Currently, there is the empirical formula discussed in Chapter 6 that is used to calculate the angle as a function of normal load and the coefficient *a*; however, after observing the wheel tests discussed in this study, it became clear that the exit angle of a wheel is a function of the slip ratio, as well. To perform such a task, one of the webcams should be mounted in an orientation such that it will view the wheel's being tested directly below the wheel centerline. The angle at which the

camera sits relative to the horizontal terrain surface should be noted so that any the projection can be accounted for during the determination of the exit angle.

A final recommendation for the terramechanics rig applies to all students who will operate it during the course of their research. Even though the tests were completed in a timely fashion, the learning curve for controlling the rig and recording the data proved rather steep. In an effort improve testing efficiency, as well as operator proficiency, it is highly recommended that all operators be enrolled in courses covering the PicPro controls programming and the LMS Test.Lab 8 software.

8. References

[1] Wong, J. Y. Theory of ground vehicles. New York: John Wiley, 2001.

[2] Wong, J. Y. "An Introduction to Terramechanics." Journal of Terramechanics 21.1 (1984): 5-17.

[3] Lee, Richard, and Corina Sandu. "Terrain Profile Modeling Using Stochastic Partial Differential Equations." International Journal of Vehicle Systems Modeling and Testing, Special Issue on "Terrain Topology: Measurement, Analysis, and Applications" (accepted May 2009).

[4] Asnani, Vivake, et al. "The development of wheels for the Lunar Roving Vehicle." Journal of Terramechanics 46 (2009): 89-103.

[5] Shmulevich, I., et al. "A New Field Single Wheel Tester." Journal of Terramechanics 33.3 (1996): 133-41.

[6] Murphy, N. R. and A. J. Green. "Effects of Test Techniques on Wheel Performance." Journal of Terramechanics 6 (1969): 37-52.

[7] Kawase, Y., et al., "An Indoor Traction Measurement System for Agricultural Tires." Journal of Terramechanics 43 (2006): 317-27.

[8] Shinone, H., et al. "Improvement of an Indoor Traction Measurement System Based on a Forced Slip Mechanism." 16th International Conference of the International Society for Terrain-Vehicle Systems. Turin, Italy. 2008. 138-43.

[9] Yahya, A. "UPM Indoor Tyre Traction Testing Facility." Journal of Terramechanics 44 (2007): 293-301.

[10] Freitag, D. R., et al. Performance Evaluation of Wheels for Lunar Roving Vehicles. U.S. Army Engineer Waterways Experiment Station Technical Report no. M-70-2. March 1970.

[11] Wang, Zhidan, and A. R. Reece. "The Performance of Free Rolling Rigid and Flexible Wheels on Sand." Journal of Terramechanics 21.4 (1984): 347-60.

[12] Sandu, Corina, et al. "Building an Infrastructure for Indoor Terramechanics Studies: The Development of a Terramechanics Rig at Virginia Tech." 16th International Conference of the International Society for Terrain-Vehicle Systems. Turin, Italy. 2008.

[13] Freitag, D. R., et al. "Wheels for Lunar Vehicles." Journal of Terramechanics 8.3 (1972): 89-105.

[14] Harnisch, Carsten, et al. "A New Tyre-Soil Interaction Model for Vehicle Simulation on Deformable Ground." Vehicle System Dynamics 43, Supplement (2005): 384-94.

[15] Reece, A. R. "Principles of Soil-Vehicle Mechanics." Proc. Instn. of Mech. Engrs. 2nd ser. 180.2A (1964a): 45-66.

[16] Wong, J. Y. "Data Processing Methodology in the Characterization of the Mechanical Properties of Terrain." Journal of Terramechanics 17.1 (1980): 13-41.

[17] Wong, J. Y., and A. R. Reece. "Prediction of Rigid Wheel Performance Based on the Analysis of Soil-Wheel Stresses Part I: Performance of Driven Rigid Wheels." Journal of Terramechanics 4.1 (1967): 81-98.

[18] Chan, Brendan J. "Development of an Off-Road Capable Tire Model for Vehicle Dynamics Simulation." Diss. Virginia Polytechnic Institute and State University, 2008.

[19] Oravec, Heather A. "Understanding Mechanical Behavior of Lunar Soils for the Study of Vehicle Mobility." Diss. Case Wester Reserve University, 2009.

[20] Worley, Marilyn E. "Experimental Study on the Mobility of Lightweight Vehicles on Sand." Thesis. Virginia Polytechnic Institute and State Unversity, 2007.

[21] Sandu, Corina. "Exit Angle Calculation." Personal interview. 16 June 2009.

[22] Holton, Carvel. "Overview of Doppler LIDAR System for Measuring Wheel Slip." Internal Engineering Communication. 7 Apr. – 12 Apr. 2009.

[23] "Buy at Fit-Senior.Com Kevlar Belt Kevlar Belting for weight machines." Fit-Senior Online Catalog. 15 June 2009 <http://www.fit-senior.com/acatalog/Kelvar_Belting_for_weight_machines_.html>.

[24] "HX Series Position Sensors." UniMeasure Linear and Rotary Transducers. 16 June 2009 <http://www.unimeasure.com/hx.htm>.

[25] "AR1000 laser distance sensors | Acuity laser measurement." Laser measurement sensors and scanners | Acuity homepage. 16 June 2009 <http://www.acuitylaser.com/AR1000/index.shtml>.

9. Appendices

A. Supplemental Test Data

Provided in this appendix are the experimental data and figures not shown in body of this document. These data include pressure-sinkage plots using Reece's equation, wheel-slip plots from tests using the Doppler LIDAR system briefly described in Chapter Seven, the data used to create the plots of the experimental results presented in Chapter Five, pressure pad testing results not discussed in Chapter Five, and modeling validation plots of drawbar pull and torque versus slip ratio from the validation section of Chapter Six.

Part I. Pressure-Sinkage Plots from Bevameter tests at NASA GRC

In order to find the values of n, k_c', and k_ϕ' for the GRC-1 Lunar soil simulant, bevameter tests were performed at NASA GRC using 7.6-, 10.2- and 19-cm diameter plates. Using the data from these tests and the processing method discussed in [16], the mean pressure-sinkage curves in Figures A-1 through A-3 were created.

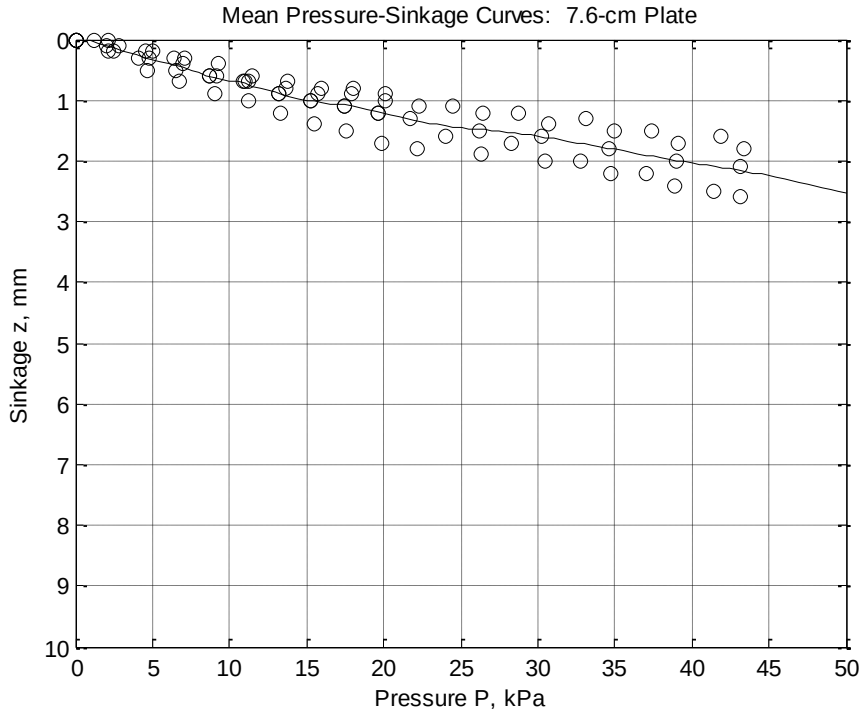

Figure A-1. Mean Pressure-Sinkage Curve for the 7.6-cm plate.

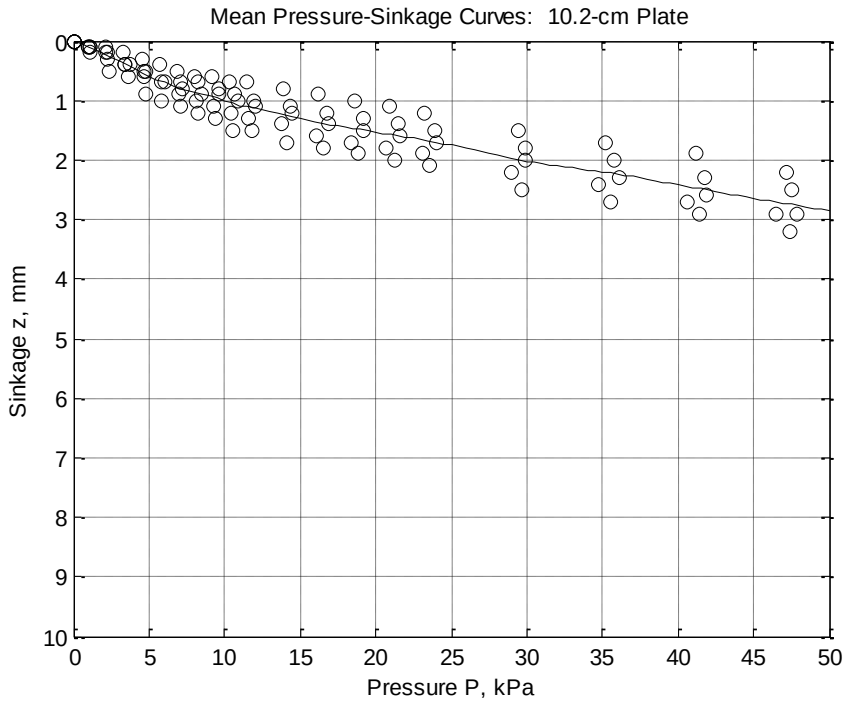

Figure A-2. Mean Pressure-Sinkage Curve for the 10.2-cm plate.

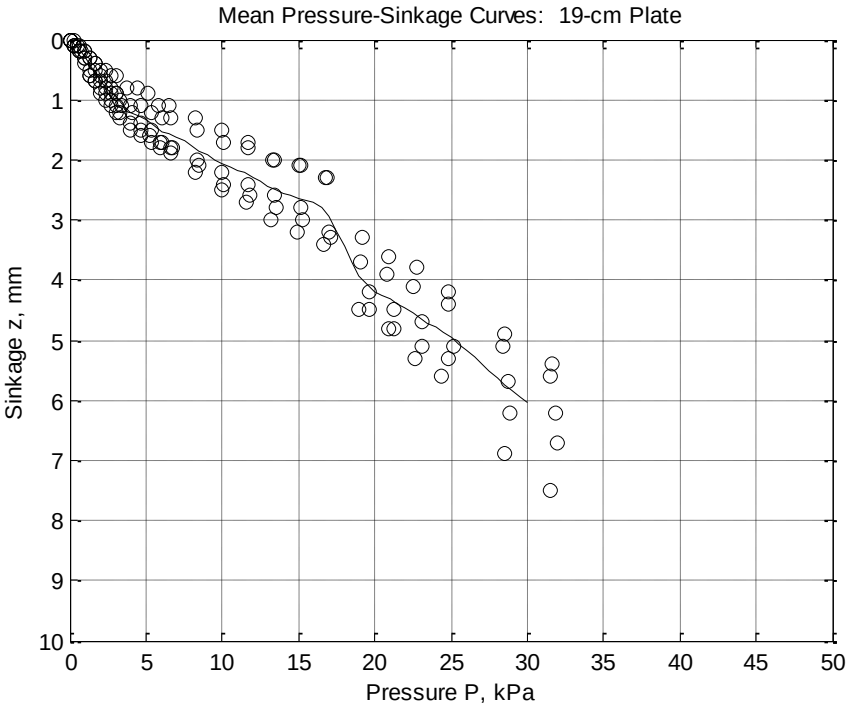

Figure A-3. Mean Pressure-Sinkage Curve for the 19-cm plate.

The Reece coefficients n, k_c', and k_ϕ' of the GRC-1 Lunar soil simulant, which were used as soil parameters in the wheel modeling, were equal to 1.2389, 33.452 kPa, and 768.19 kPa/m, respectively.

Part II. Doppler LIDAR Wheel Slip Test Results

The LIDAR wheel slip tests were utilized in an effort to determine the effective radius of the spiral wheel. The end result was that using the known translational and angular velocities and the measured slip, the effective radius was found to be 40.65 cm. The effective radius is normally calculated at the zero-slip point, where:

$$s_d = 1 - \frac{V_x}{\omega R_e} = 0 \Rightarrow R_e = \frac{V_x}{\omega} \tag{A.1}$$

The plot shown in Figure A-14 shows the measured slip value at a command slip of 5%, which was programmed using the original effective radius; however, this original effective radius was incorrect, and thus, the 40.65-cm radius was found to be the correct value.

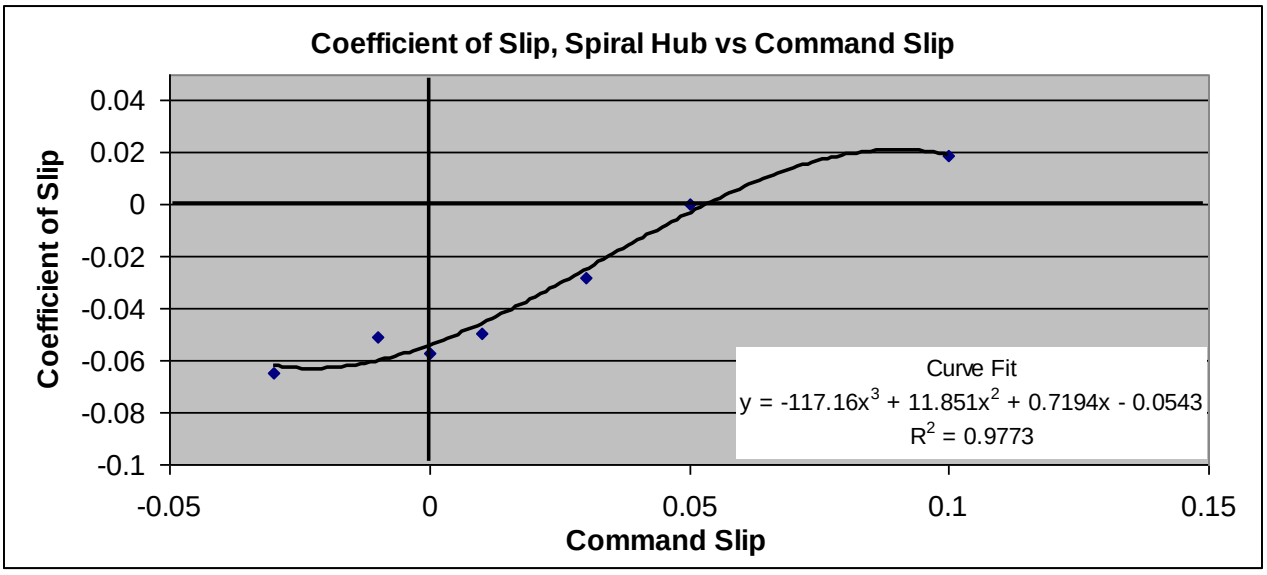

Figure A-4. Measured slip vs. command slip of the spiral wheel.

The LIDAR tests also resulted in the conclusion that the spiral wheel could not be tested at multiple slip ratios, due to resonances within the wheel.

Part III. Experimental Results of Drawbar Pull Tests

Shown in this section are data tables of the drawbar pull test results. These data were used to create the plots shown and discussed in Chapter Five.

Table A-1. Data from 32-in. x 7-in. rigid wheel tests sorted by desired normal loads.

Desired Fz	Slip (%)	Load (N)	Pull (N)	Torque (N-m)
57 lbf (253.5 N)	-14	260.5	-75.5	-13.7
	-10	241.5	-58.3	-9.6
	-4	255.9	-32.3	-3.8
	-3	297.0	-21.7	2.8
	-1	251.9	-1.0	13.1
	0	258.3	14.7	14.5
	1	248.6	18.8	16.6
	2	223.9	31.8	23.0
	6	214.8	49.1	26.7
	10	236.8	51.0	33.0
	15	141.2	44.4	24.7
	17	168.7	49.5	29.4
	19	177.1	52.5	32.4
	20	235.8	61.0	40.5
	21	178.7	61.4	35.6
	23	142.5	52.1	29.8
	25	207.3	60.3	40.4
	30	103.1	44.6	25.2
	40	99.0	42.8	24.8
	50	113.9	50.2	26.4
	60	69.6	38.4	18.3
70 lbf (311.4 N)	-15	286.7	-79	-14.3
	-10	294.2	-65	-11.0
	-5	242.7	-40	-7.6
	-3	320.1	-30	2.1
	-1	308.4	-4	9.8
	0	280.7	-11	10.4
	1	304.8	11	16.5
	3	263.1	31	22.9
	5	303.0	41	30.8
	11	263.2	56	36.5
	15	200.7	60	34.2

	17	242.7	57	38.8
	19	226.9	61	39.9
	20	187.2	52	33.0
	21	191.1	65	36.1
	23	208.3	61	37.2
	26	252.0	68	45.5
	30	228.3	73	45.5
	41	172.0	65	38.2
	50	232.5	73	49.9
	60	199.7	76	46.0
80 lbf (355.8 N)	-14	355	-101	-18.4
	-8	359	-73	-8.8
	-5	362	-44	-3.2
	-3	351	-17	4.2
	-1	306	10	17.4
	0	356	16	21.3
	1	287	23	19.9
	3	318	47	32.1
	5	354	56	39.1
	11	279	63	40.1
	14	247	62	41.9
	17	296	72	49.4
	19	171	51	30.1
	20	149	46	27.1
	21	118	42	23.4
	23	152	50	29.2
	26	136	52	28.7
	31	116	42	24.2
	40	219	70	43.9
	50	172	50	39.4
	61	179	38	42.1
114 lbf (507.1 N)	-15	510.0	-156.6	-26.5
	-8	496.6	-111.1	-20.2
	-4	510.0	-79.4	-12.2
	-3	511.2	-45.4	1.2
	-1	508.0	-6.1	17.2
	0	512.3	22.4	25.5
	1	504.7	19.5	29.5
	3	506.8	46.6	38.3
	5	453.3	65.4	41.3

	10	427.5	67.3	51.4
	15	390.5	74.1	53.8
	17	399.0	79.6	57.9
	18	411.0	71.9	60.1
	20	424.3	93.2	64.4
	21	335.8	92.3	56.1
	23	339.5	86.7	57.6
	26	361.7	87.8	61.4
	30	357.7	90.5	64.0
	41	340.8	95.7	64.8
	50	150.9	61.8	35.7
	61	207.2	82.6	48.0

Table A-2. Data from 32-in. x 11-in. rigid wheel tests sorted by desired normal loads.

Desired Fz	Slip (%)	Load (N)	Pull (N)	Torque (N-m)
57 lbf (253.5 N)	-14	256.6	-78.0	-17.5
	-10	261.9	-66.8	-17.7
	-5	256.9	-53.2	-10.3
	-3	261.6	-37.0	-3.8
	-1	252.7	-8.8	3.2
	0	257.5	-9.7	6.1
	1	254.9	17.1	10.9
	3	256.8	36.5	23.3
	5	259.1	50.3	28.1
	10	253.2	63.1	36.6
	15	236.0	68.5	39.8
	17	250.1	72.8	42.9
	19	240.9	68.7	41.0
	20	252.7	71.6	43.8
	21	215.9	67.3	40.2
	23	226.7	72.3	42.5
	26	231.9	79.3	43.9
	30	225.2	80.4	47.1
	40	173.4	77.1	39.9
	50	200.0	81.2	45.0
	60	201.4	92.6	48.1
70 lbf (311.4 N)	-14	303.8	-87.7	-18.1
	-10	307.9	-88.9	-20.1
	-5	306.8	-62.9	-11.3

	-3	310.4	-31.3	-3.7
	-1	311.7	-25.1	2.7
	0	304.3	-10.2	7.8
	1	308.7	3.5	12.9
	3	306.2	33.2	24.5
	5	314.8	39.7	30.8
	10	314.3	68.5	41.9
	15	299.9	77.8	47.5
	17	307.3	75.2	50.3
	19	295.7	77.7	48.6
	20	289.8	80.8	49.5
	21	202.1	75.1	38.9
	23	214.4	74.1	41.3
	25	249.6	80.3	47.3
	30	246.2	87.8	50.7
	40	218.1	84.0	48.1
	50	199.3	79.8	45.1
	60	177.5	86.0	43.1
80 lbf (355.8 N)	-14	312.6	-86.1	-17.7
	-10	257.8	-70.1	-15.3
	-5	332.0	-58.9	-10.8
	-3	306.5	-41.8	-4.8
	-1	355.3	-36.4	2.6
	0	340.6	-0.9	12.3
	1	345.5	7.4	15.9
	3	269.9	26.8	22.3
	5	278.9	45.3	27.3
	10	216.7	59.2	31.5
	15	297.1	71.9	45.4
	17	265.8	77.0	44.2
	19	204.1	67.0	37.0
	20	268.2	74.9	44.5
	21	327.2	89.2	55.3
	23	289.6	82.7	50.9
	26	303.2	93.1	56.9
	30	271.9	90.7	54.1
	40	306.8	99.3	63.5
	50	256.2	97.0	57.1
	60	236.3	102.2	55.1
114 lbf (507.1 N)	-15	472.6	-134.4	-25.2

	-10	504.3	-135.1	-24.1
	-5	509.9	-72.0	-9.0
	-3	507.1	-32.6	-2.5
	-1	505.0	-14.4	10.5
	0	503.2	-7.2	15.7
	1	503.8	10.2	23.1
	3	510.0	82.9	41.5
	5	508.8	50.1	44.4
	10	510.0	82.2	59.1
	15	460.4	93.4	65.5
	17	499.4	95.7	72.5
	19	478.2	116.0	75.2
	20	471.3	92.8	71.4
	21	412.2	106.6	67.1
	23	439.5	108.6	73.0
	26	409.9	106.9	70.2
	30	398.3	109.8	74.1
	40	371.0	120.7	77.3
	50	379.9	124.5	79.9
	60	343.9	133.2	78.4

Table A-3. Data from 20-in. x 7-in. rigid wheel tests sorted by desired normal loads.

Desired Fz	Slip (%)	Load (N)	Pull (N)	Torque (N-m)
57 lbf (253.5 N)	-15	218.7	-48.7	-1.5
	-10	263.8	-41.1	1.3
	-5	255.4	-23.8	3.8
	-3	259.8	-25.1	4.2
	-1	257.3	-4.5	8.7
	0	250.5	-0.4	9.2
	1	254.0	9.9	11.9
	3	215.0	17.0	11.8
	5	232.5	26.3	15.3
	10	258.6	28.3	19.4
	15	251.7	39.8	22.6
	17	214.8	37.2	20.3
	19	238.8	34.2	22.6
	20	218.2	39.3	21.2
	21	134.6	30.9	14.4
	23	133.2	36.4	15.1

	25	190.2	37.2	19.9
	30	174.0	34.9	19.3
	40	164.9	44.2	20.6
	50	157.0	47.3	20.4
	60	129.9	48.4	18.8
70 lbf (311.4 N)	-15	311.3	-69.5	-2.6
	-10	308.5	-40.4	5.4
	-4	312.6	-37.2	4.1
	-3	309.7	-21.5	6.4
	-1	306.7	2.7	10.1
	0	306.2	2.7	13.0
	1	302.9	9.6	13.0
	4	311.9	18.5	17.5
	5	314.7	26.0	20.1
	10	309.5	32.8	23.5
	15	289.7	40.2	24.8
	17	262.9	50.5	24.2
	19	252.6	44.2	24.2
	20	293.6	49.9	28.6
	21	272.0	48.1	26.4
	23	268.3	43.9	27.5
	25	272.2	42.4	27.3
	30	276.8	43.3	29.4
	40	224.2	49.8	27.2
	50	199.4	55.2	26.0
	60	241.0	61.9	32.1
80 lbf (355.8 N)	-15	360.7	-82.7	-2.1
	-10	358.3	-47.6	1.6
	-6	332.4	-38.2	4.4
	-3	363.8	-16.9	8.8
	-1	357.3	0.0	12.3
	0	354.0	7.9	15.3
	1	355.3	10.7	15.6
	3	356.0	15.2	18.2
	5	361.3	16.6	21.8
	10	343.0	31.7	24.5
	15	304.9	44.3	24.5
	17	325.4	53.1	24.6
	19	259.0	46.9	23.6
	20	250.9	34.1	22.6

	21	260.7	42.4	24.8
	23	245.1	36.9	23.8
	25	287.1	43.8	29.3
	30	258.7	42.7	27.8
	40	263.2	53.5	31.1
	50	200.4	53.4	25.3
	60	234.9	60.1	30.5
114 lbf (507.1 N)	-15	437.6	-80.8	-0.4
	-10	441.5	-57.0	5.4
	-4	506.0	-50.4	8.9
	-3	506.8	-15.5	14.7
	-1	509.4	-10.7	18.3
	0	488.2	9.7	21.9
	1	498.8	-2.3	21.3
	3	512.4	8.4	25.3
	5	475.1	11.7	26.8
	10	465.6	27.1	31.5
	15	416.5	30.3	31.9
	17	387.5	72.7	32.9
	19	335.7	41.3	30.8
	20	347.6	38.0	31.6
	21	330.9	39.5	30.0
	23	290.7	44.9	29.7
	25	322.9	46.4	32.2
	30	367.1	48.8	37.6
	40	261.9	53.0	30.9
	50	262.3	57.9	32.6
	62	151.7	53.6	22.7

Table A-4. Data from 32-in. x 7-in. spiral wheel tests sorted by desired normal loads.

Desired Fz	Slip (%)	Load (N)	Pull (N)	Torque (N-m)
57 lbf (253.5 N)	-15	254.3	-14.7	-3.0
	-10	254.7	-16.0	-3.6
	-5	254.9	-53.3	-12.5
	-3	254.8	-27.9	-6.7
	-1	254.4	-17.9	-1.4
	0	254.9	-27.6	-6.7
	1	253.4	-5.3	5.5

	3	239.8	39.2	23.3
	5	212.5	39.4	26.3
	10	223.5	62.1	34.5
	15	217.4	68.6	38.0
	17	200.1	79.4	41.2
	19	204.2	83.4	40.0
	20	218.6	82.7	43.0
	21	254.1	86.8	48.6
	23	255.7	130.4	55.1
	25	256.8	95.6	51.8
	30	254.7	91.8	55.6
	40	253.9	134.0	61.5
	50	250.1	117.0	61.7
	60	198.2	94.6	51.4

Part IV. Pressure Pad Testing Results

Static pressure pad tests were performed with the four test wheels at the four normal loads to understand the contact pressure distribution in this study. These tests were carried out by preparing the GRC-1 soil, lowering the wheel to the level of the terrain, and setting the normal load to the desired value using the method discussed in single-wheel testing portion Chapter Four. Shown in Figures A-5 through A-13 are the remaining screenshots of the wheel footprints of the three wheels for the 70-, 80-, and 114-lb_f (311.4-, 355.8-, and 507.1-N) normal loads. These pictures were not shown in Chapter Five.

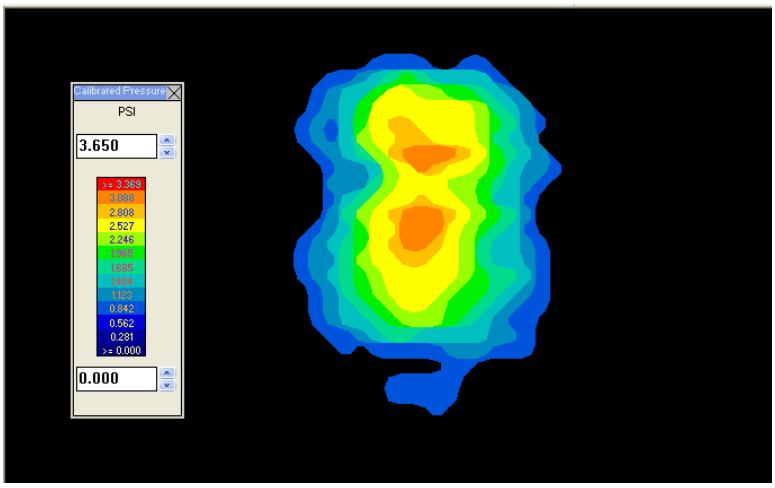

Figure A-5. 20-in. x 7-in. rigid wheel with 70-lb_f (311.4-N) normal load applied.

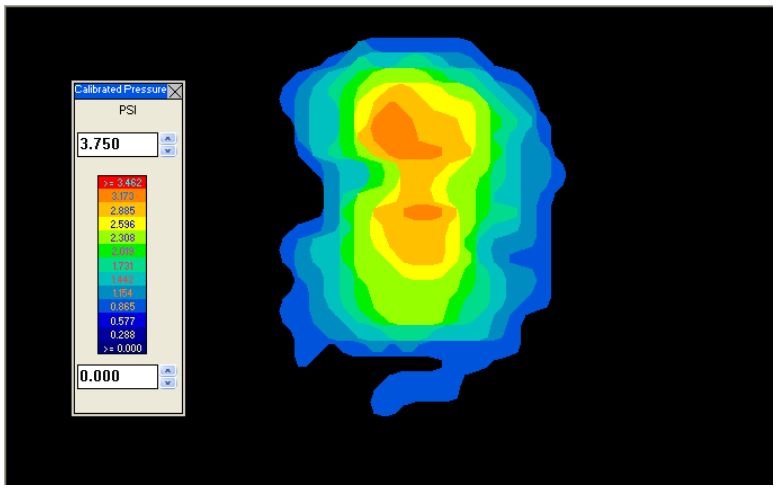

Figure A-6. 20-in. x 7-in. rigid wheel with 80-lb_f (355.8-N) normal load applied.

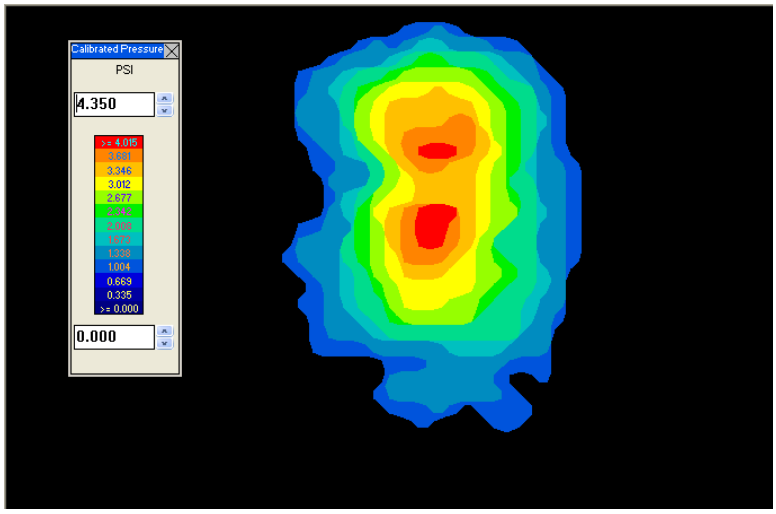

Figure A-7. 20-in. x 7-in. rigid wheel with 114-lb_f (507.1-N) normal load applied.

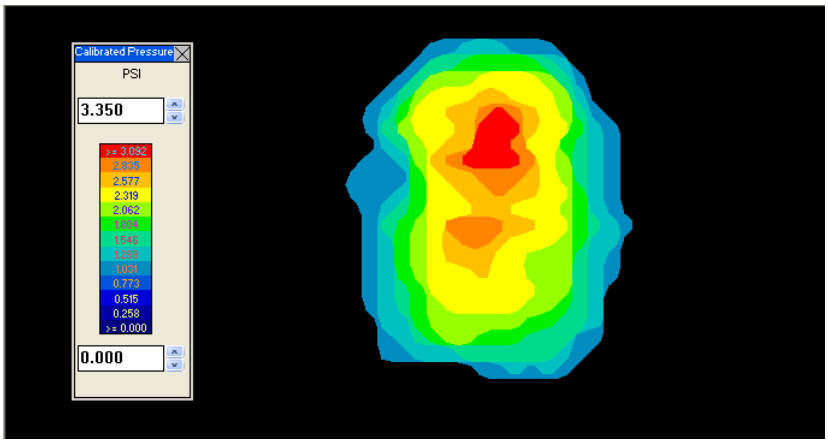

Figure A-8. 32-in. x 7-in. rigid wheel with 70-lb_f (311.4-N) normal load applied.

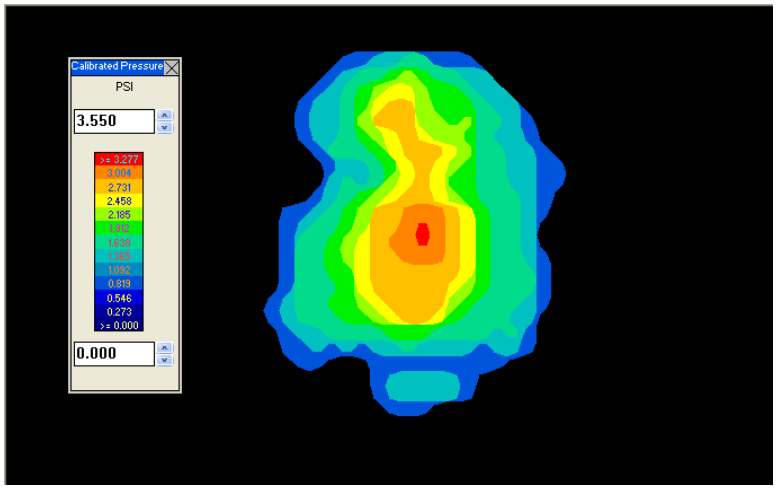

Figure A-9. 32-in. x 7-in. rigid wheel with 80-lb_f (355.8-N) normal load applied.

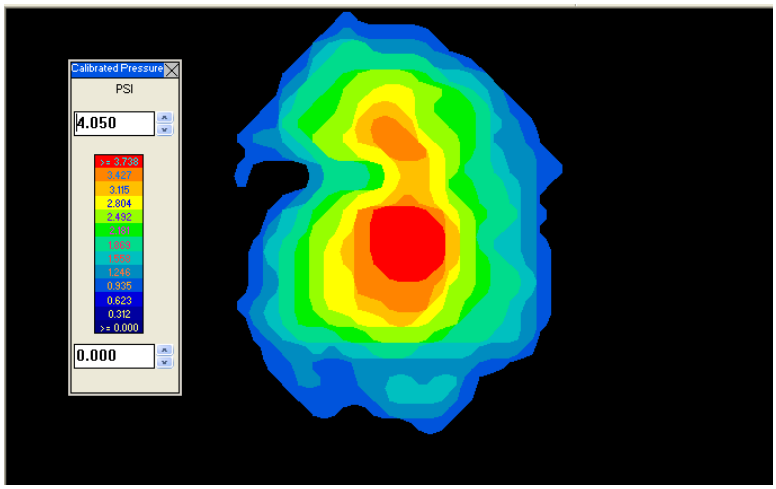

Figure A-10. 32-in. x 7-in. rigid wheel with 114-lb_f (507.1-N) normal load applied.

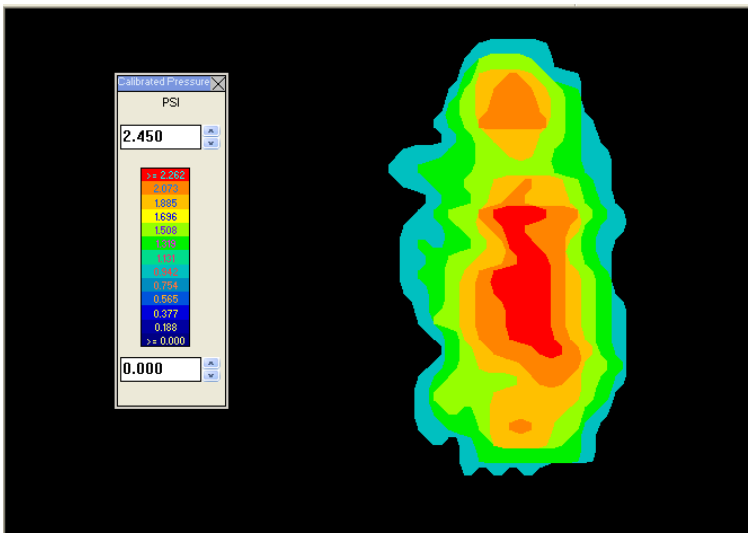

Figure A-11. 32-in. x 11-in. rigid wheel with 70-lb_f (311.4-N) normal load applied.

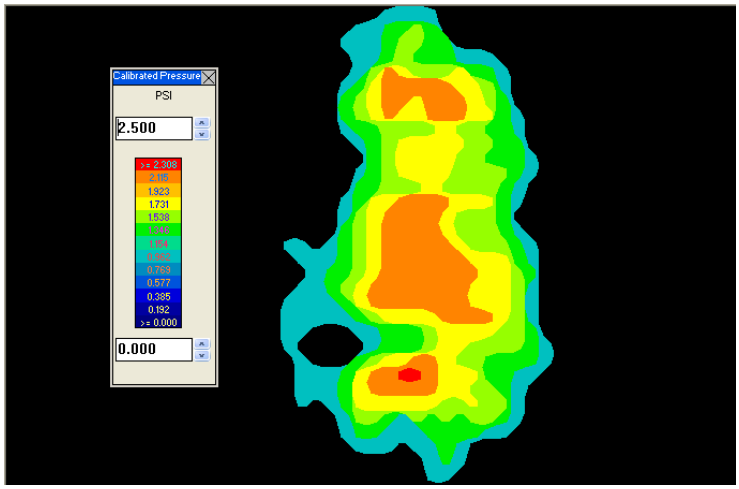

Figure A-12. 32-in. x 11-in. rigid wheel with 80-lb_f (355.8-N) normal load applied.

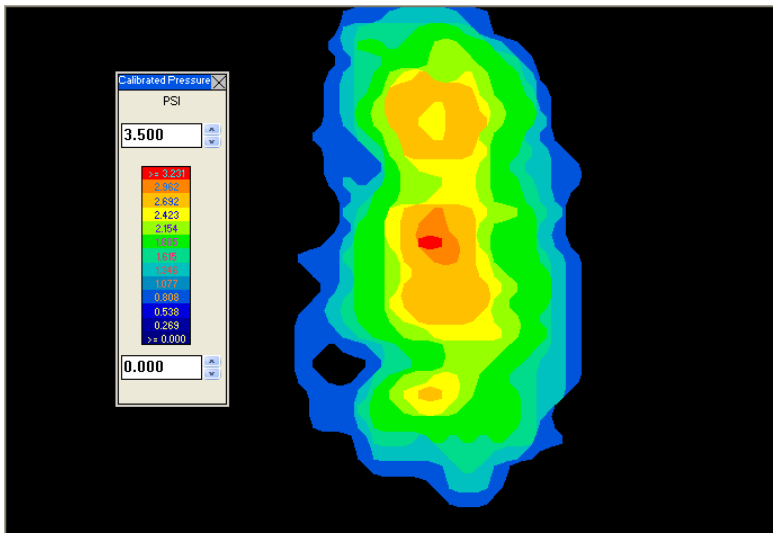

Figure A-13. 32-in. x 11-in. rigid wheel with 114-lb_f (507.1-N) normal load applied.

As expected the 20-in. x 7-in. wheel exerted the greatest contact pressure over its contact area and the 32-in. x 11-in. wheel exerted the smallest contact pressure over its contact area.

Part V. Validation Plots Excluded from Chapter Six

Shown in this section are plots used in the validation portion of Chapter Six. Figures A-14 through A-19 are plots from the modeling and experimental results of the drawbar pull and driving torque versus slip ratio.

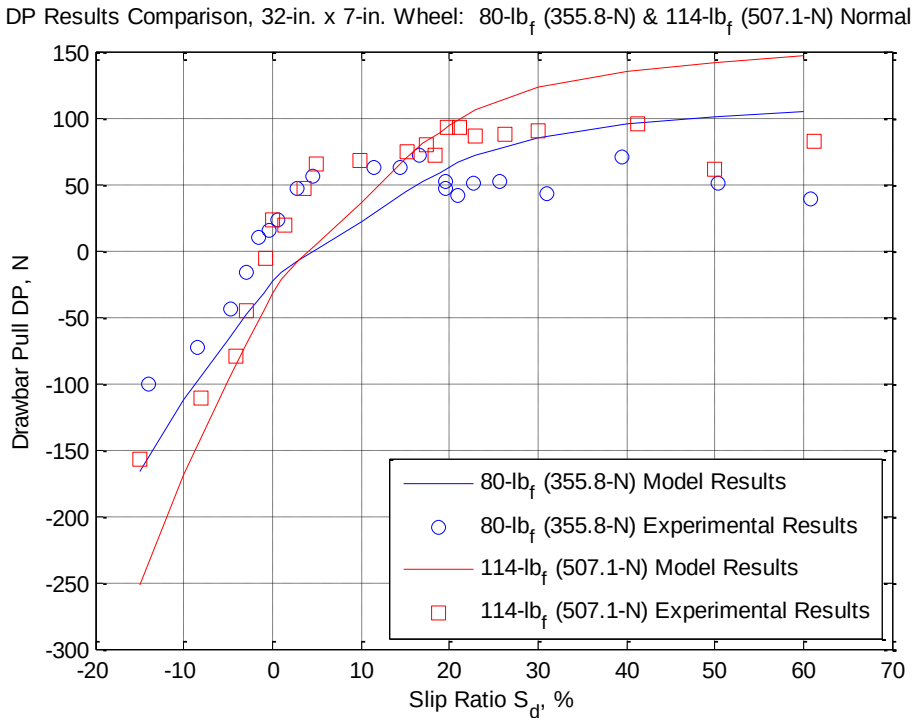

Figure A-14. Modeling and experimental results for *DP* vs. S_d for 32-in. x 7-in. wheel at 355.8-N and 507.1-N normal loads.

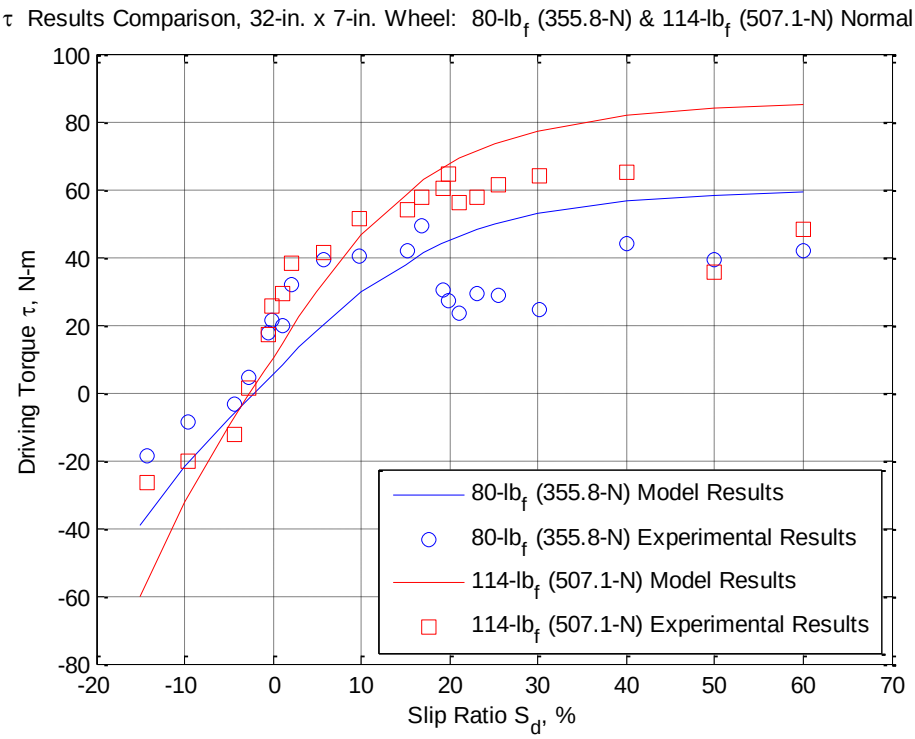

Figure A-15. Modeling and experimental results for τ vs. S_d for 32-in. x 7-in. wheel at 355.8-N and 507.1-N normal loads.

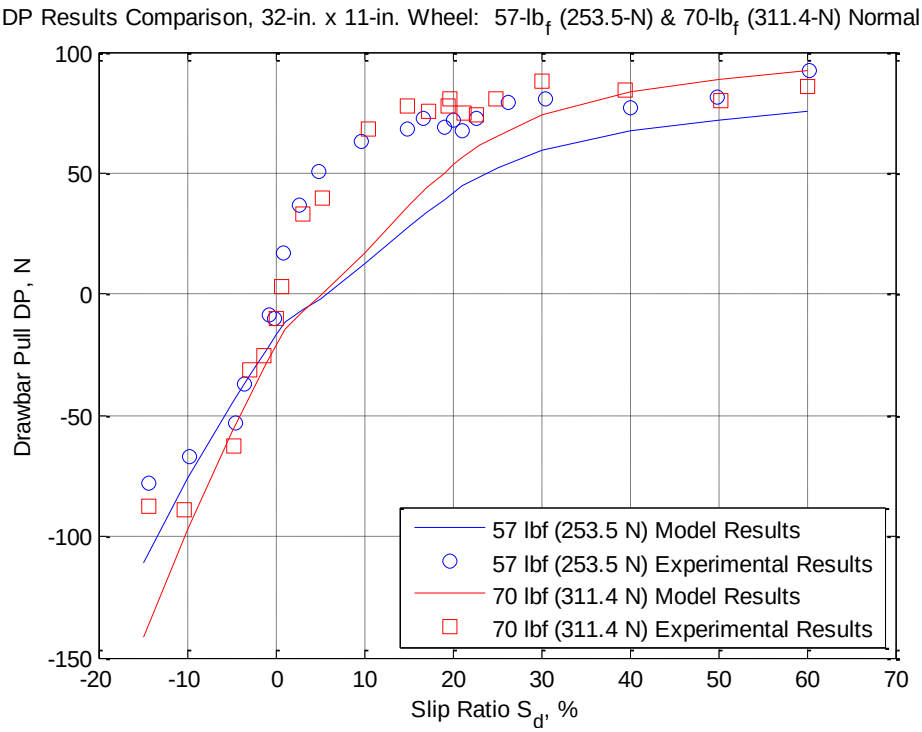

Figure A-16. Modeling and experimental results for *DP* vs. S_d for 32-in. x 11-in. wheel at 253.5-N and 311.4-N normal loads.

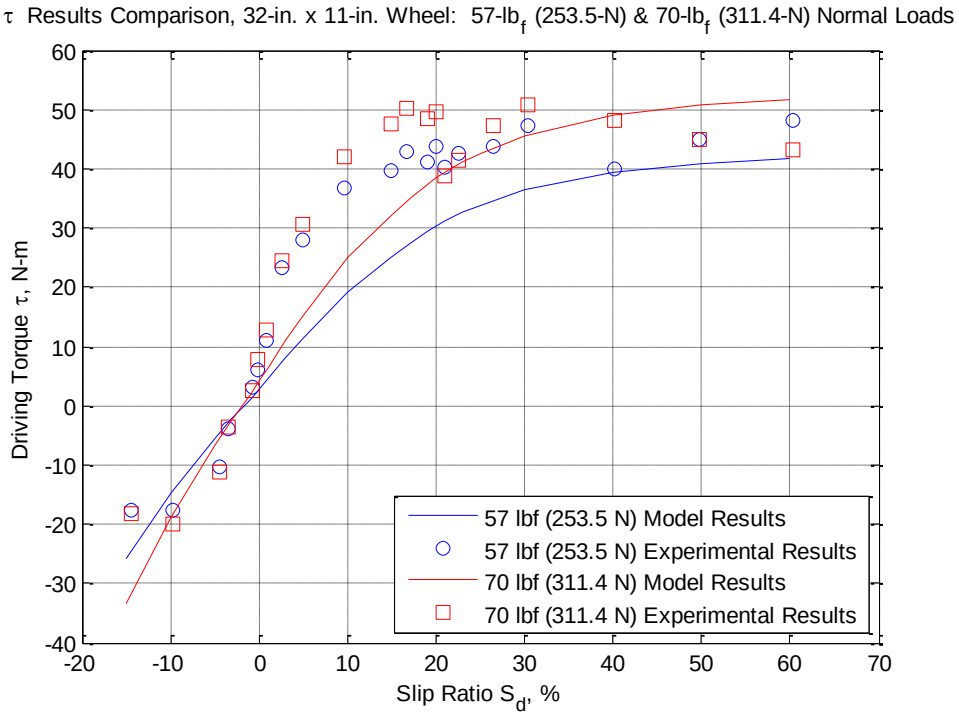

Figure A-17. Modeling and experimental results for τ vs. S_d for 32-in. x 11-in. wheel at 253.5-N and 311.4-N normal loads.

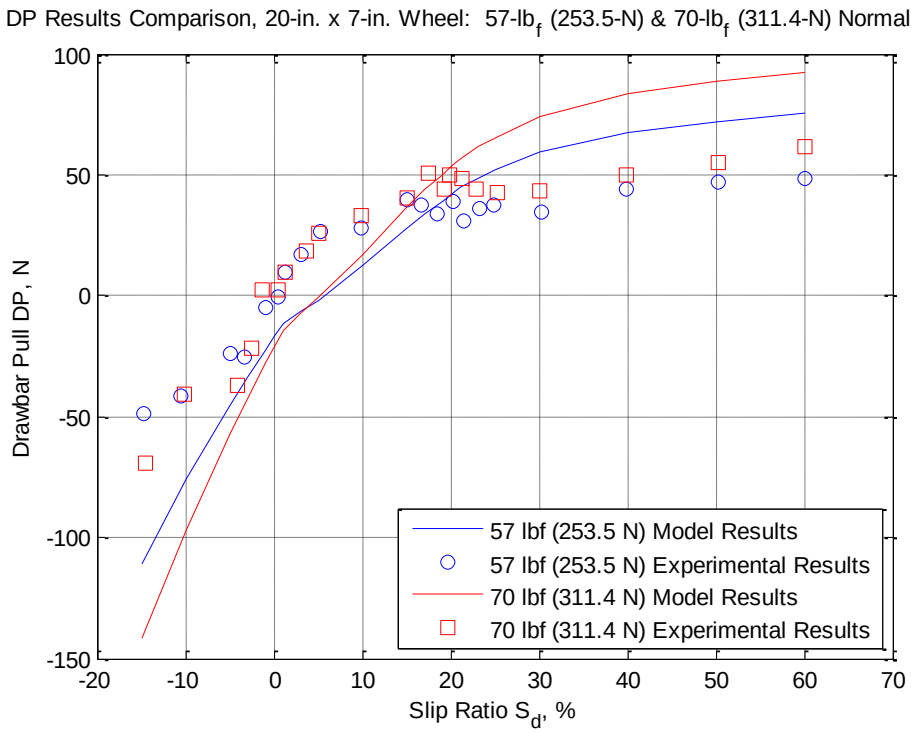

Figure A-18. Modeling and experimental results for *DP* vs. S_d for 20-in. x 7-in. wheel at 253.5-N and 311.4-N normal loads.

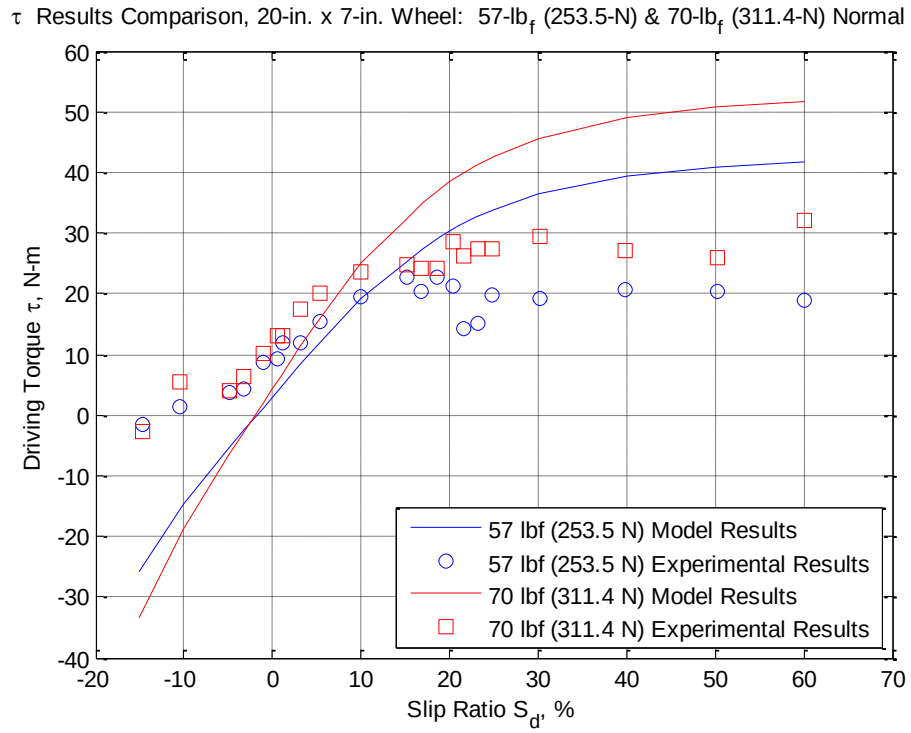

Figure A-19. Modeling and experimental results for τ vs. S_d for 20-in. x 7-in. wheel at 253.5-N and 311.4-N normal loads.

B. MATLAB Codes Utilized

Part I. Routine Used to Determine Reece Coefficients

The following MATLAB code was used to determine the Reece parameters used in [18], and the methodology is similar to that used in [19].

```
%Code to determine the Reece's equation coefficients n, k_c, and k_phi.
%Follows method similar to that used by Heather Oravec [19].
%Coeffcients will be used in Brendan Chan's tire model [18].

data=xlsread('Reece_Pressure_Sinkage.xls');

%Data in spreadsheet is labeled by plate # and test #.  The plate #'s
%correspond to the following diameters:
% a) 7.6-cm plate => 1
% b) 10.2-cm plate => 2
% c) 19-cm plate => 3
% Example:  Sinkage (z) of the 7.6-cm plate from test 1 is shown as "z11".

d1=0.076; %plate 1 diameter (m)
d2=0.102; %plate 2 diameter (m)
d3=0.190; %plate 3 diameter (m)

b1=d1/2;
b2=d2/2;
b3=d3/2;

%___7.6-cm Plate Data___
%Test 1
z11=data(:,1);f11=data(:,2);p11=data(:,3);

%Test 2
z12=data(:,4);f12=data(:,5);p12=data(:,6);

%Test 3
z13=data(:,7);f13=data(:,8);p13=data(:,9);

%Test 4
z14=data(:,10);f14=data(:,11);p14=data(:,12);

%Test 5
z15=data(:,13);f15=data(:,14);p15=data(:,15);

%___10.2-cm Plate___
%Test 1
z21=data(:,16);f21=data(:,17);p21=data(:,18);

%Test 2
z22=data(:,19);f22=data(:,20);p22=data(:,21);

%Test 3
```

```
z23=data(:,22);f23=data(:,23);p23=data(:,24);

%Test 4
z24=data(:,25);f24=data(:,26);p24=data(:,27);

%Test 5
z25=data(:,28);f25=data(:,29);p25=data(:,30);

%___19-cm Plate___
%Test 1
z31=data(:,31);f31=data(:,32);p31=data(:,33);

%Test 2
z32=data(:,34);f32=data(:,35);p32=data(:,36);

%Test 3
z33=data(:,37);f33=data(:,38);p33=data(:,39);

%Test 4
z34=data(:,40);f34=data(:,41);p34=data(:,42);

%Test 5
z35=data(:,43);f35=data(:,44);p35=data(:,45);

%Create a common and uniformly distributed pressure vector in order to
%determine the mean pressure-sinkage curve of all five data sets for each
%plate size.

%___7.6-cm Plate___
x1 = 0:.5:50; %new uniformly distributed pressure vector, kN/m^2
y11 = spline(p11,z11,x1); %new sinkage vector, m
y12 = spline(p12,z12,x1); %new sinkage vector, m
y13 = spline(p13,z13,x1); %new sinkage vector, m
y14 = spline(p14,z14,x1); %new sinkage vector, m
y15 = spline(p15,z15,x1); %new sinkage vector, m

%___10.2-cm Plate___
x2 = 0:.5:50; %new uniformly distributed pressure vector, kN/m^2
y21 = spline(p21,z21,x2); %new sinkage vector, m
y22 = spline(p22,z22,x2); %new sinkage vector, m
y23 = spline(p23,z23,x2); %new sinkage vector, m
y24 = spline(p24,z24,x2); %new sinkage vector, m
y25 = spline(p25,z25,x2); %new sinkage vector, m

%___19-cm Plate___
x3 = 0:.5:30; %new uniformly distributed pressure vector, kN/m^2
y31 = spline(p31,z31,x3); %new sinkage vector, m
y32 = spline(p32,z32,x3); %new sinkage vector, m
y33 = spline(p33,z33,x3); %new sinkage vector, m
y34 = spline(p34,z34,x3); %new sinkage vector, m
y35 = spline(p35,z35,x3); %new sinkage vector, m

%Find the average plate sinkage for each size from the overall test series.
```

```
%___7.6-cm Plate___
plate1 = [y11; y12; y13; y14; y15];
z_avg1 = mean(plate1); %mean of the sinkage vectors
stdev1 = std(plate1); %standard deviation of the sinkage vectors
figure(1)
plot(p11,z11*1000,'ko',p12,z12*1000,'ko',p13,z13*1000,'ko',p14,z14*1000,'ko',
p15,z15*1000,'ko'); hold on
plot(x1,z_avg1*1000,'k-'); hold off
title('Mean Pressure-Sinkage Curves:  7.6-cm Plate');
xlabel('Pressure P, kPa');
ylabel('Sinkage z, mm');
grid on
axis([0 50 0 10])
set(gca,'YDir','reverse')

%___10.2-cm Plate___
plate2 = [y21; y22; y23; y24; y25];
z_avg2 = mean(plate2); %mean of the sinkage vectors
stdev2 = std(plate2); %standard deviation of the sinkage vectors
figure(2)
plot(p21,z21*1000,'ko',p22,z22*1000,'ko',p23,z23*1000,'ko',p24,z24*1000,'ko',
p25,z25*1000,'ko'); hold on
plot(x2,z_avg2*1000,'k-'); hold off
title('Mean Pressure-Sinkage Curves:  10.2-cm Plate');
xlabel('Pressure P, kPa');
ylabel('Sinkage z, mm');
grid on
axis([0 50 0 10])
set(gca,'YDir','reverse')

%___19-cm Plate___
plate3 = [y31; y32; y33; y34; y35];
z_avg3 = mean(plate3); %mean of the sinkage vectors
stdev3 = std(plate3); %standard deviation of the sinkage vectors
figure(3)
plot(p31,z31*1000,'ko',p32,z32*1000,'ko',p33,z33*1000,'ko',p34,z34*1000,'ko',
p35,z35*1000,'ko'); hold on
plot(x3,z_avg3*1000,'k-'); hold off
title('Mean Pressure-Sinkage Curves:  19-cm Plate');
xlabel('Pressure P, kPa');
ylabel('Sinkage z, mm');
grid on
axis([0 50 0 10])
set(gca,'YDir','reverse')

%---Use the mean pressure-sinkage data to find the Reece's parameters.---

%___7.6-cm Plate___
z_avg1_edit = z_avg1(4:end);
x1_edit = x1(4:end);

%___10.2-cm Plate___
z_avg2_edit = z_avg2(2:end);
x2_edit = x2(2:end);
```

```
%___19-cm Plate___
z_avg3_edit = z_avg3(2:end);
x3_edit = x3(2:end);

%Find exponent of deformation, n.
%___7.6-cm Plate___
num1=sum(x1_edit.^2).*sum(x1_edit.^2.*log(x1_edit).*log(z_avg1_edit./b1))-
sum(x1_edit.^2.*log(x1_edit)).*sum(x1_edit.^2.*log(z_avg1_edit./b1));
den1=sum(x1_edit.^2).*sum(x1_edit.^2.*(log(z_avg1_edit./b1)).^2)-
(sum(x1_edit.^2.*log(z_avg1_edit./b1))).^2;
n1=num1/den1;

%___10.2-cm Plate___
num2=sum(x2_edit.^2).*sum(x2_edit.^2.*log(x2_edit).*log(z_avg2_edit./b2))-
sum(x2_edit.^2.*log(x2_edit)).*sum(x2_edit.^2.*log(z_avg2_edit./b2));
den2=sum(x2_edit.^2).*sum(x2_edit.^2.*(log(z_avg2_edit./b2)).^2)-
(sum(x2_edit.^2.*log(z_avg2_edit./b2))).^2;
n2=num2/den2;

%___19-cm Plate___
num3=sum(x3_edit.^2).*sum(x3_edit.^2.*log(x3_edit).*log(z_avg3_edit./b3))-
sum(x3_edit.^2.*log(x3_edit)).*sum(x3_edit.^2.*log(z_avg3_edit./b3));
den3=sum(x3_edit.^2).*sum(x3_edit.^2.*(log(z_avg3_edit./b3)).^2)-
(sum(x3_edit.^2.*log(z_avg3_edit./b3))).^2;
n3=num3/den3;

n_avg=(n1+n2+n3)/3

%Find k_eq' for each plate.

%___7.6-cm Plate___
ln_keq1=(sum(x1_edit.^2.*log(x1_edit))-
n_avg.*sum(x1_edit.^2.*log(z_avg1_edit./b1)))/sum(x1_edit.^2);

%___10.2-cm Plate___
ln_keq2=(sum(x2_edit.^2.*log(x2_edit))-
n_avg.*sum(x2_edit.^2.*log(z_avg2_edit./b2)))/sum(x2_edit.^2);

%___19-cm Plate___
ln_keq3=(sum(x3_edit.^2.*log(x3_edit))-
n_avg.*sum(x3_edit.^2.*log(z_avg3_edit./b3)))/sum(x3_edit.^2);

keq1=exp(ln_keq1);
keq2=exp(ln_keq2);
keq3=exp(ln_keq3);

%To find k_c" and k_phi", use a least-squares matrix operation.
A=[1/b1 1; 1/b2 1; 1/b3 1];
b=[keq1; keq2; keq3];
x=A\b;

kc_2prime = x(1)
kphi_2prime = x(2)
```

```
%Check the fit using Reece's pressure-sinkage equation.
p1_fit=(kc_2prime+(b1*kphi_2prime)).*(z_avg1./b1).^n_avg;
p2_fit=(kc_2prime+(b2*kphi_2prime)).*(z_avg2./b2).^n_avg;
p3_fit=(kc_2prime+(b3*kphi_2prime)).*(z_avg3./b3).^n_avg;

%Plot of original pressure-sinkage data vs curve-fit.
figure(4)
plot(p11,z11*1000,'bo',p12,z12*1000,'bo',p13,z13*1000,'bo',p14,z14*1000,'bo',
p15,z15*1000,'bo',p1_fit,z_avg1*1000,'b-');
hold on
plot(p21,z21*1000,'r^',p22,z22*1000,'r^',p23,z23*1000,'r^',p24,z24*1000,'r^',
p25,z25*1000,'r^',p2_fit,z_avg2*1000,'r--');
hold on
plot(p31,z31*1000,'ks',p32,z32*1000,'ks',p33,z33*1000,'ks',p34,z34*1000,'ks',
p35,z35*1000,'ks',p3_fit,z_avg3*1000,'k.');
hold on
title('Experimental Pressure-Sinkage Data vs. Reece Curve-Fit')
xlabel('Pressure P, kPa');
ylabel('Sinkage z, mm');
axis([0 50 0 10]);
grid on
set(gca,'YDir','reverse')
gtext(['n = ',num2str(n_avg),', k_c" = ',num2str(kc_2prime) ' kPa',',
k_p_h_i" = ',num2str(kphi_2prime),' kPa/m'])
```

Part II. Routine Used in Wheel Model

The following code was used to create the modeling outputs in Chapter Six and was created by Chan [18]. Note that only the rigid wheel portion was used in this study.

```
% Brendan Chan 2008
% create video of the tire with varying normal force
% function [Fx,Fy,Mx,Mz] = offroadtire(Fz,gammat,sd,alphac,omega)

%-------------------------------------------------------------------------

% Input wheel parameters

%-------------------------------------------------------------------------

% Soil parameters
% Sand
phi=deg2rad(33.82);
gammas=16382.7; %[N/m^3] ~> soil unit weight from (Soil Density)*(9.81
m/s^2).
kc=33.4520; %[kPa] ~> cohesive modulus of soil deformation.
kphi=768.1899; %[kPa/m] ~> friction modulus of soil deformation.
n=1.2389; %[unitless] ~> exponent of soil deformation.
c=-0.14; %[kPa] ~> coefficient of soil/wheel cohesion.
Kx=0.0237; %[m] ~> coefficient of longitudinal soil slip.
Ky=Kx; %[cm] ~> coefficient of lateral soil slip.
```

```
% ----------------------- Program starts here --------------------------
% inline functions
% N factors
funNq=@(x) (exp(2.*(3.*pi/4-x/2).*tan(x)))/(2.*cos(pi/4+x/2).^2);
funNc=@(x) cot(x).*(((exp(2.*(3.*pi/4-x/2).*tan(x)))/(2.*cos(pi/4+x/2).^2))-
1);
funNg=@(x) 2.*(((exp(2.*(3.*pi/4-
x/2).*tan(x)))/(2.*cos(pi/4+x/2).^2))+1).*tan(x);

% Tire stiffness functions
funcubic =@(coeff,x) coeff(1).*x.^3+coeff(2).*x.^2+coeff(3).*x+coeff(4);
funquad =@(coeff,x) coeff(1).*x.^2+coeff(2).*x+coeff(3);
funkz=@(coeff,x) coeff(1)+(coeff(2)-
coeff(1)).*(sech(coeff(3).*(abs(tan(x))./(1-abs(tan(x))))));
funsat=@(coeff,x) coeff(1).*(1-exp(-coeff(2).*x));

% Calculate tire curvature as a function of longitudinal coordinate
zcurve=@(arg,coeff) -coeff(2).*(cos(coeff(1))-cos(asin(sin(coeff(1))-
arg./coeff(2))));

% Limits the slip angle and slip ratio
sd=min(abs(sd),0.99).*sign(sd);
alphac=min(abs(alphac),pi/4).*sign(alphac);

% Initial calculation to determine
% Calculate the carcass limit pressure
pc=beta*(alp*p_i+ccons)/(2*Ru^2)*b;

% Calculate initial entry angle
[thetae,costval] = fminsearch(@(x)
thetaefun(x,inc,thetab,Ru,b,kc,kphi,gammas,c,n,Kx,Ky,phi,sd,alphac,Fz),deg2ra
d(10),optimset('Display','off'));
theta=thetae:-inc:thetab;

% Calculate initial Radial Stress
sigmaval=sigman(theta,thetab,thetae,Ru,b,kc,kphi,c,gammas,n,phi,sd);

% Decide whether rigid wheel tire model or flexible ring tire model is to be
used
% if pc<max(sigmaval),
    % use flexible tire model
    % Needs the functions
    % thetaefun2.m
    % sigmant.m
    % tauxt.m
    % tauyt.m
    % calculate the entry angle

    % Flexible tire formulation
    % Vertical Stiffness modeling
%     initdel=Fz/Kz0;
%     Cz1=-funcubic(Cz1prm,initdel) ;
%     Cz2=funquad(Cz2prm,initdel) ;
%     Kz=funkz([Cz1,1,Cz2],alphac).*Kz0;
%
```

```
%     % Rolling Radius
%     Rl=Ru-Fz./Kz;
%
%     % Calculate the carcass limit pressure
%     pc=beta*(alp*p_i+ccons)/(2*Ru^2)*b;
%
%     % Calculates thetae initially
%     a=tan(pi./4-phi./2);
%     thetaes=abs(atan2(abs(-(-(0.1e1 + sqrt((-2 .* a .^ 2 .* sd + a .^ 2 .*
sd .^ 2 - 2 .* a .^ 4 .* sd + a .^ 4 .* sd .^ 2 + a .^ 4))) ./ (1 + a .^ 2) +
0.1e1) ./ a ./ (-1 + sd)), abs(-(0.1e1 + sqrt((-2 .* a .^ 2 .* sd + a .^ 2 .*
sd .^ 2 - 2 .* a .^ 4 .* sd + a .^ 4 .* sd .^ 2 + a .^ 4))) ./ (1 + a .^ 2)
./ (-1 + sd))));
%
%     % limits thetan to 1/3 of phi, based on the retaining wall problem
%     if thetaes>0,
%         thetaes=min(abs(thetaes),(1/3).*phi).*sign(thetaes);
%     else
%         thetaes=min(abs(thetaes),0).*sign(thetaes);
%     end
%
%     % Calculate entry angle
%     [thetae,costval] = fminsearch(@(x)
thetaefun2(x,inc,thetab,Ru,b,kc,kphi,gammas,c,n,Kx,Ky,phi,sd,alphac,Fz,beta,F
z/Kz,ccons,alp,p_i,omega,cdamp,pc),thetaes+deg2rad(10),optimset('Display','of
f'));
%
%     % Set up the angle vector
%     theta=thetae:-inc:thetab;
%
%     %sweeps the angles to calculate the radial shape
%     [Reff] = radialdef(Ru,beta,Fz./Kz,ccons,alp,p_i,omega,cdamp,theta-
thetaes);
%
%     % Radial Stress Calculations
%
sigmaval=sigmant(theta,thetab,thetae,Reff,b,kc,kphi,c,gammas,n,phi,sd,pc);
%
%     % Maximum stress envelope
%
taum=(c+sigmant(theta,thetab,thetae,Reff,b,kc,kphi,c,gammas,n,phi,sd,pc).*tan
(phi));
%     taum(1)=0;
%     taum(end)=0;
%
%     % Lateral shear stress
%
tausy=tauyt(theta,thetab,thetae,Reff,b,kc,kphi,gammas,c,n,Kx,Ky,phi,sd,alphac
,pc);
%
%     % Longitudinal shear stress
%
tausx=tauxt(theta,thetab,thetae,Reff,b,kc,kphi,gammas,c,n,Kx,Ky,phi,sd,alphac
,pc);
%
%     % Calculate wheel vertical load
%     if omega==0,
```

```
%          W = - b.*(trapz(Reff.*sigmaval.*cos(theta)).*inc);
%      else
%          W = - b.*( trapz(Reff.*tausx.*sin(theta)).*inc +
trapz(Reff.*sigmaval.*cos(theta)).*inc);
%      end
%
%      % Longitudinal Force
%      if omega==0,
%          if sd==0,
%              Fx= 0;
%          else
%              Fx= b.*( trapz(Reff.*tausx.*cos(theta)).*inc -
trapz(Reff.*sigmaval.*sin(theta)).*inc);
%          end
%      else
%              Fx= b.*( trapz(Reff.*tausx.*cos(theta)).*inc -
trapz(Reff.*sigmaval.*sin(theta)).*inc);
%      end
%
%      if abs(alphac)<1e-8,
%          % Lateral shear stress force
%          Fy=0;
%          Fycp=0;
%          FBD=0;
%      else
%          % Lateral shear stress force
%          Fycp= b.*( trapz(Reff.*tausy).*inc );
%
%          % Calculate the bulldozing force
%          if abs(thetae)<1e-6,
%              % if sinkage is zero, the bulldozing force is zero
%              FBD=0;
%          else
%              xin=inc:inc:2*Ru*sin(thetae);
%              [Ref] =
radialdef(Ru,beta,Fz./Kz,ccons,alp,p_i,omega,cdamp,asin(sin(thetae)-
xin./Ru));
%              m=tan(pi/4+phi/2);
%              qm=(gammas.*Ref.*(2.*thetae-
sin(2.*thetae)).*xin.*tan(alphac))./(m.*zcurve(xin,[thetae,Ref]));
%
PBD=(gammas.*(zcurve(xin,[thetae,Ref]).^2).*funNg(phi)+c.*(zcurve(xin,[thetae
,Ref])).*funNc(phi)+abs(qm).*(zcurve(xin,[thetae,Ref])).*funNq(phi)).*cos(ata
n2(xin.*tan(alphac)./Kb,(Ru-Rw))+gammat).*tan(alphac);
%              FBD=trapz(PBD).*inc;
%
%              % calculate the total lateral force
%              Fy= -(Fycp+FBD);
%          end
%      end
%
%      % Overturning moment
%      Cmxg=funquad(Cmxgprm,Fz);
%      Cmxa=funquad(Cmxaprm,Fz);
%      Cgamma=funsat(Cgammaparam,Fz);
%      Mx=Cmxg.*(Cgamma+Fz).*Rl.*sin(gammat)+Cmxa.*Fycp+Rl.*cos(gammat).*FBD;
%
```

```
%     % Aligning moment
%     Cmz1=funquad(Cmz1prm,Fz);
%     Cmz2=funquad(Cmz2prm,Fz);
%     Cmz3=funquad(Cmz3prm,Fz);
%     Mz=-
funkz([Cmz1,Cmz2,Cmz3],alphac).*(Fycp.*cos(gammat)+Cgamma.*sin(gammat))+Ru.*s
in(thetae).*FBD;
%
% else
    % use rigid wheel model
    % Needs the functions
    % thetaefun.m
    % sigman.m
    % taux.m
    % tauy.m
    % Rigid wheel formulation

    % Calculates thetae initially
    a=tan(pi./4-phi./2);
    thetaes=abs(atan2(abs(-(-(0.1e1 + sqrt((-2 .* a .^ 2 .* sd + a .^ 2 .* sd
.^ 2 - 2 .* a .^ 4 .* sd + a .^ 4 .* sd .^ 2 + a .^ 4))) ./ (1 + a .^ 2) +
0.1e1) ./ a ./ (-1 + sd)), abs(-(0.1e1 + sqrt((-2 .* a .^ 2 .* sd + a .^ 2 .*
sd .^ 2 - 2 .* a .^ 4 .* sd + a .^ 4 .* sd .^ 2 + a .^ 4))) ./ (1 + a .^ 2)
./ (-1 + sd))));

    % limits thetan to 1/3 of phi, based on the retaining wall problem
    if thetaes>0,
        thetaes=min(abs(thetaes),(1/3).*phi).*sign(thetaes);
    else
        thetaes=min(abs(thetaes),0).*sign(thetaes);
    end

    % Calculate entry angle
    [thetae,costval] = fminsearch(@(x)
thetaefun(x,inc,thetab,Ru,b,kc,kphi,gammas,c,n,Kx,Ky,phi,sd,alphac,Fz),thetae
s+deg2rad(10),optimset('Display','off'));
%     thetae=0.3076;
    theta=thetae:-inc:thetab;

    % Radial Stress Calculations
    sigmaval=sigman(theta,thetab,thetae,Ru,b,kc,kphi,c,gammas,n,phi,sd);

    % Maximum stress envelope

taum=(c+sigman(theta,thetab,thetae,Ru,b,kc,kphi,c,gammas,n,phi,sd).*tan(phi))
;
    taum(1)=0;
    taum(end)=0;

    % Lateral shear stress

tausy=tauy(theta,thetab,thetae,Ru,b,kc,kphi,gammas,c,n,Kx,Ky,phi,sd,alphac);

    % Longitudinal shear stress
```

```
tausx=taux(theta,thetab,thetae,Ru,b,kc,kphi,gammas,c,n,Kx,Ky,phi,sd,alphac);

    % Calculate wheel vertical load
    if omega==0,
        W = - Ru.*b.*(trapz(sigmaval.*cos(theta)).*inc);
    else
        W = - Ru.*b.*( trapz(tausx.*sin(theta)).*inc +
trapz(sigmaval.*cos(theta)).*inc);
    end

    % Longitudinal Force
    if omega==0,
        if sd==0,
            Fx= 0;
        else
            Fx= Ru.*b.*( trapz(tausx.*cos(theta)).*inc -
trapz(sigmaval.*sin(theta)).*inc);
        end
    else
            Fx= Ru.*b.*( trapz(tausx.*cos(theta)).*inc -
trapz(sigmaval.*sin(theta)).*inc);
    end

    %Driving Torque
    if omega==0,
        My= 0;
    else
        My= Ru.^2.*b.*(trapz(tausx).*inc);
    end

    if abs(alphac)<1e-8,
        % Lateral shear stress force at alphac=0
        Fy=0;
        Fycp=0;
        FBD=0;
    else
        % Lateral shear stress force
        Fycp= Ru.*b.*( trapz(tausy).*inc );

        % Calculate the bulldozing force
        if abs(thetae)<1e-8,
            % if sinkage is zero, the bulldozing force is zero
            FBD=0;
        else
            xin=inc:inc:2*Ru*sin(thetae);
            m=tan(pi/4+phi/2);
            qm=(gammas.*Ru.*(2.*thetae-
sin(2.*thetae)).*xin.*tan(alphac))./(m.*zcurve(xin,[thetae,Ru]));

PBD=(gammas.*(zcurve(xin,[thetae,Ru]).^2).*funNg(phi)+c.*(zcurve(xin,[thetae,
Ru])).*funNc(phi)+abs(qm).*(zcurve(xin,[thetae,Ru])).*funNq(phi)).*cos(gammat
).*tan(alphac);
            FBD=trapz(PBD).*inc;
```

```
            % calculate the total lateral force
            Fy= -(Fycp+FBD);
        end
    end

    % Overturning moment
    Cmxg=funquad(Cmxgprm,Fz);
    Cmxa=funquad(Cmxaprm,Fz);
    Cgamma=funsat(Cgammaparam,Fz);
    Mx=-Fz.*Ru.*sin(gammat)-Ru.*cos(gammat).*Fy;

    % Aligning moment
    Mz=sin(thetaes).*Fycp+Ru.*sin(thetae).*FBD;

% end

condp=pc<max(sigmaval);

figure(1)
subplot(2,2,1)
plot(theta,sigmaval,'r-',...
                            'LineWidth',3,...
                            'MarkerSize',6)
ylabel('\sigma_n(\theta), Pa','fontsize',14)
xlabel('\theta, rad','fontsize',14)
axis([-0.25 1 0 300000])
grid on

SUBPLOT(2,2,2)
plot(theta,taum,'r-',theta,-taum,'g-',theta,tausx,'b:',theta,sigmaval,'m-
',theta,-sigmaval,'m-',...
                            'LineWidth',3,...
                            'MarkerSize',6)
ylabel('\tau_x(\theta), Pa','fontsize',14)
xlabel('\theta, rad','fontsize',14)
axis([-0.25 1 -300000 300000])
% h_legend=legend('+ve limit','-ve limit','Patch Stress','Rad. Stress','Rad.
Stress')
% set(h_legend,'fontsize',16)
grid on

SUBPLOT(2,2,3)
plot(theta,taum,'r-',theta,-taum,'g-',theta,tausy,'b:',theta,sigmaval,'m-
',theta,-sigmaval,'m-',...
                            'LineWidth',3,...
                            'MarkerSize',6)
ylabel('\tau_y(\theta), Pa','fontsize',14)
xlabel('\theta, rad','fontsize',14)
axis([-0.25 1 -300000 300000])
grid on

if condp>0.5,
    z=Ru.*(cos(thetab)-cos(thetae))
    SUBPLOT(2,2,4)
    thetafull=(0:0.01:2*pi);
```

```
    [Ref1] = radialdef(Ru,beta,Fz./Kz,ccons,alp,p_i,omega,cdamp,thetafull);
    thetafull=thetafull+thetaes;

    x1=Reff(end).*cos(theta(end)-pi/2):-0.01:-0.55;
    y1=Reff(end).*sin(theta(end)-pi/2).*ones(1,length(x1));
    x2=Reff(1).*cos(theta(1)-pi/2):0.01:0.55;
    y2=Reff(1).*sin(theta(1)-pi/2).*ones(1,length(x2));

    plot(Ref1.*cos(thetafull-pi/2),Ref1.*sin(thetafull-pi/2),'b-
',Reff.*cos(theta-pi/2),Reff.*sin(theta-pi/2),'r:',x1,y1,'k-
',Ru.*cos(thetafull-pi/2),Ru.*sin(thetafull-pi/2),'g-.',x2,y2,'k-',...
                                'LineWidth',3,...
                                'MarkerSize',6)
    axis([-0.55 0.55 -0.41 0.42])
    xlabel('Radius, m','fontsize',14)
    ylabel('Radius, m','fontsize',14)
    grid on
else
    z=Ru.*(1-cos(thetae))
    SUBPLOT(2,2,4)
    thetafull=(0:0.01:2*pi);
    thetafull=thetafull;

    x1=Ru.*cos(theta(end)-pi/2):-0.01:-0.55;
    y1=Ru.*sin(theta(end)-pi/2).*ones(1,length(x1));
    x2=Ru.*cos(theta(1)-pi/2):0.01:0.55;
    y2=Ru.*sin(theta(1)-pi/2).*ones(1,length(x2));

    plot(Ru.*cos(thetafull-pi/2),Ru.*sin(thetafull-pi/2),'b-',Ru.*cos(theta-
pi/2),Ru.*sin(theta-pi/2),'r:',x1,y1,'k-',x2,y2,'k-',...
                                'LineWidth',3,...
                                'MarkerSize',6)
    axis([-0.55 0.55 -0.41 0.42])
    xlabel('Radius, m','fontsize',14)
    ylabel('Radius, m','fontsize',14)
    grid on
end

Fz=abs(W);
DP=Fx
DP_n=DP./Fz.*100;
T=My
T_n=T./(Fz.*Ru).*100;
```

C. Terramechanics Rig Operations Manual

Step 1: Starting up the Terramechanics Rig

Task A. Panel HVP-1 powers the motors, supplying 480 Volts. Breaker 15 should be flipped to the "ON" position and is shown as Figure C-1.

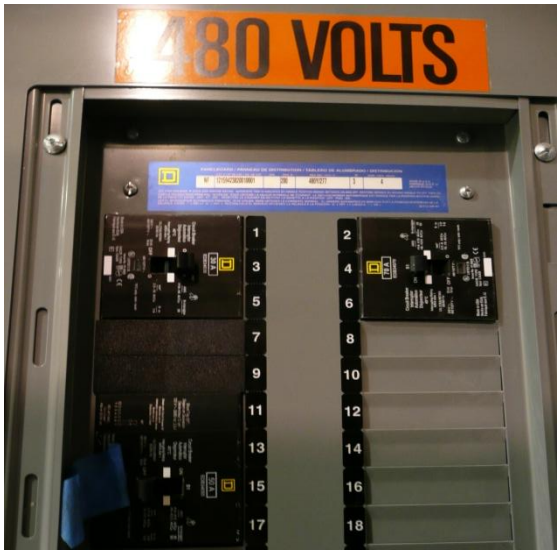

Figure C-1. Panel HVP-1 supplies 480 Volts to the motors. Breaker 15 must be flipped on to supply the voltage.

Task B. Panel LVP-1 powers the controller drives supplying 120 Volts. Breaker 28 should be flipped to the "ON" position and is shown as Figure C-2.

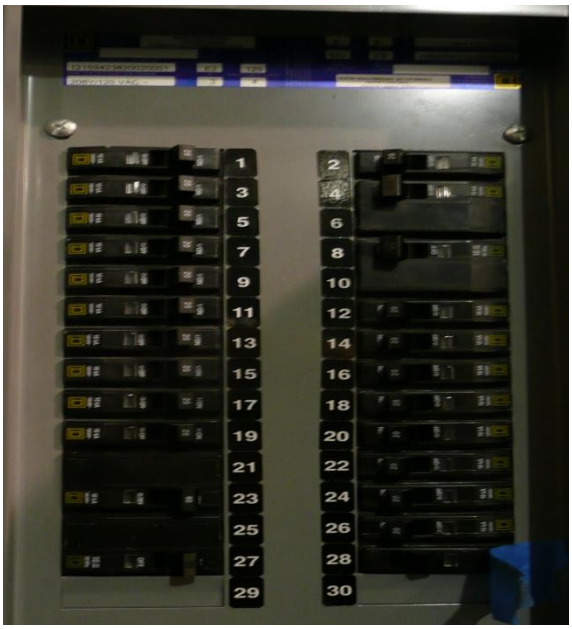

Figure C-2. Panel LVP-1 supplies 120 Volts to power the motors. Breaker 18 must be flipped on to supply the voltage.

Task C. To ensure the terramechanics rig has been energized correctly, both the 480 V and 120 V lights on the controller panel should be illuminated as shown in Figure C-3. Note that one of the Emergency Stop Buttons is located on the side of the controller panel.

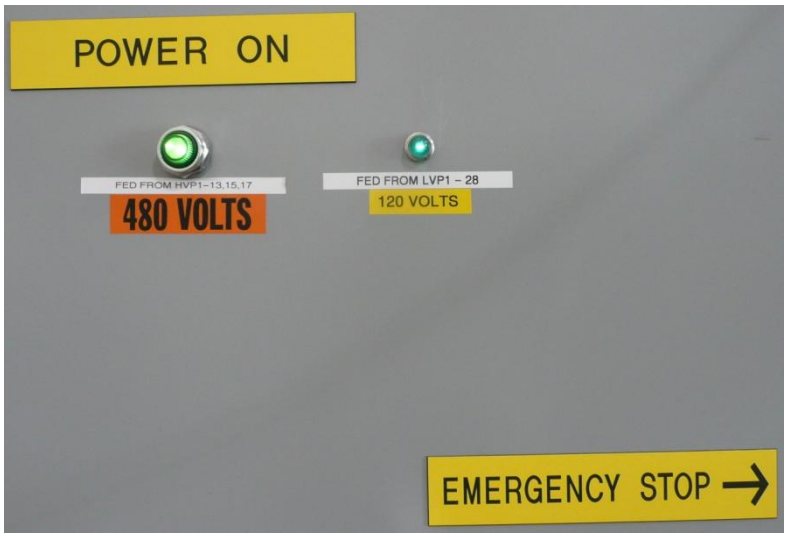

Figure C -3. The controller panel has been successfully energized when the 480 V and 120V lights are illuminated.

Task D. Turn on the LMS SCADAS III data acquisition system (DAQ) by switching on the power switch located on the rear of the device above the power chord connection. Figure C-4 shows the front of the DAQ device.

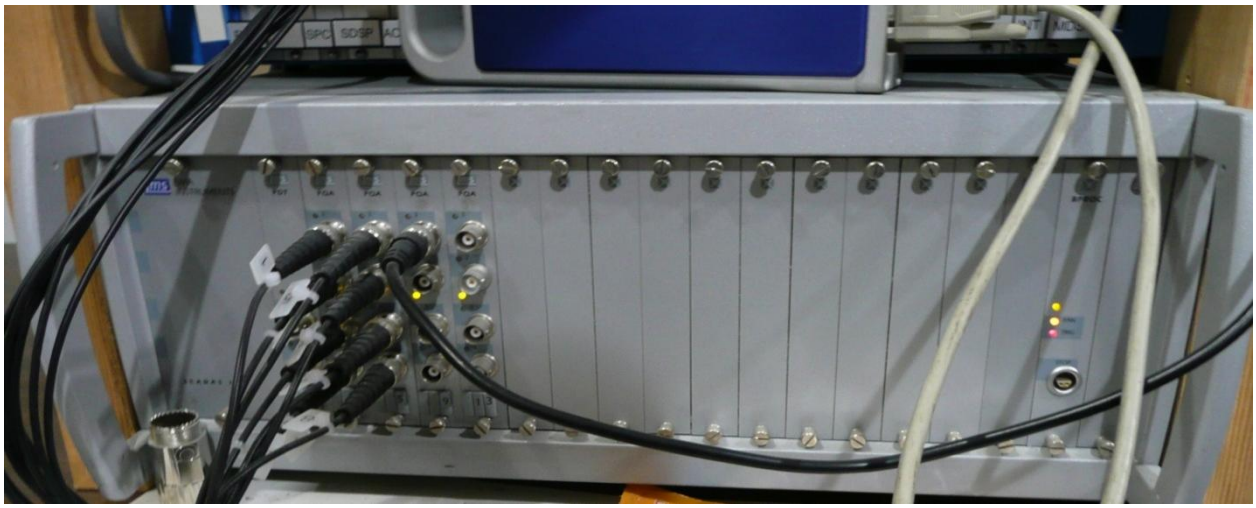

Figure C-4. The LMS SCADAS III data acquisition system (DAQ). The power switch is located on the back of the device above the power chord connection.

Task E. The desktop computer is the interface between the user and the rig. Turn on the computer and allow it to boot up to the user desktop. The computer is shown in Figure C-5.

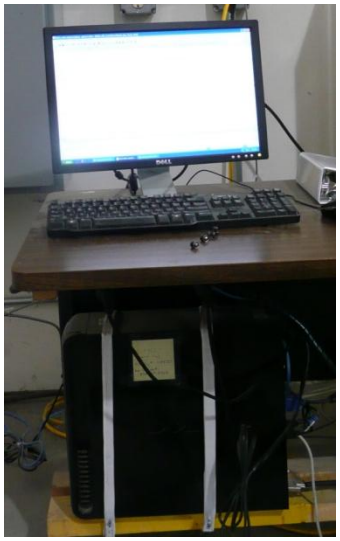

Figure C-5. Boot the desktop computer to bring up the user desktop.

Task F. Check the keyed safety switches, located at the **Northwest** and **Northeast** corners of the rig, to make sure their red lights are illuminated. If they are not, turn the key clockwise so that the light turns on. Shown in Figure C-6 is a photo of the key located at the **Northeast** corner.

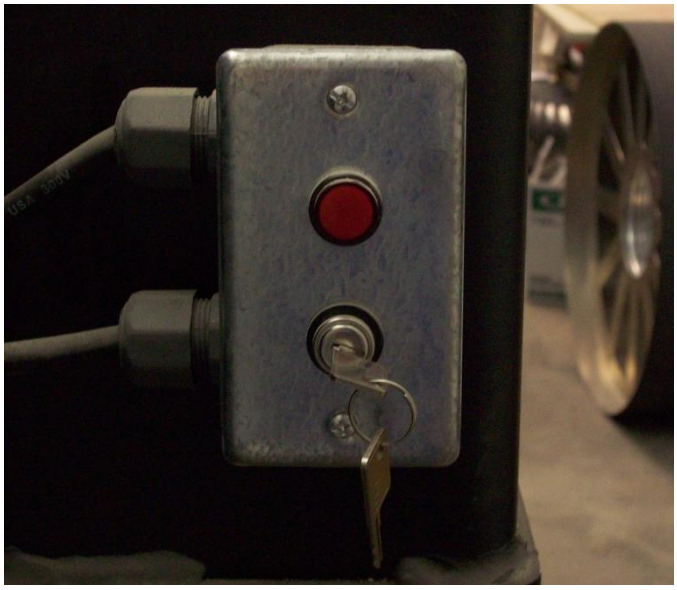

Figure C-6. Keyed safety switch located at the Northeast corner of the terramechanics rig.

Step 2. Warming up the Terramechanics Rig

Task A. The controller interface program is PiCPro V16.0 MMC Edition. Access the program by clicking the "Start" button and follow the selection scheme as shown in Figure C-7.

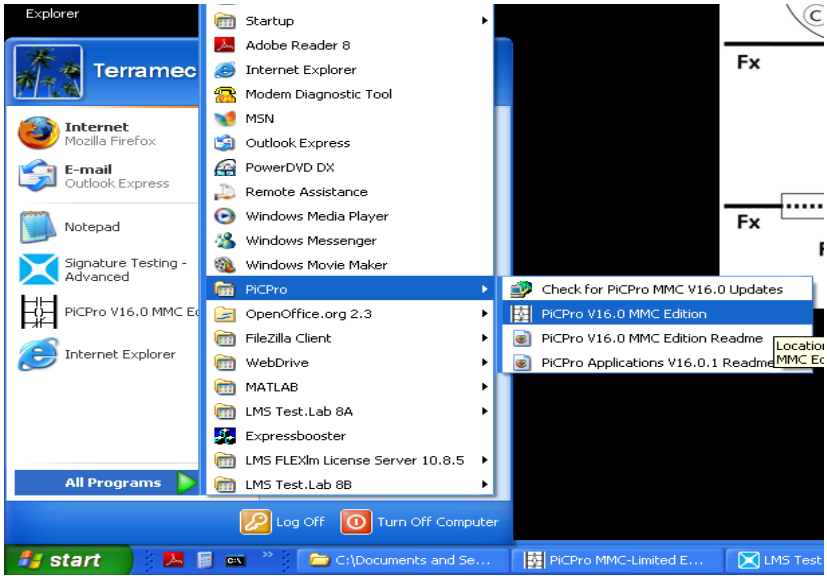

Figure C-**7.** The selection scheme showing how to open PiCPro, the controller interface.

Task B. Before the rig can be used, it must be warmed up. Once PiCPro has been loaded, spin the wheel while keeping the carriage stationary. This task will be specific to the project and program code being used. Consult the help section of PiCPro to learn how to spin the wheel or add it into the code being used. The warm-up rotational speed of the wheel should be set to **2** ***rad/s*** and should be spun for at least **fifteen minutes**. Note that the wheel to be tested must be mounted to the Kistler wheel sensor hub prior to spinning the wheel.

Important: The PiCPro program operates in Ladder Units (*LU*/min). The conversion factors into these units are as follows:

$$\frac{\frac{LU}{\min}}{\frac{cm}{s}} = 34515.9285$$

$$\frac{\frac{LU}{\min}}{\frac{rad}{s}} = 572957.7684$$

***Example**: PiCPro code is shown as Figure C-8. The "Position" block controls Axis 1, which is the axis of the translational movement of the carriage in the longitudinal direction. To spin the wheel, the "Rate" input should be changed to zero for Axis 1. The "VEL_STRT" block controls Axis 2, which is the axis about which the wheel will rotate. The "Rate" input for Axis 2 should be set to **2 rad/s**.*

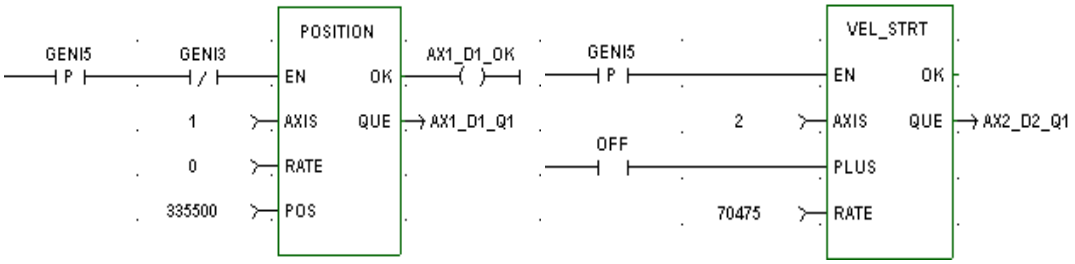

Figure C-8. The PiCPro code blocks for Axes 1 and 2 where the rate of Axis 1 must be set to zero and the rate of Axis 2 must be set to 2 *rad/s* to warm up the Kistler wheel sensor.

Task C. The rig remote controller is shown as Figure C-9 with labeled button functions. As labeled, the buttons correspond to the code used in the example above. The actual functionality of the controller buttons will be dependent on the code.

Figure C-9. The terramechanics rig controller showing the function of each button corresponding to an example code.

Step 3. Starting the Kistler System

Task A. Switch the Kistler system power supply to the "ON" position. Figure C-10 shows the power source located on top of the table, and Kistler system below it on top of the DAQ.

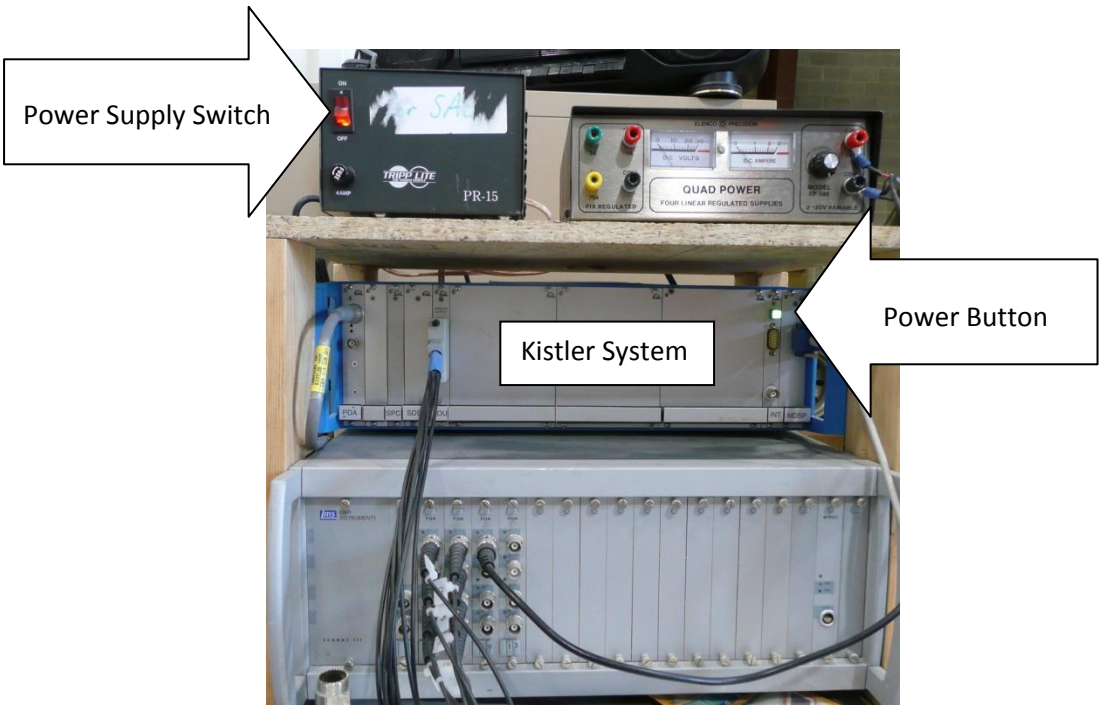

Figure C-10. The Kistler System with power source above and DAQ below.

Task B. The laptop computer shown runs the user interface of the Kistler system. To open the interface, turn on the laptop to load the desktop. Then open the "Software" folder on the desktop. Next, click on the Remote_120 icon to open the interface program. Figure C-11 shows the laptop with the correct icon highlighted.

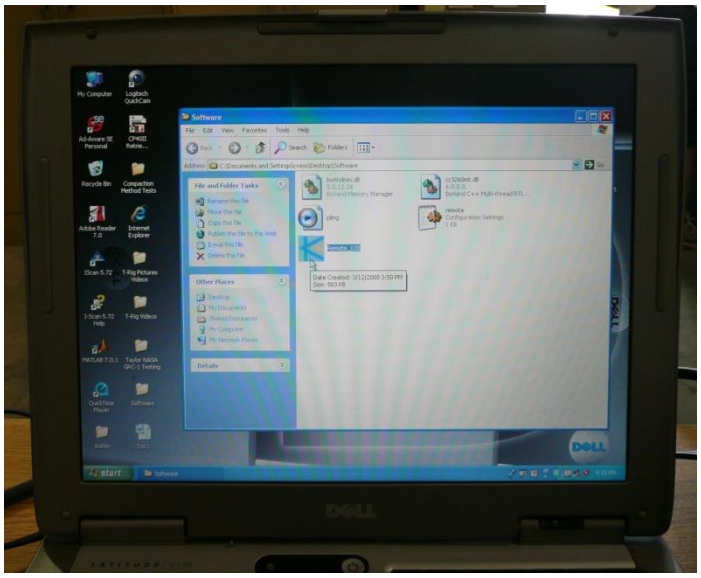

Figure C-11. The laptop computer that runs the Kistler system user interface.

Task C. When the user interface appears, the COM port must be enabled. Click the "COM" button in the lower right hand corner to bring up the screen shown as Figure C-12. Click "COM 1" followed by the "DONE" button. Then push the green power button located on the top right hand corner of the Kistler system (shown in Figure C-10). Be sure to have the wheel spinning when powering up the Kistler wheel force hub.

Note: If the interface fails to recognize the COM 1 port, restart the computer and repeat.

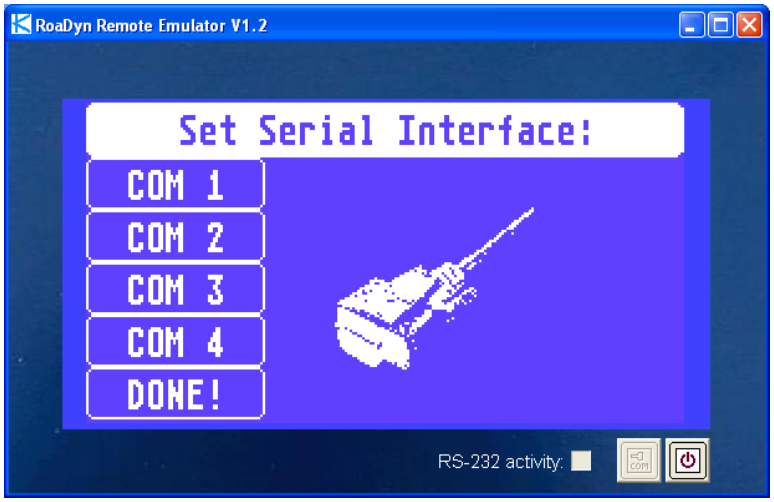

Figure C-12. The COM 1 port must be enabled when the Kistler interface is opened.

Task D. Once the Kistler system is recognized by the laptop, the main screen will appear as shown in Figure C-13.

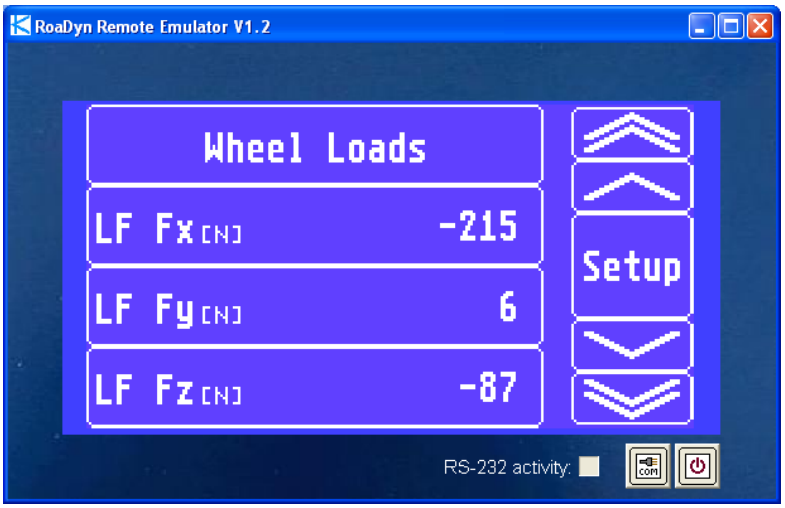

Figure C-13. The main screen of the Kistler interface displays the measured forces and moments.

The Kistler system must be calibrated before use. Click the "Setup" button in the middle right of the screen to arrive at the setup screen shown as Figure C-14. From this screen, all calibrations, checks, and customizations of the Kistler system can be performed.

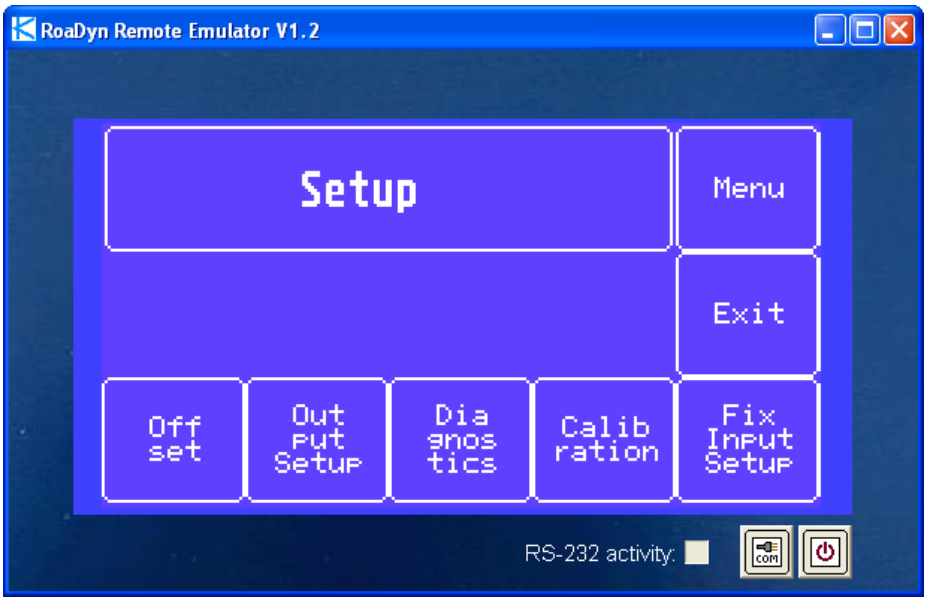

Figure C-14. The Setup screen of the Kistler system.

Task E. First, perform the angle calibration for the sensor magnets. To do this, select "Offset", then "Angle Calibration", and "Clear All" to clear out any previous angle calibration data. Once this is done, go back to the "Angle Calibration" screen and select "Left Front." Performing this procedure first will help in avoiding any angle errors, which could appear once the Kistler sensor is powered up and operational.

Task F. Second, set the Analog Scale by clicking the "Output Setup" button, followed by the "Analog Scale" button. Use the mouse to input the code which is "3-5-7," click "Enter" and verify the Analog Output Scale and Offset values on the next two screens. Click "Done" to cycle through each and back to the Setup screen.

Task G. Next, on the Setup screen, click the "Diagnostics" button, followed by clicking the "Left Front" button. Scroll down using the arrows on the right hand side of the screen to find the "TMU Data" button and click on it. Verify that the temperature has reached steady state to prevent drift in measured values. Click "Done" to exit. The Diagnostics screen is shown as Figure C-15.

Note: The terramechanics rig simulates the Left Front wheel of a vehicle. Under all operations in the Kistler system that require wheel specification, always select "Left Front".

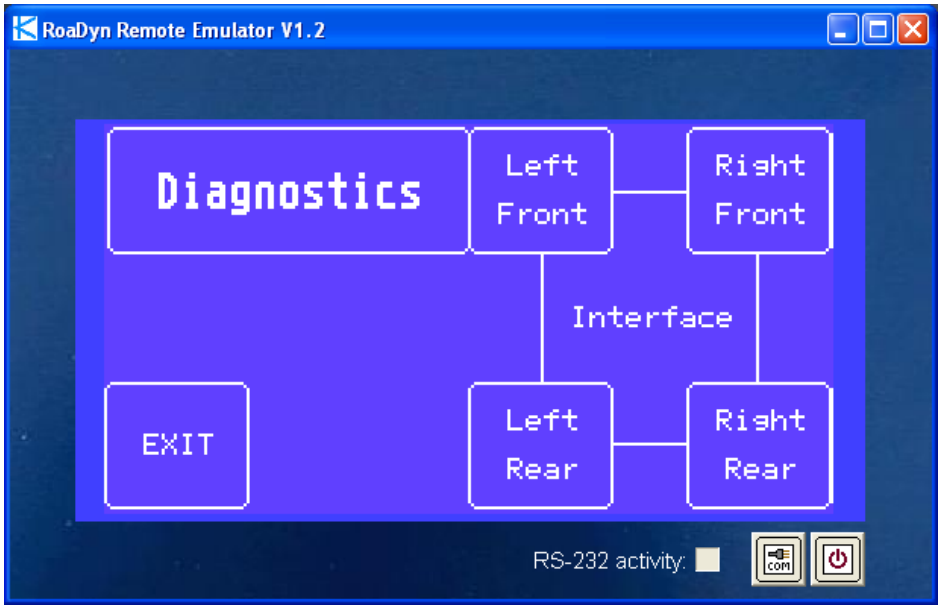

Figure C-15. The Diagnostics screen of the Kistler system.

Task H. Now that the terramechanics rig has been warmed up, while the wheel is still spinning, the Signal Offset must be calibrated. Select "Offset" from the Setup screen, followed by "Signal Offset" which is shown as Figure C-16. Select "Clear All" to purge any previous calibrations. The Setup screen will reappear. Revisit the "Signal Offset" screen. Select "Left Front" to perform the offset and wait until the calibration reaches 100%.

Note: Perform the Signal Offset immediately before testing to prevent drift. Any applied forces and settling could cause drift.

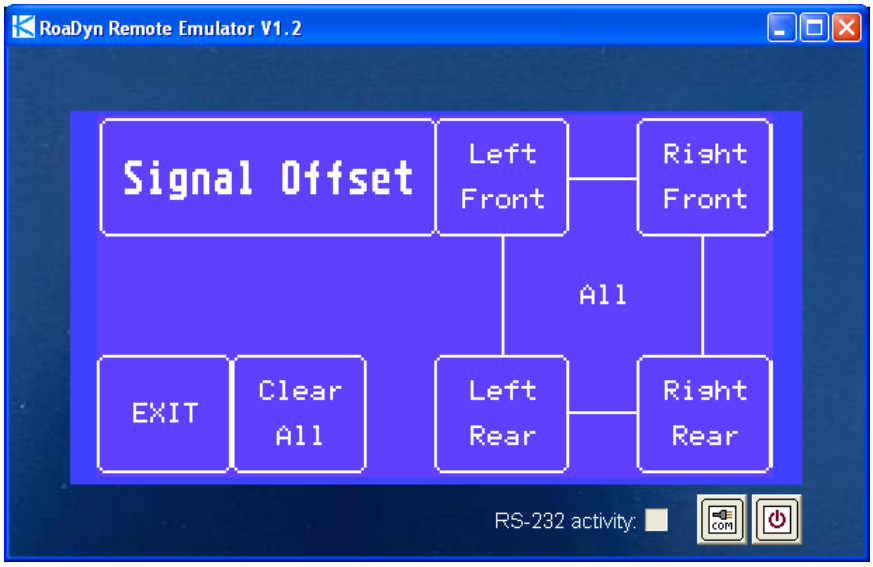

Figure C-16. The Signal Offset screen of the Kistler system.

Task I. The terramechanics rig is now calibrated and is ready for use. Make sure all systems are shut down and powered off when finished.

Step 4. Powering Down the Terramechanics Rig

Task A. Start by turning off the Kistler system. To do so, first push the green "Power Buton" shown in Figure C-10. Allow about **15-20 seconds** for the system to fully power down out of the system before turning the "Power Supply Switch" in Figure C-10 to the "OFF" position.

Task B. Save all important data that has been acquired using the LMS DAQ system. Test.Lab (the LMS software interface) will normally ask if the user would like to save his/her data if said user attempts to close the program before saving. Once Test.Lab has been closed, turn off the LMS DAQ frontend, using the same switch on the back of the device.

Task C. Before closing the rest of the programs on the rig computer, make sure the carriage is at the "Home Position" of the terramechanics rig. The home position is located at the **West** end of the soil bin.

Task D. Close all programs, saving where needed, and shut down the desktop computer.

Task E. Next, turn off the keyed safety switches. To do so, turn the keys counterclockwise until the light is no longer illuminated.

Task F. Return to circuit breaker panels and turn off Breakers 15 and 18, on the HVP-1 and LVP-1, respectively. Recall that the HVP-1 and LVP-1 are shown in Figure C-1 and C-2, respectively.

Task G. Perform a quick walk-around of the rig and check to make sure all electronics are turned off and all tools are returned to their appropriate storage areas.